

**CHARACTERIZATION OF RARE EARTH AND III-V NANOSTRUCTURED  
MATERIALS USING  
EXPERIMENTAL AND NOVEL DATA ANALYSIS TECHNIQUES**

by

Anagha S. Kulkarni

A dissertation submitted to the Faculty of the University of Delaware in partial fulfillment of the requirements for the degree of Doctor of Philosophy in Electrical and Computer Engineering

Spring 2018

© 2018 Anagha S. Kulkarni  
All Rights Reserved

**CHARACTERIZATION OF RARE EARTH AND III-V NANOSTRUCTURED  
MATERIALS USING  
EXPERIMENTAL AND NOVEL DATA ANALYSIS TECHNIQUES**

by

Anagha S. Kulkarni

Approved: \_\_\_\_\_  
Kenneth E. Barner, Ph.D.  
Chair of the Department of Electrical and Computer Engineering

Approved: \_\_\_\_\_  
Babatunde A. Ogunnaike, Ph.D.  
Dean of the College of Engineering

Approved: \_\_\_\_\_  
Ann L. Ardis, Ph.D.  
Senior Vice Provost for Graduate and Professional Education

I certify that I have read this dissertation and that in my opinion it meets the academic and professional standard required by the University as a dissertation for the degree of Doctor of Philosophy.

Signed:

---

Matthew F. Doty, Ph.D.  
Professor in charge of dissertation

I certify that I have read this dissertation and that in my opinion it meets the academic and professional standard required by the University as a dissertation for the degree of Doctor of Philosophy.

Signed:

---

D. Bruce Chase, Ph.D.  
Member of dissertation committee

I certify that I have read this dissertation and that in my opinion it meets the academic and professional standard required by the University as a dissertation for the degree of Doctor of Philosophy.

Signed:

---

Ryan Zurakowski, Ph.D.  
Member of dissertation committee

I certify that I have read this dissertation and that in my opinion it meets the academic and professional standard required by the University as a dissertation for the degree of Doctor of Philosophy.

Signed:

---

Robert L. Opila, Ph.D.  
Member of dissertation committee

## ACKNOWLEDGMENTS

First and foremost, I would like to thank my doctoral advisor Dr. Matthew F. Doty. He took me on as a doctoral student when I wasn't entirely sure if my doctoral dream was possible and for that I am eternally grateful. He has lead me patiently through the years and like a true Guru also stepped back when the time was right to afford me the luxury of finding my own way. Dr. Doty has taught me everything I know about low dimensional semiconductor physics and given me the tools to break down any problem no matter how complex. These invaluable lessons I take with me in my professional and personal life.

When I first met Dr. D. Bruce Chase I was intimidated by the wealth of knowledge he possesses in the world of spectroscopy and optics. Over the years, this first impression of being intimated by him has been shattered. He has been an amazing mentor to me during the last 3 years and has given me valuable lessons in spectroscopy, optics, life in the industry, humility and humor. Dr. Chase is the hidden super power of the Doty lab and I grateful for his mentorship and guidance.

I would also like to express my deepest gratitude to Dr. Ryan Zurakowski, the MCMC project would not have been possible without his guidance and mentorship. He helped me appreciate the beauty of mathematical modeling and statistical analysis by teaching me the nuances of the field. I am grateful for unique opportunity to work on a truly inter disciplinary project. I would also like to thank Dr. Robert L. Opila for being on my committee and sharing his expertise in FRET and MCMC modelling with me. Dr. Heather Doty, Dr. Pam Cook and Dr. Rachel Davidson, I am grateful for

everything I have learned from them during my time on the Women in Engineering steering committee. I thank Andrew F. Burnett for being the epitome of a “work-dad”.

I would like to thank all my lab mates, past and present, for helping me: fill liquid Nitrogen innumerable times, build the reliquifier, ship the open cycle cryostat, Optics 101, invaluable discussions and all the laughter: Dr. Weiwen Liu, William Reid, Dr. Xinran Zhou, Dr. Laura Rose Vanderhoef, Dr. Chelsea Haughn, Dr. Diane Sellers, Jamie Beshore, Eric Chen and Xiangyu Ma. I am also thankful for the ECE family who helped me during my initial days and continued to support me through the ups and downs of grad school: Dr. Luisa Polania, Dr. Qi Wang, Sergio Pino and Dr. Irene Manotas. The staff in Evans and Dupont, specifically, Kathy Forwood, Gwen Looby, Jo Ann Rucker, Christine Williamson, Robin Buccos, Karen Di Stefano and Amber Spivey have been extremely friendly, approachable and I am grateful to them for their numerous favors.

On a more personal note, I would like to thank Nagamani Mundru, Mayuri Utturkar, Pradeepti Batala, Drs. Nicole Kotulak, Nandita Bhagwat, Chelsea Haughn and Sona Lakshmi Balasubramaniam for your unwavering support and friendship. You are some of the smartest, kindest, sassiest and loving people I have met and I feel lucky to count them amongst my friends. Dr. Samir and Shivangi Mushrif for graciously opening your home to me, I am grateful. Dr. Subodh and Mrs. Vibha Wagle, thank you for your love, affection and “khau”. Dr. Laura and Jesse Vanderhoef, I am forever indebted to you for welcoming me into their heart, home and family. I thank, Shirisha Reddy, for being a constant friend through the highs and the many lows over the last 12 years. Dr. Soma Dash I thank you for being who she is and letting me adopt her. Abhinav R. Jain and Dr. Devesh Radhakrishnan, words cannot

describe how grateful I am for their friendship, love and support. They are the family I chose.

Amongst the many blessing I have, being part of the Kulkarni and Vempati families is the greatest. Without their blessings and prayers, I would not have made it this far for which I am eternally grateful. I would like to thank, Wg Cdr Mallikarjun and Ratnavali Vempati, for welcoming me into their family and providing me with love and unwavering support. I would like to thank my grandparents, Nalini and Anant Kulkarni, for always being there especially when the going got tough, showering me with unconditional love, instilling in me values of duty and importance of family. Dr. Rasika Ramdasi, I thank for being a part of our crazy family, her presence has enriched our lives.

The loves of my life: Nikhilesh, words cannot describe how incredibly lucky I feel to be his partner. This first year of our marriage has brought me immeasurable amount of happiness, joy, love and peace and I cannot wait to see what life throws our way. I thank Niki for the friendship, support and undying love showered on me over the last 13 years. I thank my brother, Dr. Sameer Kulkarni, for being my first and forever best friend, my biggest support system and reality check. I thank, my father, Col S.A Kulkarni, for being my biggest cheer leader, safety net, my strength, my life. The three loves of my life, Niki, Goada and Baba, make me, me, they are the fibre of my being.

*I dedicate this dissertation to my mother, Urmila S. Kulkarni.*

*Aai, we miss you.*

## TABLE OF CONTENTS

LIST OF TABLES .....	xii
LIST OF FIGURES .....	xiii
ABSTRACT .....	xvii

### Chapter

1	INTRODUCTION .....	1
1.1	Motivation for novel material systems .....	1
1.1.1	Motivation for studying ErAs Nano composite.....	2
1.1.2	Motivation for studying QDMs.....	4
2	PROPERTIES AND GROWTH METHODS OF NANOSTRUCTURED SEMICONDUCTOR MATERIALS .....	5
2.1	Properties of Semiconductors .....	5
2.1.1	Formation of Bands .....	5
2.1.2	Manipulation of Band Structure .....	7
2.2	Growth of Heterostructures .....	8
2.2.1	Molecular Beam Epitaxy .....	9
2.3	Quantum Dots.....	10
2.3.1	Confinement by Quantum Dots.....	11
2.3.2	Growth of Epitaxial QDs.....	13
2.4	Quantum Dot Molecules.....	15
2.4.1	Properties of QDMs.....	16
2.4.2	VQDM growth mechanism .....	19
2.5	Ln-V Nanocomposite material systems.....	20

2.5.1	Electronic Properties of ErAs NP in GaAs Matrix .....	21
2.5.2	Growth Processes for ErAs NPs .....	22
2.5.2.1	Growth via co-deposition .....	22
2.5.2.2	Growth via Growth Interrupt .....	23
2.6	Summary.....	24
3	OPTICAL CHARACTERIZATION OF LOW DIMENSIONAL SEMICONDUCTORS .....	25
3.1	Photoluminescence (PL).....	25
3.1.1	Principal Components of a PL spectroscopy set up .....	26
3.2	Optical absorption and emission in low dimensional semiconductor heterostructures .....	28
3.2.1	Optical selection rules .....	30
3.2.2	QD Photoluminescence under electric field .....	31
3.3	Time integrated photoluminescence spectroscopy .....	34
3.3.1	Optical set up .....	35
3.3.2	Helium cooled open cycle Cryostat.....	36
3.3.3	Time integrated PL spectrum .....	36
3.4	Time Resolved Photoluminescence Spectroscopy .....	38
4	USING TIME RESOLVED PHOTOLUMINESCENCE TO UNDERSTAND ENERGY TRANSFER MECHNAISMS IN ERAS NANOCOMPOSITES.....	42
4.1	Förster resonance energy transfer (FRET) .....	43
4.2	Tunneling.....	45
4.3	Hypothesis for the experiment.....	47
4.4	Sample structure .....	48
4.5	Temperature dependent TRPL .....	49
4.6	FRET calculations .....	51
4.7	Conclusions .....	53
5	EXTRACTING PHYSICAL PARAMETER VALUES FROM QDM SPECTROSCOPY DATA.....	55
5.1	Introduction .....	55

5.2	Structure of the VQDM studied .....	55
5.3	Time integrated PL data from a QDM .....	56
5.4	Notations.....	57
5.5	Spectroscopic Signatures and Hamiltonians .....	58
5.5.1	Anticrossing formation.....	58
5.5.2	Hamiltonian for $\mathbf{X0}$ State .....	60
5.5.3	Hamiltonian for the $\mathbf{Xh} + \mathbf{0}$ state.....	61
5.5.4	Formation of X pattern .....	62
5.5.5	Hamiltonian for $\mathbf{X2}$ – state .....	63
5.5.6	Hamiltonian for $\mathbf{Xh} + \mathbf{2}$ – state.....	65
5.6	Analytical expressions for observed spectral lines.....	66
5.7	Importance of physical parameters for device development .....	69
5.8	Traditional Data Extraction .....	69
5.9	Limitations of the traditional data extraction .....	71
6	MARKOV CHAIN MONTE CARLO INTEGRATION.....	73
6.1	Bayesian Inference .....	73
6.2	Markov chain Monte Carlo .....	75
6.2.1	Monte Carlo integration .....	75
6.2.2	Markov Chain.....	76
6.2.3	Conventional MCMC .....	77
6.2.4	MCMC using Gibbs sampling.....	78
7	IMPLEMENTING MCMC ON QDM SPECTROSCOPY DATA.....	79
7.1	Data extraction procedure.....	80
7.2	Implementing adapted MCMC.....	83
7.2.1	Uniquely identifiable parameters .....	84
7.2.2	Initialization of MCMC.....	90
7.2.3	MCMC simulation: what happens in a single iteration? .....	91
7.2.4	Burn in.....	93
7.2.5	MCMC Implementation .....	94
7.3	Conclusions .....	99
8	VALIDATION OF ADAPTED MCMC SIMULATION FOR SPECTROSCOPY DATA.....	100
8.1	Dependence on density of data point.....	100

8.1.1	Dense data set .....	100
8.1.2	Sparse data set .....	103
8.1.3	Comparison between MCMC simulations using dense and sparse data sets .....	106
8.2	Sensitivity to size of error bars .....	107
8.3	Summary.....	109
9	SUMMARY AND FUTURE WORK.....	110
	REFERENCES .....	114
Appendix		
A	HISTOGRAM OF ALL OBSERVABLES .....	120
B	ADAPTED MCMC MATLAB CODE .....	125
C	CODE FOR GENERATING PREDICTION INTERVAL .....	137
D	PROCEDURE FOR REFILLING LIQUID HELIUM WITH THE RELQUIFIER IN OPERATION.....	143
E	FIRST COOL DOWN PROCEDURE.....	145

## LIST OF TABLES

Table 7.1: List of all physical parameters that describe the TIPL map of VQDMs.....	85
Table 7.2: List of initial values used for all observables and tunneling coefficients ...	90
Table 7.3: Mean and confidence interval values for the observables generated using MCMC simulations .....	95
Table 8.1: Mean, maximum likelihood value and confidence interval values for the observables generated using a dense data set .....	101
Table 8.2: Mean, maximum likelihood value and confidence interval values for the observables generated using a sparse data set .....	104
Table 8.3: Comparison of mean and maximum likelihood values of observables generated from dense and sparse data .....	106
Table 8.4: Comparison of mean values of parameters for data sets with 25% larger error and 25% smaller error.....	108

## LIST OF FIGURES

Figure 2.1: Band formation in diamond <sup>9</sup> depicting the energy gap between allowed continuum of states or bands. ....	7
Figure 2.2: Three types of semiconductor heterojunctions organized by band alignment. <sup>10</sup> .....	8
Figure 2.3: Schematic of a MBE machine with multiple effusion cells, a rotating sample holder and a RHEED screen. <sup>13</sup> .....	11
Figure 2.4: Schematic of lowest three discrete energy levels formed due to confinement in two dimensions. <sup>17</sup> .....	14
Figure 2.5: Schematic of the growth of a typical InAs/GaAs quantum dot .....	16
Figure 2.6: Schematic of the band diagram of a QDM along its growth direction .....	18
Figure 2.7: Photoluminescence of neutral exciton which exhibits the formation of molecular states and the anticrossing $\Delta$ <sup>19</sup> .....	19
Figure 2.8: Cross-sectional STM image of vertically stacked InAs QDs <sup>7</sup> .....	20
Figure 2.9: Bulk ErAs band structure <sup>22</sup> .....	22
Figure 3.1: Schematic of PL generation under non-resonant excitation conditions.....	30
Figure 3.2: Interband and intraband transitions in a quantum dot (a) Different symmetries of Bloch waves for conduction and valence band allow optical transition (b) Intraband transition are allowed due to the different envelope functions <sup>32</sup> .....	32
Figure 3.3: Band diagram for a quantum well with (b) and without (a) external applied field which reduced the energy of both bound states and wavefunction of electron and hole are pushed on opposite directions of each other reducing the overlap integral <sup>33</sup> .....	33
Figure 3.4: Tuning of the energy levels of a QD across the Fermi sea of the doped substrate upon application of an electric field (flatter band) <sup>34</sup> .....	34

Figure 3.5: (a) Schematic of the Janis superconducting magnet system. The color in the center column depicts the gradient of the temperature. (b) Schematic of the sample insert of the sample column <sup>35</sup> .....	37
Figure 3.6: TIPL from VQDM of sizes 2.9 nm and 2.6 nm separated by a 6 nm GaAs barrier including 3 nm of AlGaAs at the center of the barrier under an applied electric field. ....	38
Figure 3.7: Schematic of the TRPL set up used to study ErAs:GaAs nanocomposites .....	39
Figure 4.1: Potential step barrier at $z = 0$ , the potential on the left is 0 and on the right is $V_0$ .....	45
Figure 4.2: Schematic of a single period of ErAs nanocomposites studied using TRPL .....	48
Figure 4.3: Decay time measured as a function of exciting laser fluence at (a) 7K, (b)37K, and (c)67K .....	50
Figure 4.4: FRET efficiency as a function of thickness of the barrier composed of pure GaAs, pure AlGaAs, and AlGaAs and GaAs.....	53
Figure 5.1: Schematic band diagram, composition, and size of VQDM sample studied. ....	56
Figure 5.2: (a) Raw time integrated PL map from VQDM of sizes 2.9 nm and 2.6 nm separated by separated by a 6 nm GaAs barrier including 3 nm of AlGaAs at the center of the barrier under an applied electric field (b) Extracted TIPL map .....	57
Figure 5.3: Formation of anti-crossing for a neutral exciton by tunneling of a single hole between dots in a VQDM under an applied electric field <sup>19</sup> .....	60
Figure 5.4: X pattern formation for the $X2$ – charge complex .....	62
Figure 5.5: Manual iterative fits for the neutral exciton line by varying the term $EX0D + V0101$ from 1338 meV to 1337.85 meV. ....	71
Figure 7.1: (a) Raw intensity plot extracted at 7.88kV/cm from TIPL data from a single VQDM under applied electric field (b) Section of the raw TIPL map extracted from TIPL data for a single VQDM under electric field being fit to the lorentzian.....	81

Figure 7.2: Lorentzian fit to raw PL data at two different field values for a single VQDM under applied electric field .....	82
Figure 7.3: Processed TIPL map with extracted peak energy and error bars generated from the Lorentzian fits on extracted data from raw TIPL map for a single VQDM under applied electric field .....	82
Figure 7.4: Manual fitting of parameter for neutral exciton line for a single VQDM under applied electric field using two values for $EX0D + V0101$ , pink (1338 meV) and blue (1337.85 meV). Each simulated line is within error bars. ....	84
Figure 7.5: Flowchart for implementation of a single run of MCMC .....	93
Figure 7.6: Flowchart for the final implementation of MCMC.....	94
Figure 7.7: Spectral map reproduced using observable values generated from the MCMC run (blue line) against the experimental data (red points) .....	97
Figure 7.8 : Histogram of four observables generated at the end of the MCMC simulation. ....	98
Figure 8.1: Sparse and dense data sets used to validate the robustness of MCMC ....	101
Figure 8.2: Individual plots for each spectral line depicting the simulated data generated from the maximum likelihood value for the observables (black), the experimental data (red) and the prediction interval (blue) for dense data set. ....	103
Figure 8.3: Individual plots for each spectral line depicting the simulated data generated from the maximum likelihood value for the observables (black), the experimental data (red) and the prediction interval (blue) for sparse data set. ....	105
Figure A.1: Histogram of M1, M2, M3 and M4 generated at the end of the MCMC simulation. ....	120
Figure A.2: Histogram of M5, M6, M7 and M8 generated at the end of the MCMC simulation. ....	121
Figure A.3: Histogram of M9, M10, $F_0$ and $tx^0$ generated at the end of the MCMC simulation. ....	122
Figure A.4: Histogram of $tx0h$ , $tx2$ , $tx2h$ and $ed$ generated at the end of the MCMC simulation. ....	123

Figure A.5: Histogram of SS, te2 and te2h generated at the end of the MCMC simulation. .... 124

## ABSTRACT

In recent years there has been great interest in developing new computing architectures that go beyond Moore's Law. Such architectures include spintronic and photonic devices that could enable logic functions analogous to CMOS technologies and novel architectures that include quantum information processing. Virtually all emerging device architectures rely on materials with structures on nanometer length scales, either as fundamental units of the computation (e.g. qubits based on the spin projection of electrons or hole confined in quantum dots) or as components of a larger functional material (e.g. ErAs nanoparticles embedded within GaAs heterostructures). It is thus crucial to understand physical phenomena such as charge carrier transfer and many-body interactions within and between these nanostructures.

The objective of this research is to develop and demonstrate statistically-valid methods for characterizing and understanding ErAs nanocomposites and vertically stacked InAs QDMs. Optical studies using time resolved photoluminescence (TRPL) and time-integrated photoluminescence (PL), respectively, investigate the energy structure and charge interactions in these novel nanostructures. Information such as recombination rates of excitons, coulomb interaction terms, and the effect of screening charges can all be extracted from these optical studies. We first demonstrate the use of TRPL to determine the mechanism of charge transfer in ErAs nanoparticles embedded in GaAs coupled with InAs QDs with applications in ultrafast optoelectronic devices.

We then demonstrate the first of its kind implementation of Markov Chain Monte Carlo (MCMC) simulations for extracting accurate values for physical parameters from sparse time integrated photoluminescence data from vertically stacked InAs QDs, which are of interest as components of potential quantum computing hardware. This MCMC simulation method provides a template for data analysis of data from other complex spectroscopic techniques.

The methods developed to probe and understand these disparate material systems provide important new tools for the design and development of the next generation of optoelectronic devices.

## **Chapter 1**

### **INTRODUCTION**

Semiconductor-based devices are the foundation of the electronics that have created and defined the modern world. The growth in the complexity and capacity of these devices, in parallel with decreasing cost, has been enabled by advances in both materials science and device design and fabrication. The dynamic growth of this industry over the last couple of decades was captured by the projections of “Moore’s Law,” which states that the number of transistors on integrated chips doubles every two years. This projection was based on three important factors, namely increase in die size, reduction in physical dimensions of the transistors themselves, and improvements to the circuit-device design.

#### **1.1 Motivation for novel material systems**

Over the past decade the predictions of Moore’s Law have started to stumble. Indeed, major chip manufacturers have recently announced that they will no longer attempt to keep up with the predictions. One of the primary bottlenecks is that devices have already reached the length scales on which quantum, inhomogeneity, and surface / edge effects adversely affect the performance of conventional CMOS devices.

There is great interest in developing new computing architectures that go beyond Moore. Such architectures include spintronic and photonic devices that could enable logic functions analogous to CMOS technologies, but with lower power consumption, less waste heat generation, and improved non-volatility. Other

architectures of interest include quantum information processing, which employs a fundamentally new paradigm for logic that could outperform all classical computers for certain classes of computational problems. In all cases, one of the fundamental challenges is to design, characterize, and understand the material platforms from which these architectures could be constructed. Virtually all emerging device architectures rely on materials with structures on nanometer length scales, either as quantum dots that confine a single charge to be used as a building block for a quantum information processing or as components of a larger functional nanocomposite such as GaAs heterostructures that include embedded ErAs nanoparticles (NP) that can control carrier densities and alter the optical response.

This dissertation is focused on methods for characterizing and modeling the properties of nanostructured semiconductors that could be the foundation for future optoelectronic devices. There are two thrusts. First, we seek to determine the dominant charge carrier transfer mechanism in ErAs nanocomposite structures. Second, we develop and demonstrate statistically-valid methods for characterizing and understanding physical phenomena in vertically stacked QDs.

### **1.1.1 Motivation for studying ErAs Nano composite**

New optoelectronic devices need a material platform whose properties have been optimized for applications in the fields of communication and sensing. Terahertz (THz) radiation is a relatively unexplored domain for applications in the fields of short range communication and imaging. Terahertz is the portion of the electromagnetic spectrum between that of infrared and microwave radiation (0.3 to 3THz), with some characteristics of both regions. Usage of this region of the EM spectrum has been limited because material systems capable of harnessing its potential haven't been

adequately developed. THz light can be generated in semiconductors by the rapid motion of photo generated charge carriers. Current density under a bias can be described as

$$J(t) = N(t)E_A(e\mu_e + h\mu_h)$$

where  $N(t)$  is density of charge carriers,  $E_A$  is the applied electric field,  $\mu_{e(h)}$  represents the mobility of electron (hole) and  $e$  ( $h$ ) represent the charge of the electron (hole). The hole contribution to current density is significantly smaller due to their higher effective mass and can be ignored. Thus, materials with a short electron lifetime and high electron mobility would be ideal for THz applications. Cross sectional scanning tunneling spectroscopy studies of ErAs NP embedded in a GaAs substrate determined that the ErAs NPs are semi-metallic<sup>1</sup>. Short carrier lifetimes and high mobility of charge carriers have been reported<sup>2,3</sup>. These properties make ErAs NP embedded in GaAs an ideal material platform for THz application. The second motivation behind studying this nanocomposite structure is the demonstrated enhanced surface plasmon resonance (SPR) by these material systems<sup>4</sup>. Coupling this nanocomposite structure with a QD could potentially augment optical response from the QD, making this hybrid composite system an attractive research platform for applications in photodetectors and lasers. Development of this material platform for photoconductive devices requires a clearer picture of what processes mediate charge transfer between these components. This dissertation focuses on determining the dominant charge carrier transfer mechanism in this hybrid composite system.

### 1.1.2 Motivation for studying QDMs

For computing, devices that go beyond Moore's law are governed by architectures that utilize alternate material platforms. These platforms harness quantum mechanical properties such as quantum entanglement and superposition exhibited by quantum states in three-dimensionally confined systems. Material platforms for quantum information processing should enable initialization, coherent manipulation, coherent coupling of multiple bits, and non-destructive readout. Single quantum dots satisfy the nascent requirements, making them a promising building block for quantum devices<sup>5</sup>. The next challenge for quantum information systems based on single QDs is scalability. One way to achieve scalability would be to engineer quantum interactions with other QDs or photonic cavities. These conditions could be met by quantum dot molecules. Quantum dot molecules are vertically- or laterally-stacked QDs that are coupled by tunneling. This tunnel coupling can be manipulated by an electric field that in turn modulates the indirect transitions<sup>6</sup>. Unique spin properties also emerge as a result of tunneling between the QDs<sup>7,8</sup>. Engineering this tunability opens another door for manipulation of quantum states.

Coulomb interaction and many body terms play a crucial role in designing and implementing algorithms because the magnitude of these terms determines the energies of optical transitions. However, the magnitude of these terms can vary from nanostructure to nanostructure as a result of small changes in composition or size. Values for these parameters are currently deduced from spectroscopic data using non-optimized visual analysis without statistical confidence. The second focus of this dissertation is the development and demonstration of a novel statistically-valid Markov Chain Monte Carlo method for extracting precise experimental values from spectral data of a vertically stacked QDMs.

## Chapter 2

### PROPERTIES AND GROWTH METHODS OF NANOSTRUCTURED SEMICONDUCTOR MATERIALS

#### 2.1 Properties of Semiconductors

Semiconductor devices like transistors and p-n diodes are the foundation of all electronic devices and hence the modern world. The fundamental property of semiconductor materials is the variation of resistance as a function of temperature. This variation in resistance is caused by the presence of a gap in the material band structure. Understanding the origin of band structures and mechanisms to manipulate properties is the foundation of the research effort for developing novel semiconductor material platforms.

##### 2.1.1 Formation of Bands

Metals, insulators and semiconductors all have distinctive band structure. The origins of band formation can be understood by first considering the energy levels of a single isolated atom. Electrons of a single atom occupy quantized energy states. Bringing another identical atom into close proximity can result in the formation of molecule with molecular states that arise from the hybridization of individual atomic quantized states. This hybridization is a consequence of Pauli's exclusion principle which states two identical electrons cannot occupy the same quantum state (energy state) in a quantum system (molecule) simultaneously. Now, consider a crystalline semiconductor that has "N" atoms periodically arranged. Due to hybridization, the

available energy states split in “N” states with different energies. These hybridized states are closely spaced and resemble a continuum of states or a “band” of allowed energy levels. The states in these energy bands are not necessarily evenly spaced and are strongly dependent on interatomic distance. As the number of atoms reaches infinity, separate regions of allowed energy states can emerge. In semiconductors there are two such regions. The lower energy band is called the valence band (VB) and the higher energy band is called the conduction band (CB). The valence band is completely filled with electrons and cannot carry current unless some electrons are removed. The allowed states of the conduction bands are devoid of electrons, but if electrons are excited to the CB they can conduct current when electric fields are applied. The range of energies between the conduction and valence band for which no states exist is called the band gap. It is calculated from the difference between the lowest energy level of the conduction band and the highest energy of the valence band.

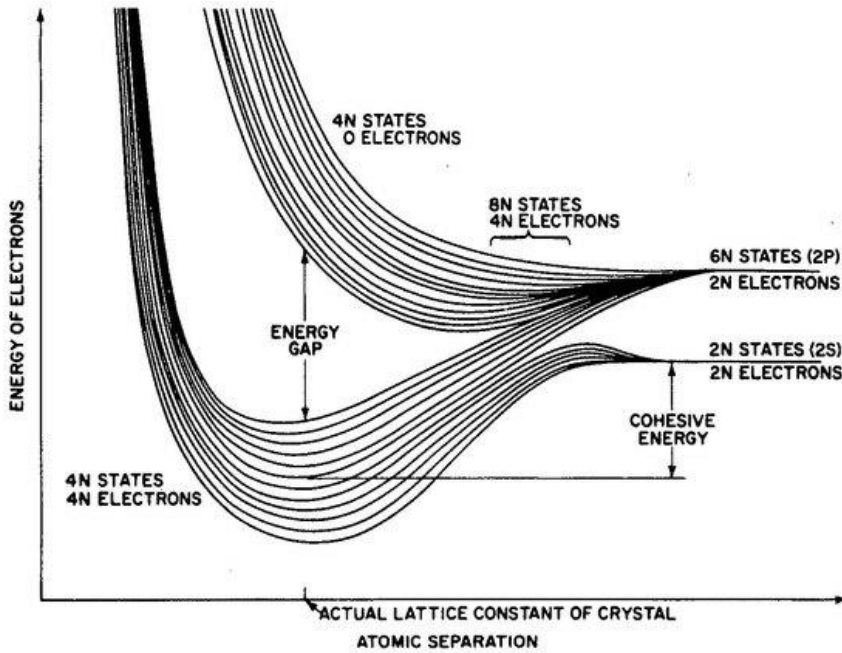


Figure 2.1: Band formation in diamond<sup>9</sup> depicting the energy gap between allowed continuum of states or bands.

### 2.1.2 Manipulation of Band Structure

Every semiconductor material has its characteristic band structure. Tailoring a material's band structure results in changed electrical properties. A pure semiconducting material made of only one element with no changes made to its composition is called a homogenous intrinsic semiconductor. One way of changing this system's band structure is by adding additional electrons or holes into the system. This method is called doping and the doped semiconductor is now called an extrinsic semiconductor. Another popular method of altering band structure is by growing or joining two semiconducting materials to form a heterostructure. The properties of the heterostructure are crucially dependent on the alignment of the CB and VB at the junction and the type of alignment classifies the heterostructure into straddling gap

(type I), staggered gap (type II) and broken gap (type III) heterostructures. The tailoring of band structures to fabricate heterostructures of desired optical and electronic properties is called band engineering.

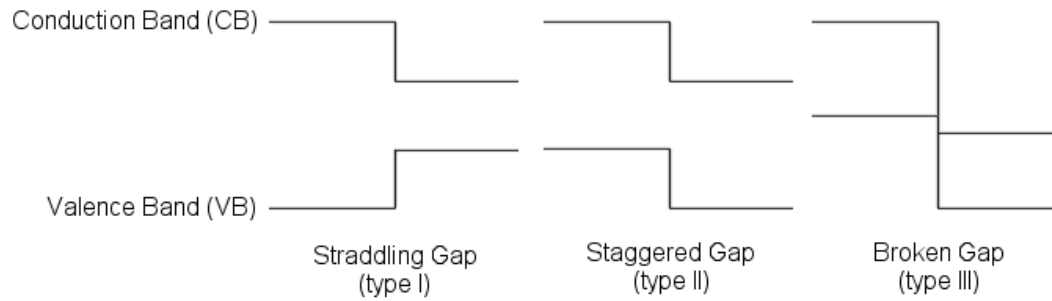


Figure 2.2: Three types of semiconductor heterojunctions organized by band alignment.<sup>10</sup>

## 2.2 Growth of Heterostructures

Bulk semiconductors are grown using Czochralski, Bridgman and Float zone processes. These industrial scale processes yield large single crystals of semiconductors with micrometer level control of composition. Crucial for band engineering is the ability to grow defect free heterostructures with high quality integration of the constituent elements. For band engineered heterostructures, epitaxial growth processes are used for fabrication as they allow accurate control at the nanometer length scale and an extremely pure end-product. Epitaxial growth processes, in principle, involve growing a thin crystalline layer on a crystalline substrate. These growth techniques can be categorized depending on direction of growth and material systems of used for the substrate and epilayer. The most commonly used epitaxial growth techniques are vapor phase epitaxy (VPE), liquid

phase epitaxy (LPE), solid phase epitaxy and molecular beam epitaxy (MBE). Vapor and liquid phase epitaxy use liquid and gaseous precursors to grow a monocrystalline film on a crystalline substrate. Solid phase epitaxy is a two-step process. The first step is the growth of an amorphous film on the monocrystalline substrate. In the next step, the substrate is heated under an ambient pressure which crystallizes the deposited film. The ErAs hybrid nanocomposite and InAs VQDMs studied in this dissertation have been grown using MBE.

### **2.2.1 Molecular Beam Epitaxy**

Molecular beam epitaxy, as the name suggests, is a thin film deposition technique where monolayers are grown on a clean substrate by molecular beams in an ultra-high vacuum chamber. The monolayers grown are extremely pure with minimal contaminants and control over the composition of each monolayer. The MBE machine's main components are the chamber, Knudsen effusion cells, a rotating heated substrate holder and RHEED (reflection high energy electron diffraction) set up. The MBE chamber (shown in Fig 2.1) is pumped down to ultra- high vacuum,  $10^{-13}$  mbar or more. Solid constituents are heated in the effusion cells until they slowly sublime. At such low pressures the vaporized elements form molecular beams and condense on the substrate. Rotating the substrate ensures a monolayer of uniform thickness. RHEED is used to ensure crystalline quality of the deposited layer. Heating elements and shutters to the effusion cells are computer controlled which allows precise control of the composition and thickness of the deposited layer. The rate of deposition is usually monolayers (lattice plane) per second. The glacial rate of growth is both a boon and bane for MBE grown films; on the one hand it allows a high degree

of control over the structures grown, but on the other hand it is an extremely expensive and slow method for fabricating devices.

MBE grown heterostructures with clean interfaces and atomically flat surfaces have enabled the expansion of our understanding of the fundamental material properties. They have also become critical as components of high-speed and high-efficiency electronics and optoelectronics. Material specific growth details for the novel heterostructures studied in this dissertation are discussed in the following sections.

### **2.3 Quantum Dots**

Quantum dots (QDs) are synthetic nanoscale boxes that can spatially confine charge carriers and excitons in all three directions. With their high quantum yield and malleable discrete energy levels that can be tuned with the size of the “box”, they are of great interest for applications ranging from single photon emitters<sup>11</sup> to biophotonics<sup>12</sup>. Depending on the method of synthesis, QDs are classified into two categories, colloidal QDs and epitaxially grown QDs.

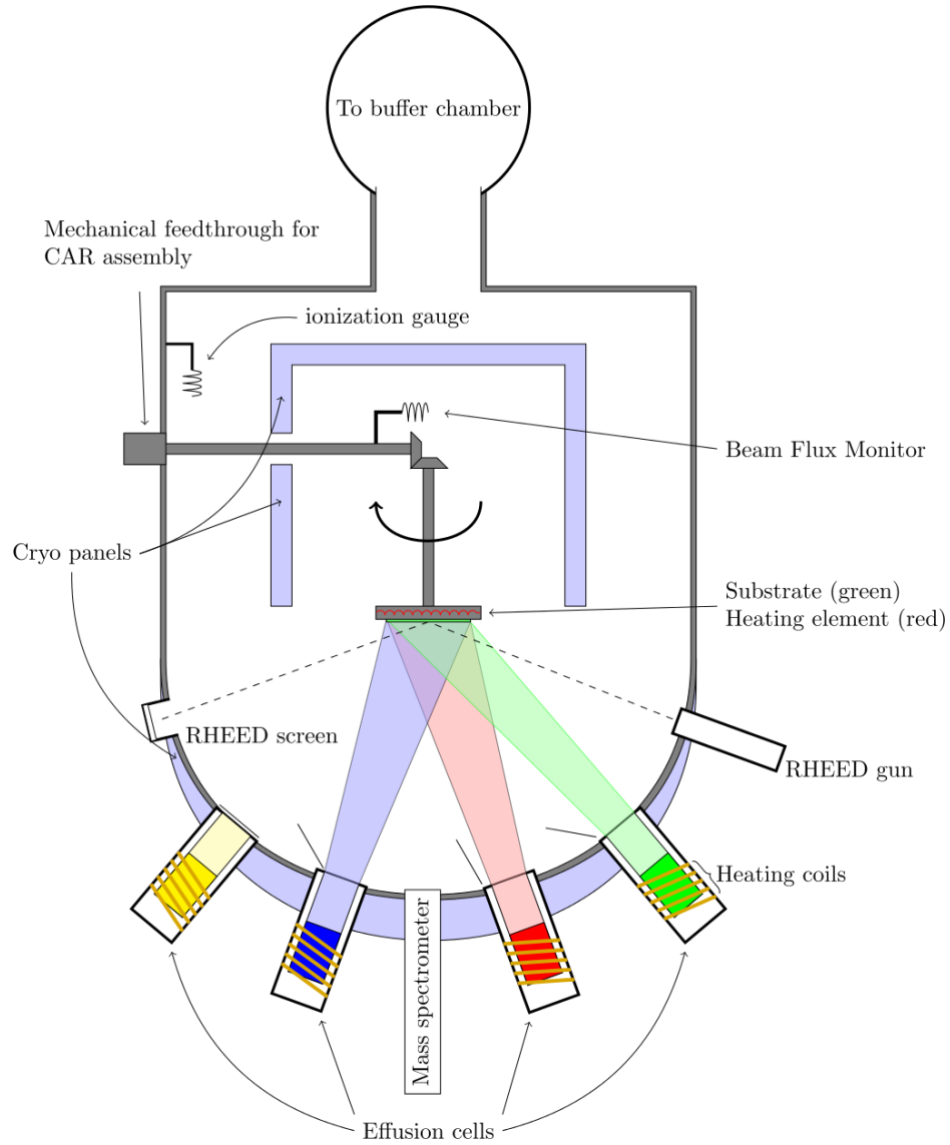


Figure 2.3: Schematic of a MBE machine with multiple effusion cells, a rotating sample holder and a RHEED screen.<sup>13</sup>

### 2.3.1 Confinement by Quantum Dots

A quantum dot can be conceptualized as larger band gap material surrounding a lower band gap material, forming an energy well for any charge particle within the “box”. A wave function ( $\Psi(x, t)$ ) of a charge particle is a mathematical representation

of the state of the charge particle in a quantum system. The time dependent Schrödinger equation describes the evolution of the wave function as a function of space (x) and time (t). It's one dimensional form is

$$-\frac{\hbar^2}{2m} \frac{\partial^2}{\partial x^2} \Psi(x, t) + V(x)\Psi(x, t) = i\hbar \frac{\partial}{\partial t} \Psi(x, t) \quad (2.1)$$

Here  $V(x)$  describes the particle moving in a region with varying potential energy and  $m$  is the effective mass. Let's consider the time independent Schrödinger equation which can be written as

$$-\frac{\hbar^2}{2m} \frac{\partial^2}{\partial x^2} \Psi(x) + V(x)\Psi(x) = E\Psi(x) \quad (2.2)$$

This equation also gives us  $E$ , which is the energy of the particle. The solutions for the time independent Schrödinger equation describe stationary states of the particle<sup>14</sup>. The movement of the charge particle in a QD can be described by the model of a charge particle in a finite square potential well. The energy of the particle can be described as

$$E\Psi(z) = -\frac{\hbar^2}{2m} \frac{\partial^2}{\partial z^2} \Psi(z) + V(z)\Psi(z) \dots\dots \text{Outside the well}$$

$$E\Psi(z) = -\frac{\hbar^2}{2m} \frac{\partial^2}{\partial z^2} \Psi(z) \dots\dots \text{Inside the well} \quad (2.3)$$

For a square well potential, the wave-function inside the well can be written as  $\psi(z) = A \sin kz$  or  $\psi(z) = A \cos kz$ , where  $A$  is the normalization constant and  $k$  is the wave number with definition of  $E = \frac{\hbar^2 k^2}{2m}$ .

Outside the wall the wave function can be described as  $\psi(z) = B \exp(\pm \kappa z)$ , where  $\kappa$  is defined in terms of  $V - E = \hbar^2 \kappa^2 / 2m$ .

To solve the equations and determine the allowed energy levels, the wave functions have to satisfy boundary conditions. These boundary conditions require  $d\psi/dz$  and  $\psi(z)$  to be continuous. Solving equations, we get the allowed energy levels which are defined as

$$E_n = \frac{\hbar^2}{2m} \left( \frac{n\pi}{L_z} \right)^2 \quad (2.4)$$

Here  $L_z$  is the size of the quantum well and  $n$  is the principle quantum number. The principle quantum number describes discrete energy levels of the system. This equation is extended to describe allowed energy a three-dimensional system with finite confinement. This three-dimensional confined system is a quantum dot with allowed energy levels of

$$E_n = \frac{\hbar^2}{2m} \left( \frac{n_x^2}{L_x^2} + \frac{n_y^2}{L_y^2} + \frac{n_z^2}{L_z^2} \right) \quad (2.5)$$

where  $L_x$ ,  $L_y$  and  $L_z$  is the size of the quantum dot in three dimensions, and  $n_x$ ,  $n_y$  and  $n_z$  is the principle quantum number along the three dimensions. From this equation we observe that in a confined quantum state, there are only discrete levels of allowed energy states. The second observation we make is that a particle is never found at the “bottom” of the box, it has a minimum energy which corresponds to  $n_{x,y,z} = 1$ . This minimum energy is called zero-point energy.

### 2.3.2 Growth of Epitaxial QDs

Epitaxial QDs can be grown using Molecular Beam Epitaxy (MBE) and Metal Organic Chemical Vapor Deposition (MOCVD) techniques. Each of these techniques has their own pros and cons and here we will focus on MBE grown QDs.

Early QDs were grown using the Cleaved edge overgrowth (CEO) technique<sup>15</sup>. This approach relies on MBE overgrowth of a cleaved multilayer MBE sample followed by another cleave and overgrowth along that cleave. Each cleave and overgrowth region form a Quantum well and the intersection of the three quantum wells forms the QD dot. Our InAs QD samples are grown by the more prevalent method of growing QDs, the Stranski-Krastanov growth (SK growth) technique. This is one of three primary modes of epitaxially growing thin films. This two-step growth mechanism was first recognized by Ivan Stranski and Lyubomir Krastanov and demonstrated in 1958 by Ernst Bauer, who classified the three growth modes for thin

films. In the SK method, growth relies on formation of coherently strained epitaxial islands due to strain and surface energy created by a small mismatch in lattice constants (1% to 8%) between the materials being grown and the crystalline substrate<sup>16</sup>. For growing the InAs QDs investigated here, first a few monolayers (ML) of InAs, called the wetting layer (WL), are grown on a crystalline GaAs substrate. Due to the 7% lattice mismatch between InAs (6.0583 Å) and GaAs (5.65325 Å), strain builds up within the InAs layer. As additional In and As atoms are added to the layer, the In and As diffusing on the surface settle into island of InAs that reduces the total strain and surface energy. The islands can then be completely covered in GaAs by continued deposition.

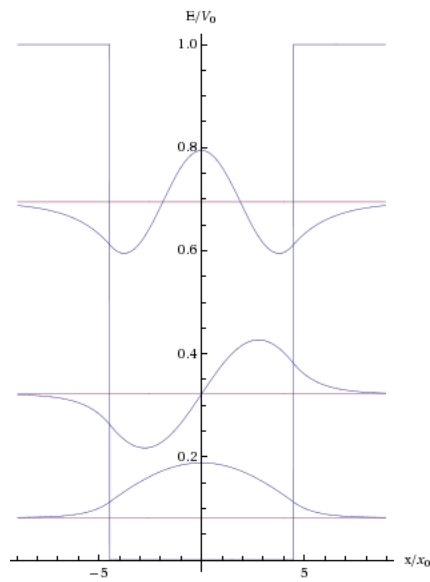


Figure 2.4: Schematic of lowest three discrete energy levels formed due to confinement in two dimensions.<sup>17</sup>

The covered islands of InAs behave as QDs, providing three-dimensional confinement of charge particles. The height of these QDs can be precisely controlled by the Indium Flush technique<sup>18</sup>. Here after the formation of the QDs, deposition of GaAs covers the QDs to the desired height, with the top of the QDs not covered. The temperature is increased slightly causing only the InAs to boil off due to its higher vapor pressure and leaving behind a truncated QD. GaAs is again grown on the sample covering the QD. The resulting QDs grown have a Type I band alignment. Epitaxially grown QDs are promising candidates for proving grounds for understanding the fundamental physics of QDs. These QDs have also been studied for applications in laser diodes and intermediate band solar cells as well as for understanding fundamental properties of single confined charges. With the ability to confine and manipulate single spin states, the most interesting avenue of application for MBE grown InAs QDs is quantum information processing(QIP). The biggest challenge in using QDs for QIP is the issue of scalability which arises due to the inhomogeneity in size and location of QDs on the substrate. This uncertainty in spatial location and precise state energy makes coupling to other QDs and photonic cavities difficult. Quantum dot molecules have unique features that provide a path to overcome the issue of scalability which will be described in the following sections.

#### **2.4 Quantum Dot Molecules**

Quantum dot molecules (QDMs) are two quantum dots with close spatial proximity that allows quantum mechanical tunneling of charge between the QDs. This tunneling can lead to the formation of molecular wavefunctions with bonding or antibonding symmetry analogous to the state of a hydrogen molecule. QDMs can be grown one on top of the other to form vertically stacked coupled QDs (VQDMs) or

laterally arranged by template growth to form lateral QDMs. The optical emissions of QDMs can be tuned in situ by the application of applied electric fields, which makes QDMs one of the prominent test beds for quantum devices.

#### 2.4.1 Properties of QDMs

QDMs can exhibit both inter dot (between two coupled dots) and intra dot (within the same dot) optical transitions. The relative energy levels of states in two QDs can be manipulated by an external electric field, which in turn controls the formation of the molecular bonding and anti-bonding states that can only be formed when states of two QDs are degenerate in energy. Optical spectra from VQDMs has demonstrated the formation of these bonding and anti-bonding states under an applied electric field.

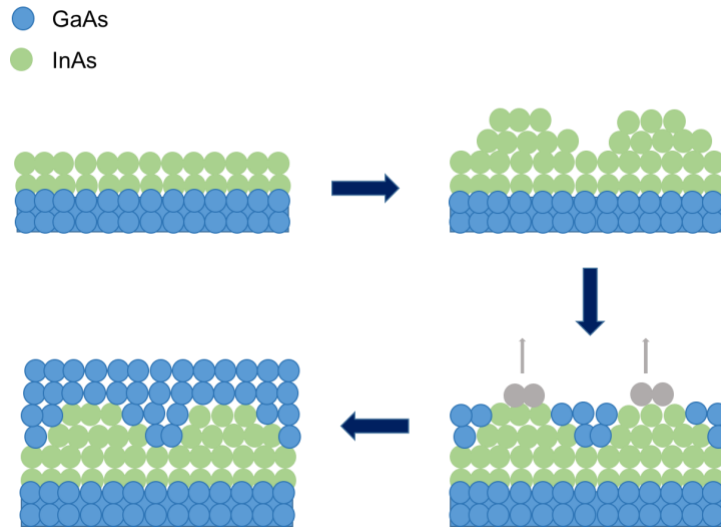


Figure 2.5: Schematic of the growth of a typical InAs/GaAs quantum dot

Figure 2.6 shows the PL emitted from a neutral exciton, the simplest optically observable charge configuration seen in VQDMs. A neutral exciton has a single electron and single hole. If both electron and hole are in the same dot (bottom left inset), the optical recombination is “direct exciton” and is identical to single QDs. The direct exciton has a PL energy with little dependence on applied electric field. If the electron and hole are in a different dot (top left inset), the optical recombination is unique to QDMs and called “indirect exciton” with a diagonal PL line. The energy of these indirect transitions can be tuned by an electric field, which creates the possibility of tuning these transitions into resonance with external device components such as a photonic cavity. We see an anticrossing (where the direct and indirect line should have intersected) due to the creation of hybridized states of the degenerate energy levels by the electric field. This anticrossing is the optical signature of coherent tunneling of charged particles between the QDs. The right inset in Figure 2.6, shows the formation of bonding and anti-bonding molecular states at the anticrossing.

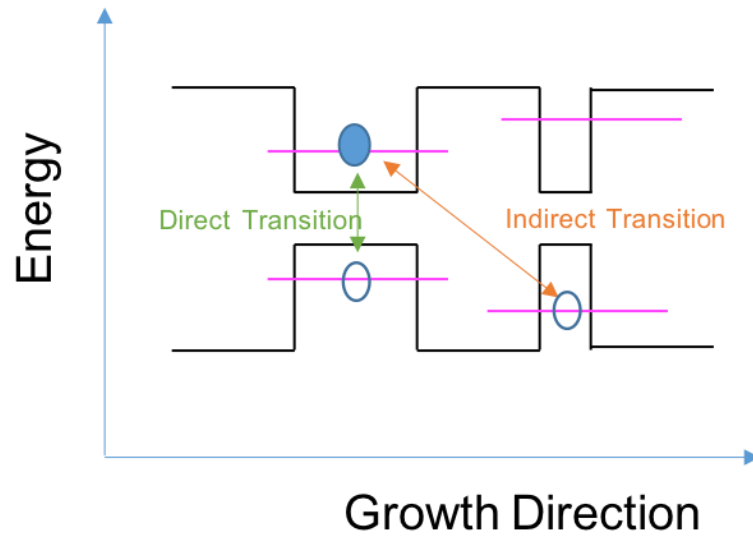


Figure 2.6: Schematic of the band diagram of a QDM along its growth direction

The bonding and antibonding states are delocalized over QDs and the barrier separating them. The similarity of these states to the hydrogen molecule leads to the name *QD Molecule*. The magnitude of the anticrossing, and the direct and indirect transition can be manipulated by careful engineering of the barrier and the applied electric field. These inter dot transitions which are unique to QDMs, provide another mechanism to manipulate quantum states, making them an attractive platform for QIP and for single photon/single charge based novel optoelectronic applications.

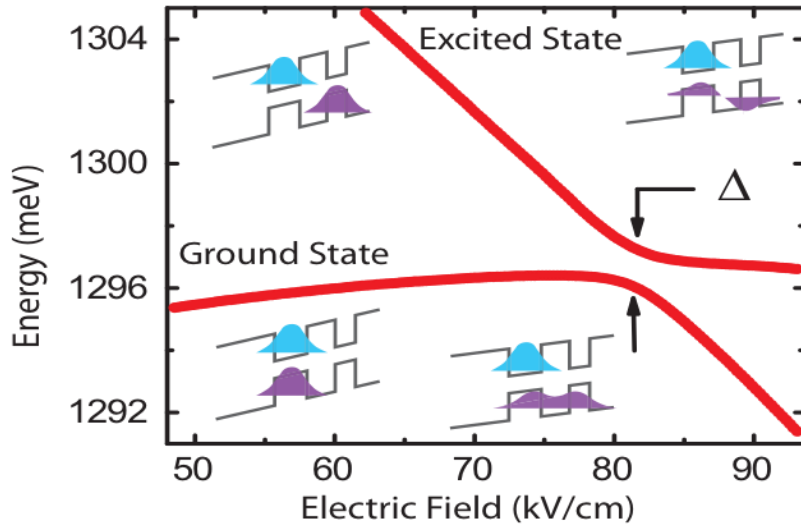


Figure 2.7: Photoluminescence of neutral exciton which exhibits the formation of molecular states and the anticrossing  $\Delta$ <sup>19</sup>

#### 2.4.2 VQDM growth mechanism

VQDMs are also MBE grown in the SK growth mode. First, a single layer of individual QDs are grown on a GaAs substrate. Second, a capping layer of GaAs is grown with predefined thickness to control tunnel coupling. Third, a second layer of InAs QDs is deposited on the capping layer. These QDs preferentially nucleate directly on top of buried QDs due to the strain propagation from the buried QDs. The alignment probability is inversely proportional to the thickness of the barrier layer. Preferential nucleation ensures tunnel coupling between nearly all QDs. The VQDMs studied in this dissertation are single pairs of coupled QDs, though this method can be extended to create columns with many stacked QDs.

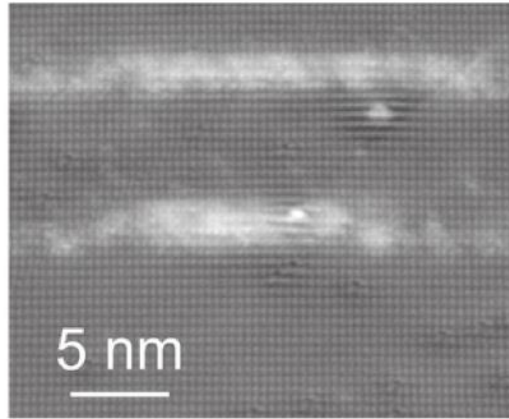


Figure 2.8: Cross-sectional STM image of vertically stacked InAs QDs<sup>7</sup>

## 2.5 Ln-V Nanocomposite material systems

Multiphase material systems with at least one of the constituent phases on the nanometer scale form the class of nanocomposite materials. This reduction in feature size brings into play “size effects” that result in material properties of nanocomposites substantially different from the properties of the individual components.

Lanthanide pnictides (Ln-V) grown in a III-V matrix are an interesting group of nanocomposites, particularly epitaxially-grown ErAs nanoparticles grown in a GaAs matrix. Ln-V nanoparticle (NP) systems can have an altered optical response that is important for the development of photoconductive switches, large area emitters, and photomixers. For each of these terahertz applications, Ln-V nanoparticle composites can meet the material requirements of these devices needing high dark resistance, short carrier lifetimes, and high mobility. Despite the many impressive properties of the ErAs NPs, very little is actually known about charge transfer mechanisms at the interface and through the bulk of the GaAs. The TRPL studies in Chapter 4 aim to understand the dominant mechanism of charge transfer through

GaAs separating an NP and a coupled QD. The following sections describe the growth and properties of ErAs NP.

### **2.5.1 Electronic Properties of ErAs NP in GaAs Matrix**

Bulk ErAs has a rock salt crystal structure with a lattice constant of 5.7427 Å. The initial motivation for studying Erbium was to develop a gain medium for lasers at 1.56 μm to be utilized for telecommunication<sup>20</sup>. Bulk ErAs is semi-metallic and its band gap is depicted in Figure 2.8.

The electronic nature of ErAs nanoparticles was a subject of significant debate because of effects of both size and strain. Theoretical modelling suggested the f-shell electrons of Er and the dangling p-shell electrons of the interface caused the material to behave as a semi-metal. Thus, according to these calculations, the pinning of the Fermi level mid gap would be independent of the confinement (size) of the ErAs NP<sup>21</sup>. Cross sectional tunneling microscopy and spectroscopy results showed a distance dependent decaying state 0.2 eV above the Fermi level<sup>1</sup>. This decaying state is attributed to interface and metallic states, confirming that NP of ErAs will have a high dark resistance and be a semi metal until their size passes a critical thickness. Time resolved difference optical reflectance for ErAs NP embedded in GaAs matrix measured 120 fs as its response time<sup>3</sup>. These properties of high mobility of charge particle, high dark resistance, and ultra-short lifetimes in a material system make it the perfect testbed for novel optoelectronic devices for Terahertz applications.

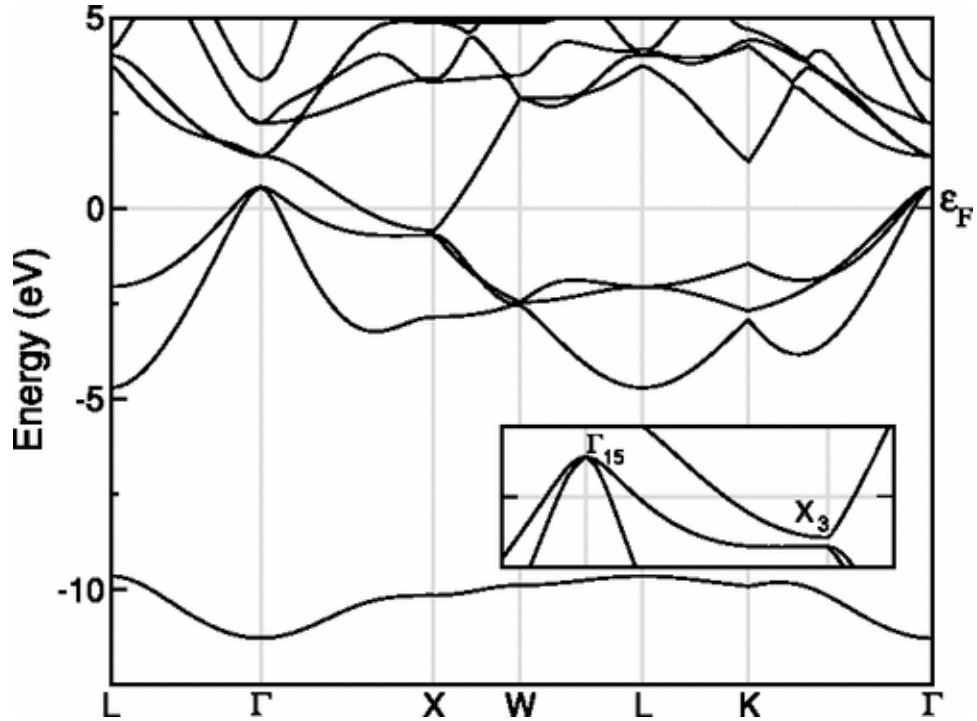


Figure 2.9: Bulk ErAs band structure<sup>22</sup>

## 2.5.2 Growth Processes for ErAs NPs

Ln-V nanoparticles in III-V material are primarily grown epitaxially through a) co-deposition during the growth of III-V materials or b) the growth interrupt method.

### 2.5.2.1 Growth via co-deposition

In this growth mechanism, Ln-V and III-V are grown simultaneously. During growth, the Ln atoms displace the group III atoms bonding with group V atoms on the surface. This process continues until the solid solubility limit of the III-V material is reached. Once the Ln concentration increases beyond this limit, Ln-V nanoparticles are formed randomly through the material. The size of the NPs is dependent on the substrate temperature and deposition rate<sup>23</sup>. The shape of the nanoparticles is also controlled by the concentration of Ln deposited and the orientation of the substrate<sup>24</sup>.

Over other methods of growth, co-deposition has the advantages of shorter growth times and the particles being closer together.

#### **2.5.2.2 Growth via Growth Interrupt**

Kadow et al. were the first to demonstrate the growth interrupt method<sup>25</sup>. The method uses the Volmer-Weber growth mode to form ErAs nano-inclusions in GaAs. The Volmer-Weber growth mechanism is also called the “island” growth mode where the attraction between the deposited atoms (here Ln) to each other is stronger than the attraction between atoms of the substrate material (here III-V) leading to the formation of three dimensional islands of the deposited material. For growing NP using this method, the first step is to grow a thin layer of III-V material. Then, the shutters for group III are closed, and Ln shutters opened. This pauses the growth of the III-V layer and Ln atoms displace the III group atoms and bond with group V atoms. After the critical thickness of 4 monolayers is reached, the crystal of Ln-V is stabilized by lateral expansion of the Ln-V nano inclusion. Continued deposition of Ln atoms leads to lateral expansion of the nano inclusions with the previously formed Ln-V NP acting as a nucleation site preventing further diffusion of the incoming Ln atoms. NP growth is then terminated by closing the Ln shutter and opening the group III shutter. The overgrowth of the III-V layer is templated on the lattice of the previously grown III-V layer. Eyink et al. showed pitting around ErAs NP due to GaAs overgrowth<sup>26</sup>. This pit was then used as a template to grow InAs QD directly coupled to ErAs under it, resulting in a coupled ErAs NP /InAs QD hybrid structure. By controlling the spacing between the NP and the QD we can manipulate the degree of coupling between the two material systems and thus the optical response from QDs.

## **2.6 Summary**

The next generation of optoelectronic devices with novel functionalities require precise design for the optimized incorporation of novel, nanostructured materials. Understanding the origin of these unique properties of these nanostructured materials, and how the properties depend on growth, is crucial for engineering the materials for applications. In this chapter, we summarized the electronic properties and methods for growing these nanostructured materials. In the next chapter, optical characterization techniques used to investigate these materials are described.

## **Chapter 3**

### **OPTICAL CHARACTERIZATION OF LOW DIMENSIONAL SEMICONDUCTORS**

The optical response of a material can be influenced by many material properties, including composition, structure, stress, thickness, and electronic (band) structure. Because optical measurement techniques are almost always non-contact, require minimal sample preparation, and typically have high sensitivity, they are a powerful and common tool to investigate new material systems<sup>27</sup>. I use time-integrated and time-resolved photoluminescence spectroscopy to study low dimensional semiconductor heterostructures. In this chapter, I review these optical characterization techniques.

#### **3.1 Photoluminescence (PL)**

The principle behind photoluminescence is the excitation of an electron from the valence band of a semiconductor to the conduction band, forming an electron-hole pair. These electrons and holes can relax to the lower energy levels, typically by non-radiatively emitting phonons. If the optical selection rules are satisfied and electrons and holes remain spatially proximate, the electron and hole can eventually recombine and emit a photon of equal or lower energy than the photon that initially generated the electron hole pair.

### 3.1.1 Principal Components of a PL spectroscopy set up

The fundamental photoluminescence experimental set up has 4 main components: the collimated coherent exciting source (usually a laser), the temperature-controlled sample holder, a monochromator, and a detector.

Lasers with exciting photon energies tuned to transitions of interest are used to selectively excite only the energy states under study. The temperature-controlled sample holder enables cooling of the sample, in our case down to temperatures as low as 4 K. At room temperature, spectroscopic data is always contaminated by non-radiative recombination processes and thermal broadening. The thermal broadening of emission lines is approximately  $kT/2$  where  $k$  is the Boltzmann constant, thus cooling samples allows one to obtain narrower lines and differentiate between closely spaced lines<sup>28</sup>. In our case, low temperatures are also important to keep electrons and hole confined within the low energy states of the semiconductor nanostructures we are investigating<sup>29</sup>. The monochromator and the detector, along with passive optical components such as mirrors and lenses, are optimized to ensure maximum light collection. . The monochromator is an optical device that separates the different wavelength components of incoming light by using a diffraction grating. The grating causes the different wavelengths to diffract at different angles, resulting in spatial dispersion. The degree of dispersion is dependent on the groove density on the gratings. Our spectrometer uses three different diffraction gratings, with groove density of 150 grooves/mm, 600 grooves/mm and 1100 grooves/mm. The diffracted light is incident on a liquid nitrogen cooled Charge Coupled Device detector, which is a one dimensional (linear) or two dimensional (area) multichannel array detector built of individual elements known as pixels. Each of the elements converts the impinging photons into charge. At the end of the measurement, the read-out electronics measure

the individual element's charge and converts it into a count. This monochromator-detector combination is often referred to as a spectrograph and allows us to resolve spectral lines and measure the intensities of different wavelengths. The spectrograph we use is a  $\frac{3}{4}$  m Acton spectrometer with a Si detector CCD manufactured by Princeton instruments. The resolution of our measurement is dictated by the length of the spectrometer and the pixel size of CCD. The spectral resolution of this set up is about 70  $\mu\text{eV}$ .

Another kind of photon detector that can be coupled to a monochromator is the Avalanche Photo diode (APD). The APD is essentially a strongly reverse-biased photodiode that is triggered into breakdown with an incoming photon. In other words, an absorbed photon creates an avalanche of carriers by impact ionization. This results in a measurable current. If the APD is triggered by a photon event, it can't detect another event for a period of time called dead time. If another photon event occurs during dead time, the detector does not count it and that can lead to artificially short lifetimes. To overcome this, the incoming photon rate should be kept at a fraction of the repetition rate of the pulsed laser. Since the APD is triggered by the photons, stray photons from sources other than the laser or the sample affect the signal to noise ratio of the measurement. These stray photon counts are known as dark counts and can be defined as the counts registered by the APD when photons from neither the laser or the sample are counted by the APD. These counts can vary between tens to thousands of counts per second.

### **3.2 Optical absorption and emission in low dimensional semiconductor heterostructures**

Excited electrons and holes typically relax to the lowest energy states of the conduction and valence band before recombining to emit PL. Consequently, the energies of emitted PL can be used to understand the energy levels and mechanisms of charge transfer between such energy levels in novel low dimensional semiconductor heterostructures. For the InAs QDs grown on a GaAs substrate studied in this dissertation, the mechanism for non-resonant PL excitation and detection is as follows. First, the charge carriers are excited by a coherent light source (laser at 780nm). The energy of the incoming photon is greater than the bandgap of the GaAs, generating electrons in the conduction band and holes in the valence band. The energy of the electron and hole is determined by the energy of the absorbed photon and is above the band edge. The optically-generated electron and hole relax to the lowest available energy states, which are the lowest energy levels of the InAs QDs ( $E_0$  for electrons and  $H_0$  for holes) as shown in the schematic, Fig 3.1. The electrons and holes in the lowest energy states then undergo either radiative or non-radiative recombination. Photons emitted through radiative recombination are collected as photoluminescence. The lifetime of the electron-hole state that undergoes spontaneous recombination to release energy radiatively is called the radiative lifetime of that state. Luminescence from the lowest state can be seen under low excitation powers. PL from higher energy states can be observed by increasing the laser fluence or energy. PL from higher energy states occurs when the photon arrival rate is faster than the radiative lifetime of the lower states, which results in saturation of the lower states and population of the higher energy states by electrons and holes relaxing into the QD. Escape of carriers by any mechanism other than photon emission can limit the observed PL lifetime to be

shorter than the “natural” radiative lifetime. In this way, PL lifetimes can be used to measure the rate of carrier escape from the QD.

In the case of the vertical quantum dot molecules we study here, PL can be observed from a variety of closely spaced low energy levels, even without saturation of the ground states. This occurs for two reasons. First, the states are close enough in energy that there is a reasonable thermal distribution of electrons and holes over these states even at low temperature. Second, relaxation through the discrete states of QDs is somewhat slower than in continuous bulk bands, and therefore the different carrier relaxation pathways lead to temporary occupation of the slightly higher energy levels.

The energy of a photon emitted from an InAs QD is

$$h\nu = E_n - H_n = E_G^{InAs} + \frac{(\hbar\pi n)^2}{2ma^2} \left( \frac{1}{m_e^{InAs}} + \frac{1}{m_h^{InAs}} \right) + E_{Coulomb} \quad (3.1)$$

The term  $\left( \frac{1}{m_e^{InAs}} + \frac{1}{m_h^{InAs}} \right)$  is the optical effective mass of the generated exciton.  $E_{Coulomb}$  is the coulomb interaction energy between the electron and the hole. The energy of the emitted photon can also be calculated by subtracting the Eigenvalues of the initial and the final state Hamiltonians, which we will describe in detail in Chapter 5.

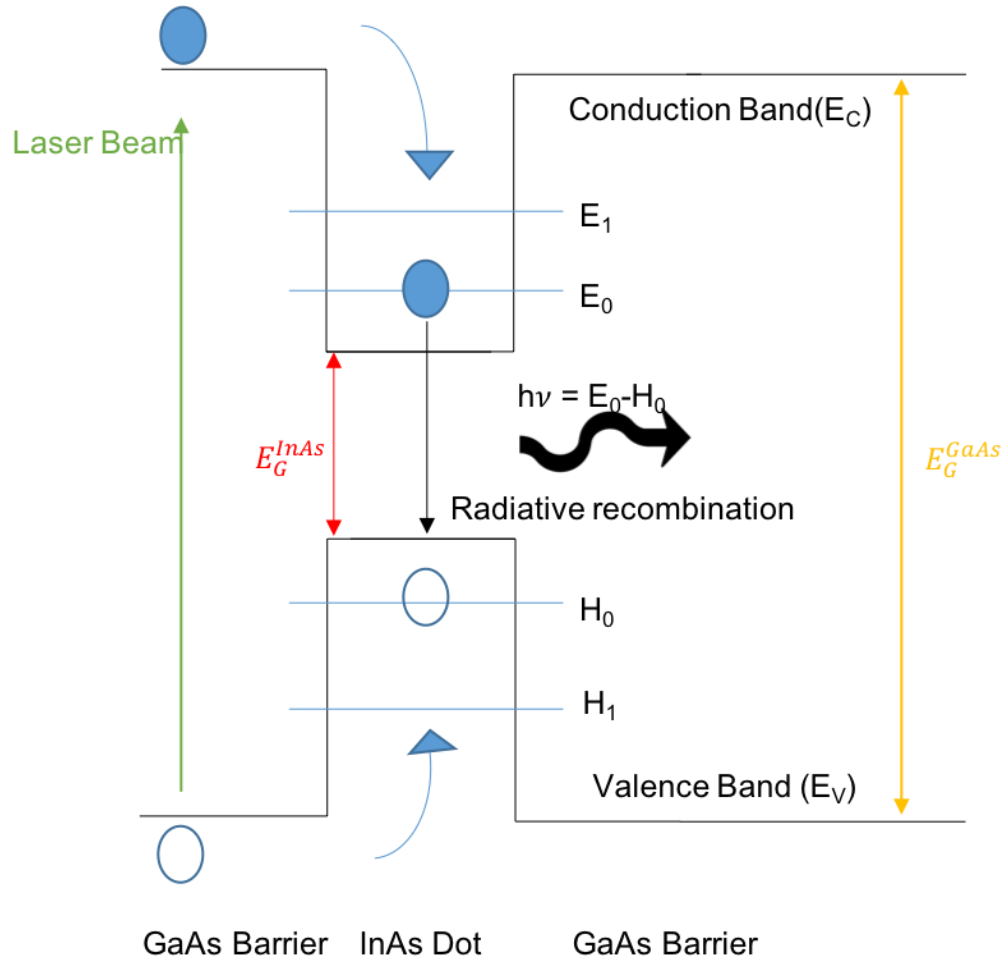


Figure 3.1: Schematic of PL generation under non-resonant excitation conditions

### 3.2.1 Optical selection rules

Whether or not an electron and hole can recombine to emit a photon is determined by optical selection rules. Using the dipole approximation technique, we can calculate the optical transition matrix element to define these optical selection rules. Fermi's Golden Rule give us the optical transition rate between an initial state  $i$  to a final state  $j$  and can be written as

$$\Gamma_{i \rightarrow j} = \frac{2\pi}{\hbar} |\langle j | H' | i \rangle|^2 \rho \quad (3.2)$$

Here  $\rho$  is the density of states and  $|\langle j|H'|i\rangle|^2$  is the matrix element that gives us the optical selection rule<sup>30</sup>. This element is directly proportional to spatial location (i.e. wave function overlap of the electron and hole) and only couples states of different parity to conserve total angular momentum. Wave function of a particle in the particle in a crystalline material can be described by Bloch wave written as

$$\psi(r) = e^{ik \cdot r} u(r) \quad (3.3)$$

Here  $k$  is the crystal wave vector,  $r$  is the spatial position, and  $u$  is the periodic function for the crystal under study<sup>31</sup>. The total quantum mechanical wave function includes both the envelope function and the Bloch wavefunction for the charge particle. Both these wavefunctions play a significant role in the optical transitions. In InAs QDs, interband transitions, which are the optical transition between the ground electron and hole states, are allowed because the Bloch wave functions have opposite symmetries, i.e. even for conduction band and odd for valence band. For intraband transitions, transitions are only allowed for the between ground and excited states for electrons when envelope functions have different symmetries<sup>32</sup>. These selection rules are strictly defined for circularly symmetric QDs. In practice the selection rules can be broken due to the asymmetric lens-like shape of QDs, but the “allowed” states by this rule remain the brightest transitions.

### 3.2.2 QD Photoluminescence under electric field

We study VQDMs as a function of applied electric field. There are two consequences of applying electric field to QDs. The first is the band bending that pushes the electron and hole wave functions in opposite directions. The second is the changing of the energy levels relative to both one another and the Fermi level.

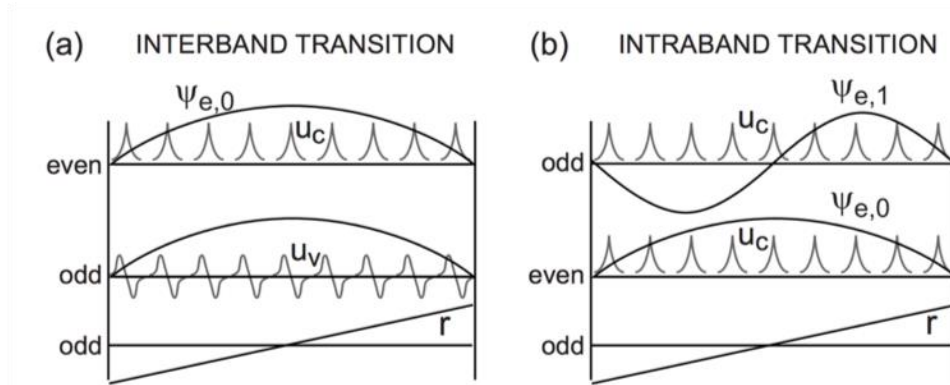


Figure 3.2: Interband and intraband transitions in a quantum dot (a) Different symmetries of Bloch waves for conduction and valence band allow optical transition (b) Intraband transition are allowed due to the different envelope functions<sup>32</sup>

The separation of electron and hole wavefunctions results in a reduced overlap integral that reduces the recombination efficiency and thus the intensity of the emitted PL when compared to PL with no applied electric field. The shift in energy and intensity for optical recombination of confined carriers and excitons is called the quantum confined stark effect (QCSE) and the shift in energy is called the Stark shift. For vertically applied electric field parallel to the growth direction, the energy of the transition decreases quadratically with applied field.

For QDs and QDMs grown on doped substrates applying an external electric field also results in deterministic charging of the QD or QDMs. As depicted in Figure 3.4, by applying an electric field we tune the energy level of the QDs across the Fermi level of the doped substrate. This tuning allows for controlled and sequential tunneling of charge particles into the QD. Such charges, which are present in the QD before any optically generated carriers are added, are called spectator charges. These spectator charges always have an influence on the PL of the QD, and each injection or charging

event results in sharp shifts in the PL energy. This shift is called the Coulomb shift. The inherent Coulomb interaction energy due to the spectator charges needs to be overcome as each additional charge is injected from the Fermi sea of the doped substrate. Each charge complex has a characteristic Coulomb shift energy, with the direction depending on the net charge of the exciton. This is often used as an identifying signature for each charge complex. A detailed description of charging events in VQDMs is given in Chapter 5.

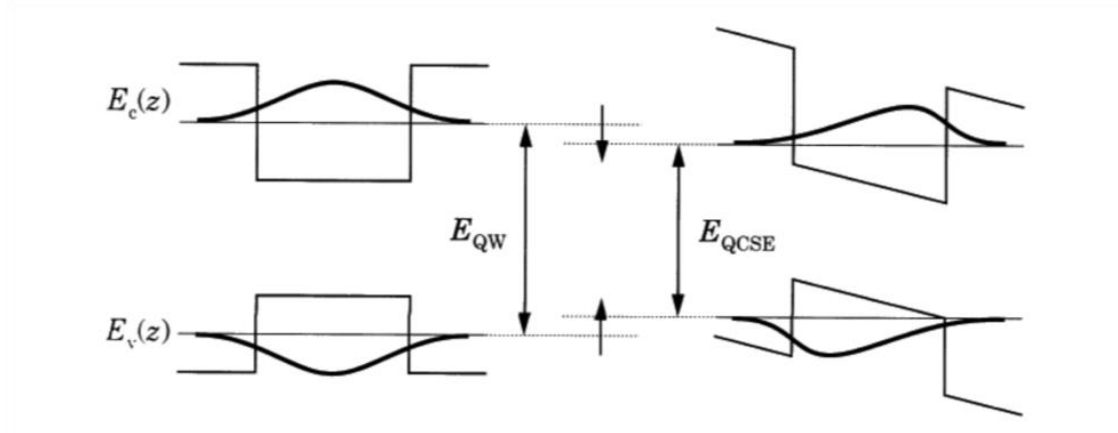


Figure 3.3: Band diagram for a quantum well with (b) and without (a) external applied field which reduced the energy of both bound states and wavefunction of electron and hole are pushed on opposite directions of each other reducing the overlap integral<sup>33</sup>

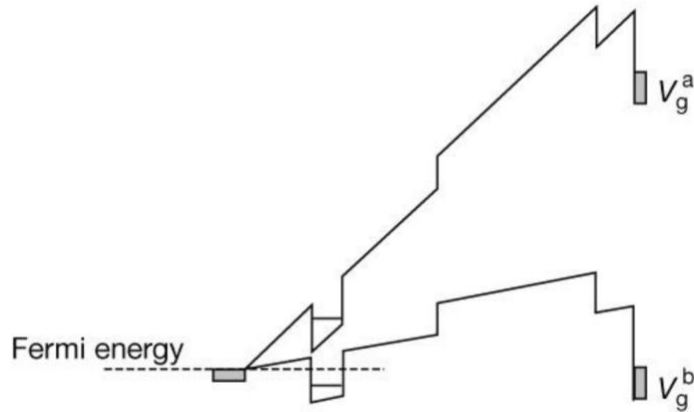


Figure 3.4: Tuning of the energy levels of a QD across the Fermi sea of the doped substrate upon application of an electric field (flatter band)<sup>34</sup>

### 3.3 Time integrated photoluminescence spectroscopy

As described in Chapter 2, a pair of vertically stacked InAs QDs grown on GaAs substrate are studied using time integrated photoluminescence (TIPL). Because the barrier between the two QDs is relatively thin, three new features emerge. First, electrons and holes in separate QDs can recombine because the barrier is sufficiently thin that their wave functions overlap. The optical transition energy of such indirect excitons tunes strongly with applied electric field. Second, when energy levels of the two QDs are in resonance, coherent tunneling of charge carriers between the two quantum dots leads to the formation of molecular states. Third, the Coulomb interaction terms become more complex. In single QDs, only the number of spectator charges has to be considered. In QDMs, the spectator charges can be in one of two QDs, requiring that both the number and spatial location of each charge be considered. All of these properties of QDMs provide important opportunities for building devices. For example, for designing a photonic cavity coupled QDM, we would need precise

exciton energies to enable strong resonant coupling with the modal frequency of the photonic cavity. A deeper understanding of the energy levels, Coulomb interactions, and the dependence of these properties on external fields is necessary to design devices that leverage these properties.

Developing a deeper understanding of quantum dot molecules requires the study of emission from quantum states that are limited to one photon per emission cycle. Good signal to noise ratio is achieved by increasing the acquisition time of the spectrometer. The long integration times also result in multiple charge states being observed on the spectral map - the number of spectator charges can vary within the integration time, which covers many cycles of excitation and recombination. We repeat the time integrated photoluminescence measurement for a series of applied electric field values, which tunes the energy states of the QDM across the Fermi level of the doped substrate and changes the relative energy levels of the two QDs.

### **3.3.1 Optical set up**

An extended cavity tunable diode CW laser is the excitation source that excites the biased QDM sample at 895 nm. The excitation wavelength is selected to excite carriers only in the InAs wetting layer. We use an external cavity diode laser (ECDL) manufactured by Sacher lasertechnik in the Littman- Metcalf configuration. The laser beam travels through an optical isolator that prevents back reflections from returning to and damaging the laser head. The laser beam is coupled into a single mode optical fiber from Edmund optics using a fiber coupler. Coupling into a fiber coupler is done using two mirrors that allow us to control the optical angle of the beam to ensure the highest coupling efficiency, typically around 50%. The output of the fiber is attached to an optical table built onto our magneto-optical cryostat. The beam passes through a

power stabilizer and then onto the beam splitter that directs the laser off a mirror, through a window, and into the sample column. The sample column holds a 6 foot insert. At the bottom of the sample insert we have the QDM sample mounted on Attocube piezoelectric nano-positioners. A high aperture objective lens is used to excite the sample and collect the emitted PL, which returns along the same optical path. The same beam splitter is used to route the collected PL into a separate optical fiber that directs the light into a spectrometer. Optical filters are used to suppress any laser light in the PL output path.

### **3.3.2 Helium cooled open cycle Cryostat**

A schematic for this system is shown in Figure 3.5. The sample is mounted on an insert that is lowered into the sample space of the cryostat. A capillary tube connecting the sample space to the He reservoir controls the flow of liquid helium into the sample column. The cold He gas from the liquid He boil off cools the sample to 4 K. Superconducting magnetic coils within the helium reservoir generate a magnetic field of 9T in the vertical direction (parallel to the sample column) and 4 T in the horizontal direction, allowing generation of a magnetic field of 3.5 T at arbitrary angles. The thermal load on the liquid Helium space is reduced by a vacuum jacket and a liquid Nitrogen reservoir. A Helium liquefaction system recovers and recondenses much of the liquid Helium.

### **3.3.3 Time integrated PL spectrum**

Displayed in Figure 3.6 is a typical raw time integrated PL bias map. It has three axes, namely energy, applied voltage, and intensity. These three-dimensional maps are formed by acquiring sequential spectra (PL intensity vs energy) as a function

of electric field. The reds, yellows, and oranges indicate a higher count of photons on the CCD. In Chapter 7, we describe the development of a template using Markov Chain Monte Carlo methods to extract statistically valid precise information about the Coulomb interaction terms, tunneling coefficients, and exciton energy values from data such as that displayed in 3.6.

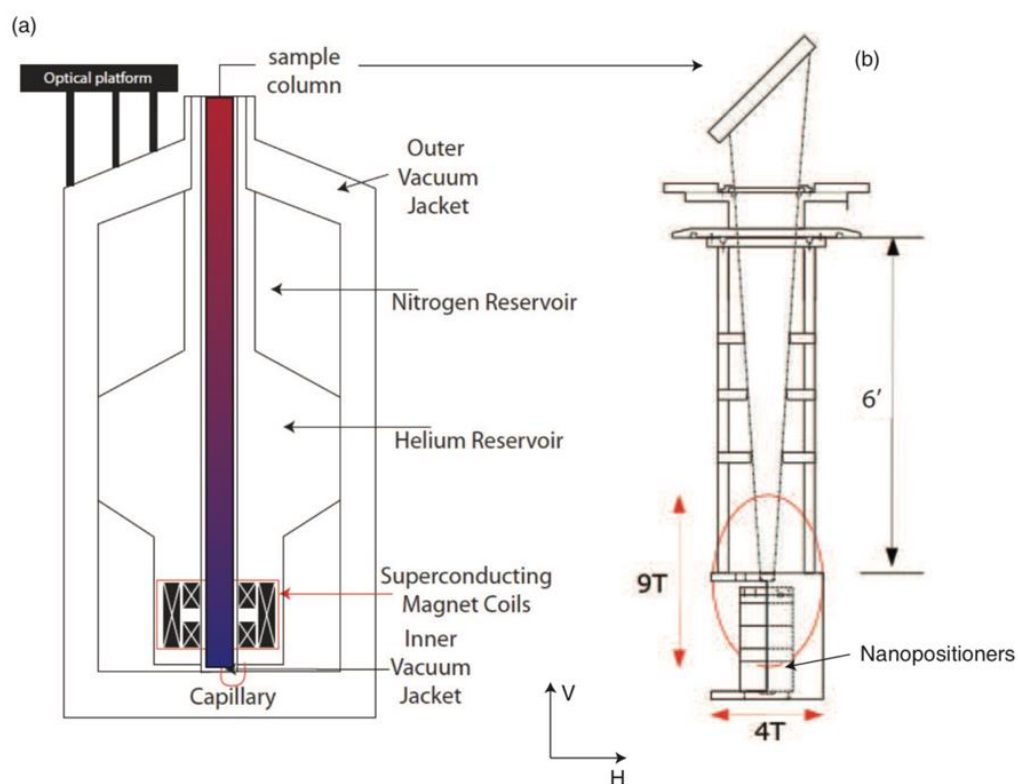


Figure 3.5: (a) Schematic of the Janis superconducting magnet system. The color in the center column depicts the gradient of the temperature. (b) Schematic of the sample insert of the sample column<sup>35</sup>.

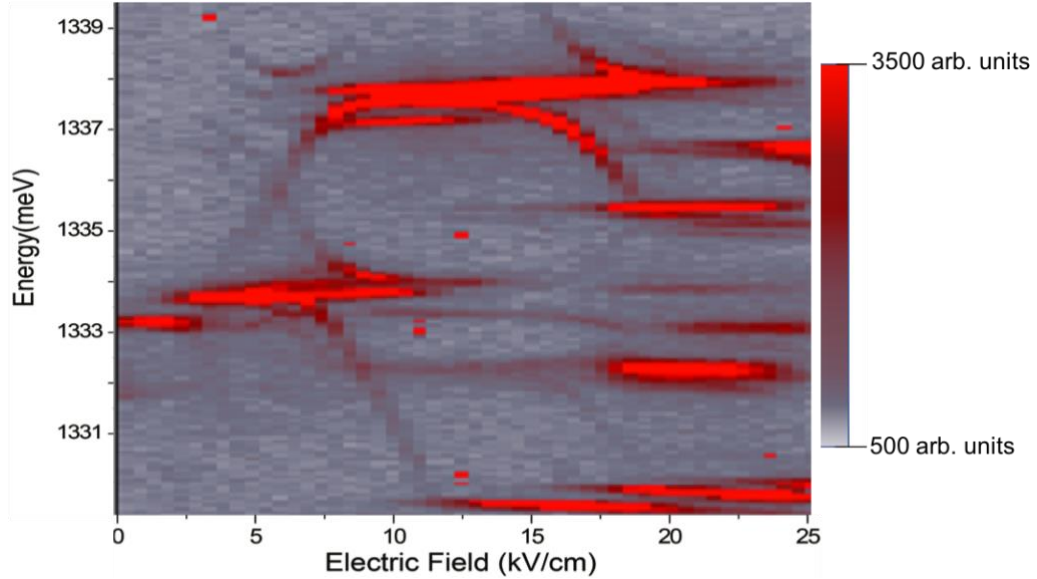


Figure 3.6: TIPL from VQDM of sizes 2.9 nm and 2.6 nm separated by a 6 nm GaAs barrier including 3 nm of AlGaAs at the center of the barrier under an applied electric field.

### 3.4 Time Resolved Photoluminescence Spectroscopy

Time resolved photoluminescence (TRPL) spectroscopy is a modification of traditional photoluminescence measurements. This technique has been used extensively to study defect densities, carrier lifetimes, and charge carrier dynamics. The components unique to this technique are an APD, counting electronics, and a pulsed laser, the rest of the components are the same as a time integrated system. TRPL is the investigative technique used in this dissertation to study the charge carrier transfer mechanism in ErAs:GaAs nanocomposites as described in Chapter 2. A schematic of the TRPL system used is provided in figure 3.7.

The principle behind this technique is measuring the time between excitation and emission of an optically generated electron-hole pair. Light from a pulsed laser excites charge carriers in the sample under study. Depending on the material

properties of the sample, the excited charge carrier pair radiatively or non-radiatively recombine. Counting electronics create a histogram of the time delay between each excitation pulse and the resulting emitted photon for a large number of excitation instances. This histogram is then fit to extract the PL lifetime.

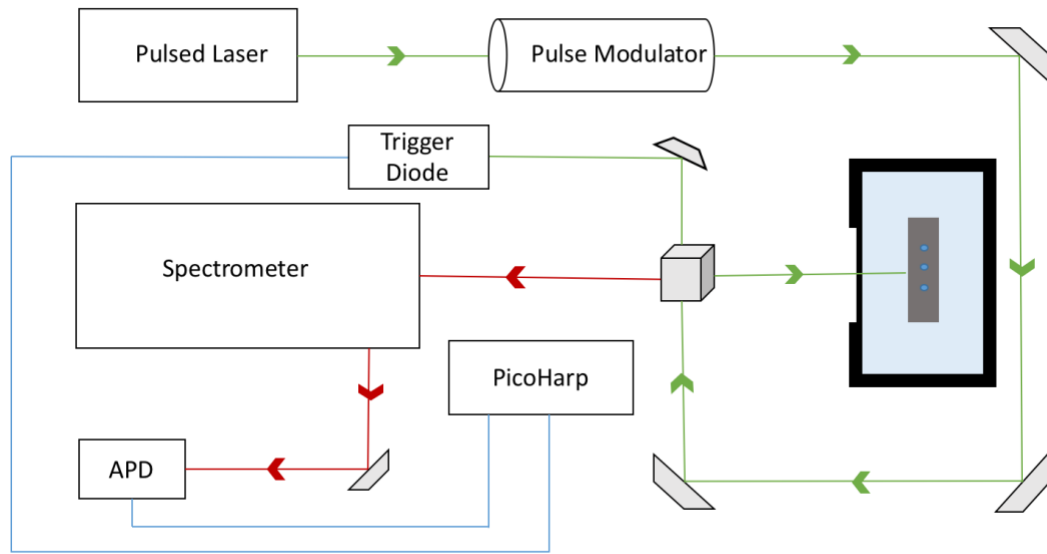


Figure 3.7: Schematic of the TRPL set up used to study ErAs:GaAs nanocomposites

In this set up, the pulsed laser light from the Mira-900 Ti:Sapphire with a repetition rate of 76 MHz is used to optically create electron hole pairs in the InAs QD. This repetition rate results in a 13.2 ns window between each laser pulse. To evaluate materials with lifetimes longer than the fundamental repetition rate of the laser we use a ConOptics Pulse Modulation system. This system suppresses pulses using crossed polarizers and allows select pulses to pass through by rotating their

polarization by applying large electric fields to a medium whose degree of birefringence depends on the applied field. This technique is called pulse picking and the system is often referred to as the pulse picker.

The cryostat used for our TRPL experiments is an Advanced Research Systems closed cycle cryogenic refrigerator. Mounting the sample in this system allows us to conduct measurements as a function of temperature. For this system, the lowest temperature measurement is carried out at 7 K. Using the filtration techniques described in the previous sections, the intensity of laser light entering the spectrometer is suppressed. For TRPL measurements, a side port mirror guides the dispersed PL from the grating through a slit onto an APD whose function is described below. The slit width and the groove density of the grating allows us to control the spectral range incident on the APD.

We use time correlated single photon counting for our TRPL studies. In this approach, the electrical pulse generated by the APD when it detects a photon is sent to a PicoHarp counting module. In parallel, a trigger diode detects the excitation pulses from the laser. The PicoHarp system calculates the time delay between each detected photon and the next excitation pulse, then computes the excitation – emission delay by subtracting the repetition rate of the laser. The PicoHarp software generates a histogram of the number of photon detection events as a function of the delay time, which is a measure of the lifetime of the excited charge carriers. The histogram is analyzed using Fluofit software. Previous TRPL studies reported lifetimes of .9 ns<sup>36</sup> for similar ErAs nanocomposite structures, which is comparable to the instrument response function (IRF) of our counting electronics. To remove instrumental bias, the histogram was deconvolved with the IRF measured at the start of the experiment.

Fluofit performs deconvolution fits with a non-linear least squares estimation based on the Levenberg-Marquardt and maximum likelihood estimation algorithms. Test decay times are generated using Monte Carlo estimation methods, these values are then compared against the data set and the residuals are calculated. The software repeats this process until it reaches lifetimes with the lowest residuals.

## Chapter 4

### USING TIME RESOLVED PHOTOLUMINESCENCE TO UNDERSTAND ENERGY TRANSFER MECHANISMS IN ERAS NANOCOMPOSITES

As discussed in chapter 2, nanocomposite materials exhibit unique “bulk” material properties that can be tailored by varying the constituent components. For example, the inclusion of Ln-V nanoparticles within a III-V host can have a significant impact on carrier dynamics, increasing dark resistance<sup>3</sup>, reducing carrier lifetimes<sup>25</sup>, and increasing mobility<sup>3</sup>. Consequently, Ln-V / III-V nanocomposites can play a key role in the development of improved THz optoelectronic devices such as photoconductive switches, large area emitters, and photomixers. The incorporation of both ErAs nanoparticles and InAs QDs within GaAs forms a hybrid composite in which both carrier dynamics and optical absorption and emission can be controlled<sup>26</sup>. This particular class of composite has been studied extensively in the last decade to understand how the physical and chemical properties of the constituent elements, as well as their relative spatial proximity, lead to the optical and electronic properties of the hybrid composite material<sup>37</sup>. Studies have established that the concentration of ErAs NP and their spacing relative to InAs QDs alter the intensity and lifetime associated with charge carriers from the QDs<sup>36</sup>. Intensity dependent TRPL measurements on such a system showed that the ErAs NPs are semi-metallic<sup>36</sup>. Similarly, the temperature independence indicates that phonons do not play a role in energy transfer within this system<sup>36</sup>. However, the specific mechanism of energy transfer from InAs QDs to ErAs NPs remains unclear, with tunneling and Förster

resonance energy transfer (FRET) as the leading candidates. Here we use TRPL measurements of a series of samples with varying structure and composition to clearly establish tunneling as the dominant mode of energy transfer in these materials.

#### **4.1 Förster resonance energy transfer (FRET)**

Observed first in the early 1920s by G. Cario and J. Franck<sup>38</sup>, the first complete quantitative theory for FRET was developed by Theodor Förster in the late 1940s<sup>39</sup>. In this energy transfer mechanism, the excited donor species transfers energy to an acceptor species if the transfer energy matches the available energy transitions in the acceptor. If the donor and acceptor are sufficiently coupled to one another, the excited acceptor may also simultaneously transfer energy back to the donor<sup>40</sup>. This synchronous energy transfer is exhibited in the form of energy transfer resonance analogous to tuning forks transferring their energies once struck. FRET is based on Coulombic interactions and is strongly dependent on the relative dipole orientation of the particles involved. The energy transfer is virtual, in the sense that no photon is emitted or absorbed. FRET results in quenching of the donor emission intensity, reduction in the donor lifetime, and increase in the acceptor emission which is detected using FRET microscopy<sup>41</sup>.

FRET has been studied extensively in the field of analytical chemistry as the dominant mode of non-radiative energy transfer between chromophores. The efficiency of FRET is extremely sensitive to distance, which allows FRET to be used to measure sub nanometer distances in, for example, metabolic pathways. For this reason, FRET is often called the “Spectroscopic ruler”<sup>42</sup>.

The rate of energy transfer ( $k_T$ ) between the donor and acceptor particles is given by

$$k_T = k_D \left(\frac{R_0}{r}\right)^6 = \frac{1}{\tau_D} \left(\frac{R_0}{r}\right)^6 \quad (4.1)$$

where  $k_D$  is the emission rate constant of the donor in the absence of FRET,  $\tau_D$  is the lifetime of the donor,  $r$  is the distance between the donor and acceptor, and  $R_0$  is the distance at which emission and transfer are both equally probably, i.e.  $k_D = k_T$ <sup>42</sup>. This distance is characteristic property of a material system and is known as the Förster radius. This critical radius can be calculated by the following expression

$$R_0^6 = \frac{9 \ln 10}{128 N_A \pi^5} \frac{\kappa^2 Q_D J}{n^4} \quad (4.2)$$

in which  $N_A$  is the Avogadro's number,  $n$  is the average refractive index of the medium separating the donor and acceptor and  $Q_D$  is the quantum yield of the donor particle in the absence of the acceptor<sup>43</sup>.  $J$  is the normalized overlap integral defined as

$$J = \int \frac{f_{D\lambda}(\lambda) \varepsilon_A(\lambda) \lambda^4 d\lambda}{\int f_{D\lambda}(\lambda) d\lambda} \quad (4.3)$$

where  $f_{D\lambda}(\lambda)$  is the donor fluorescence per unit wavelength and  $\varepsilon_A(\lambda)$  is the molar absorption coefficient. Both these quantities are wavelength specific and the overlap terms represents spectral overlap between the donor and acceptor particles.  $\kappa^2$  is the dipole orientation factor, which can be calculated as follows

$$\kappa = \cos \theta_T - 3 \cos \theta_D \cos \theta_A \quad (4.4)$$

$\theta_T$  is the difference between the dipole moments between the donor and acceptor, and  $\theta_{D(A)}$  is the dipole moment of the donor (acceptor) particle.  $\kappa^2$  varies between 0 (perpendicular transition moments) and 4 (collinear transition moment)<sup>44</sup>. For fluids this value is usually taken to be  $2/3$ <sup>44</sup>, however for systems where the particles are constant but can be randomly orientated,  $\kappa^2$  is taken to be  $0.476$ <sup>45</sup>.

The efficiency of FERT is sixth inverse power dependent on distance between donor and acceptor, and can be written as

$$E = \frac{1}{\left[1 + \left(\frac{r}{R_0}\right)^6\right]} \quad (4.5)$$

## 4.2 Tunneling

Tunneling is a quantum mechanical phenomenon where there is a finite probability of a charge carrier passing through a potential barrier with energy greater than that of the charge carrier. The probability of tunneling is dependent on the composition and size of the barrier. Tunneling probabilities or rates can be extracted for both simple single barrier and complex multiple barrier systems by calculating flux transmission and reflection coefficients for the systems.

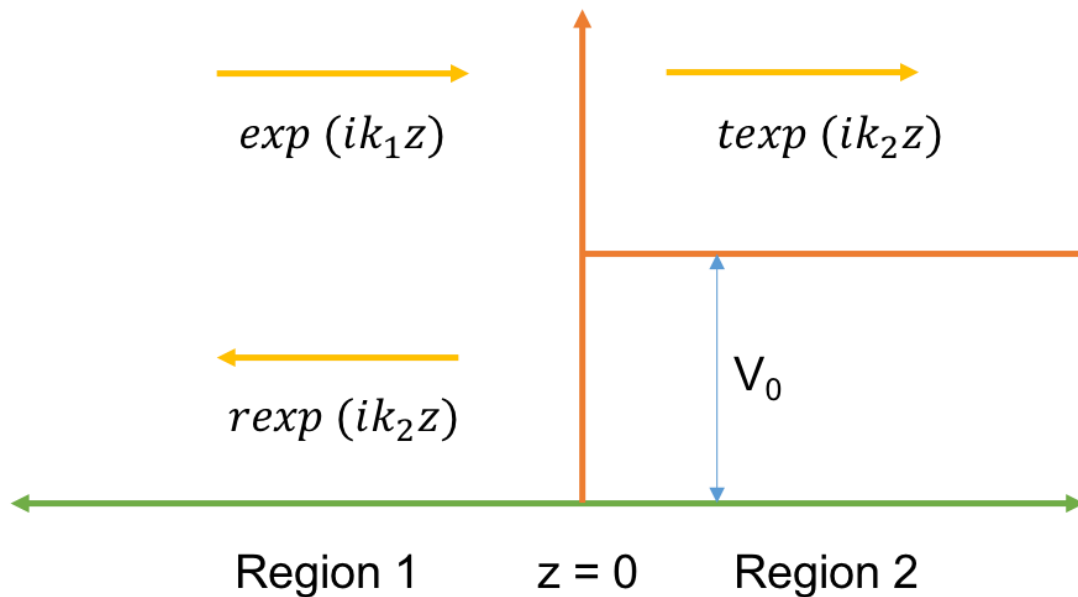


Figure 4.1: Potential step barrier at  $z = 0$ , the potential on the left is 0 and on the right is  $V_0$

Let's consider a simple single step barrier at  $z = 0$  in which the wave function for an incident particle has energy  $E$  and the potential energy height of the barrier is  $V_0$ . At the interface the solutions to the Schrödinger's equation can be written as

$$\psi(z) = \begin{cases} A \exp(ik_1z) + B \exp(-ik_1z), & z < 0 \\ C \exp(ik_2z) + D \exp(-ik_2z), & z > 0 \end{cases} \quad (4.6)$$

where  $k_1$  and  $k_2$  are wavenumbers for the incoming and outgoing waves at the barrier which can be defined as  $k_1^2 = \frac{2mE}{\hbar^2}$  and  $k_2^2 = \frac{2m(E-V_0)}{\hbar^2}$ . For continuity the slope and values of the wave functions have to be equal at the barrier. This boundary condition allows the calculation of coefficients on both sides of the barrier as described in Figure 4.1. In this scenario, the potential is big enough to have no travelling wave from the opposite side of the barrier. Using this simplification, we can further reduce equation 4.6 to get  $t$  and  $r$  values as

$$t = \frac{2k_1}{k_1+k_2} \quad , \quad r = \frac{k_1-k_2}{k_1+k_2} \quad (4.7)$$

Transmissions and reflection flux coefficient are calculated for this case with the energy of the particle being greater than the barrier.

$$T = \frac{\hbar k_2/m_2}{\hbar k_1/m_1} |t|^2 \quad (4.8)$$

$$R = |r|^2 \quad (4.9)$$

For the case  $E < V_0$ , no flux is carried by the wave across the barrier, i.e. no current is carried by a decaying wave and  $k_2$  is replaced by  $ik_2$ .

For complex multi barrier situations we depend on Transfer Matrices commonly known as the T matrix method. This method was first formulated by P.C Waterman for modelling scattering of EM waves<sup>46</sup>. This boundary matching

technique couples the amplitude coefficients of the wave functions on the left and right of the barrier in the following manner

$$\begin{pmatrix} C \\ D \end{pmatrix} = T^{21} \begin{pmatrix} A \\ B \end{pmatrix} = \begin{pmatrix} T_{11}^{(21)} & T_{12}^{(21)} \\ T_{21}^{(21)} & T_{22}^{(21)} \end{pmatrix} \begin{pmatrix} A \\ B \end{pmatrix} \quad (4.10)$$

where  $A, B, C$  and  $D$  are the amplitudes of the wave functions on either side of the barrier as described in Equation 4.6. We can find transmission and reflection amplitudes for the case described in Figure 4.1, where the wave function is reflected from the barrier with the amplitudes of the reflected and transmitted wave function is  $r$  and  $t$ . Using these assumptions, we get,

$$\begin{pmatrix} t \\ 0 \end{pmatrix} = T \begin{pmatrix} 1 \\ r \end{pmatrix} \quad (4.11)$$

Solving this for elements of the T matrix we get

$$r = -\frac{T_{21}}{T_{22}}, \quad t = \frac{T_{11}T_{22} - T_{12}T_{21}}{T_{22}} \quad (4.12)$$

These values can be used to calculate the  $T$  and  $R$ , from which we can calculate tunneling rates. The T matrix formulism can be extended to multiple barrier scenarios. Flux coefficients are strongly dependent on wave numbers which are in turn dependent on the relative energy levels of the barriers. These energy levels can be controlled by compositions, and the size and dimension of the nanostructures.

### 4.3 Hypothesis for the experiment

Charge transfer mechanisms in ErAs nanocomposites are temperature and intensity independent<sup>36</sup>. This narrows down the probable mechanisms of charge transfer to FRET or tunneling. FRET depends weakly on barrier composition through the dielectric constant. Tunneling depends strongly on composition through the height of the potential barrier. We hypothesize that tunneling is the dominant mechanism. If

this is true, changing the composition to significantly increase the potential energy height of the barrier will result in a significant decrease in the rate of carrier escape from the QDs and thus a significant increase in the PL lifetime.

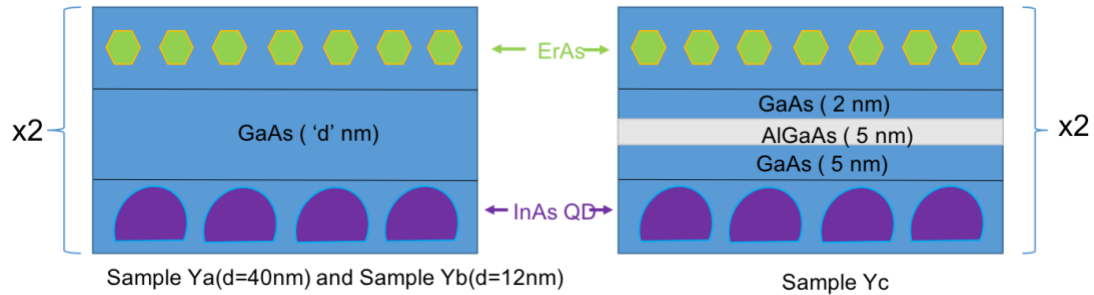


Figure 4.2: Schematic of a single period of ErAs nanocomposites studied using TRPL

#### 4.4 Sample structure

The three nanocomposites studied were grown by MBE at the Air Force Research Laboratory using the growth interrupt technique. These samples consist of 2 periods of a heterostructure. Each period comprises a layer of InAs quantum dots (QDs), a barrier layer and ErAs nanoparticles. The InAs QDs were fabricated by depositing 2 ML of InAs on a GaAs substrate using the SK method as described in chapter 2. The thickness and composition of the barrier layers makes each of the samples unique. Barriers of samples Ya and Yb are made of GaAs with thickness of 40 nm and 12 nm respectively. In contrast, the barrier of sample Yc has 5 nm of AlGaAs within the GaAs barrier of total thickness 12 nm. The variation in composition and barrier thickness allows us to resolve the individual contributions of FRET and tunneling. We first studied these samples using fluence-dependent photoluminescence to determine the lowest ground state of the QD. The ground state

energy of the QD for the three samples was at 1040 nm (1.19 eV). We then used TRPL to study the lifetime of the ground state of the InAs QDs in each sample to determine the difference in energy transfer rate.

#### **4.5 Temperature dependent TRPL**

TRPL measurements of this sample were acquired by the system described in Chapter 3. The excitation laser was centered at 780 nm and the emitted PL was collected by a microscope objective with numerical aperture of .65. The injection laser was filtered out with an 800nm long pass filter to prevent contamination of data. The three samples were studied under various excitation laser fluences (0.51 mJ/cm<sup>2</sup> to 64 mJ/cm<sup>2</sup>) and under different temperature (7K to 137K) conditions. Figure 4.2 shows the decay time for the three samples at 7K under varying fluence conditions.

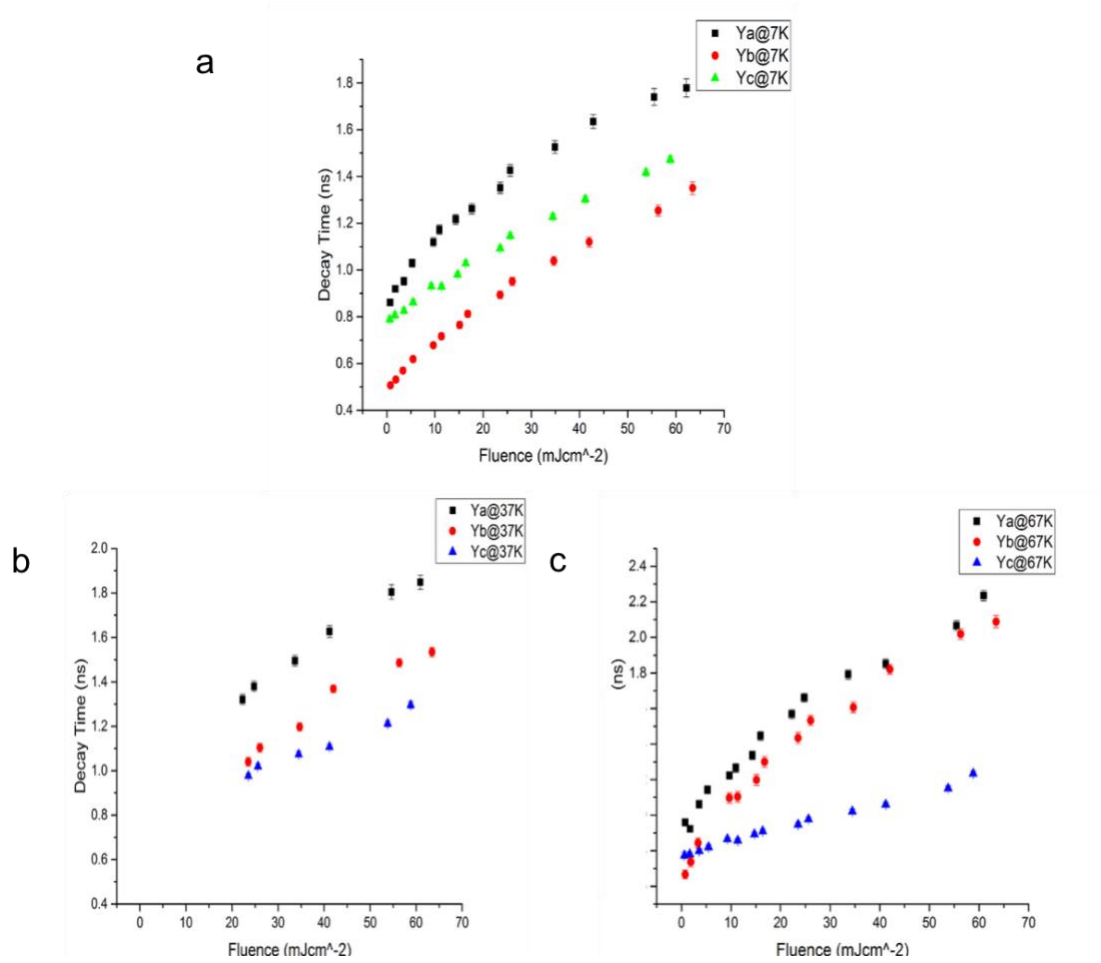


Figure 4.3: Decay time measured as a function of exciting laser fluence at (a) 7K, (b)37K, and (c)67K

From the decay time measurements in Figure 4.2, fluence dependence of the decay time is observed. Past TRPL measurements on a ErAs nanocomposite fabricated in a similar manner as the samples studied in this dissertation established their semi-metallic nature<sup>36</sup>. Semi-metallic states are not saturable. As a result, we assign the observed fluence dependence to defects in the interface or the barrier and not originating from the ErAs NPs.

The decay lifetimes for all three samples showed a significant difference between the sample with and without the AlGaAs in the barrier as shown in Figure 4.2. We observe an approximate difference of .25 ns between the decay times of the sample without (Yb, red, 4.2 (a)) and with AlGaAs (Yc, green, 4.2(a)) at 7K. We also note a difference in decay time for samples Yb and Yc at 37K (4.2(b)) and 67K (4.2(c)). The barrier thickness for samples Yb and Yc is identical at 12 nm, but their composition is different. Specifically, sample Yc contains AlGaAs, which has a much higher conduction band edge than GaAs and thus a higher tunneling barrier. The increased PL decay time for the sample with AlGaAs in the barrier indicates a reduced carrier escape rate, consistent with energy transfer via tunneling. We next determine if FRET is consistent with the observed changes in lifetime by computing the Förster critical radius and transfer efficiency.

#### **4.6 FRET calculations**

From equation 4.2, we know that the Förster critical radius  $R_0$ , has a weak dependence on the refractive index of the medium of transfer. We calculate Förster radii for three nanocomposite structures, 1) a nanocomposite structure with a 12 nm barrier of pure GaAs, 2) a 12 nm barrier of pure AlGaAs, and 3) a 12 nm barrier with composition mirroring the composition of Yc, i.e. with both AlGaAs and GaAs in the barrier. We note that the thickness of each of these barriers is the same, but the refractive index is different. For the third structure, the refractive index was calculated using the effective medium approximation, computing the effective refractive index by using average of the GaAs and AlGaAs refractive indices, weighted by the fraction of each material in the barrier<sup>47</sup>. The dipole orientation factor was assumed to be 0.476 as orientation of InAs QD and the ErAs NP with respect to each other could be random

but is fixed<sup>45</sup>. The normalized spectral overlap value was calculated to be  $1.7632 \times 10^{16}$  using the absorption and emission data from analysis of similar nanostructures<sup>48</sup>. If we assume an ideal scenario with  $Q_D$ , the quantum yield, of InAs being 100%, we find Förster radii of 4.0512 nm, 4.344 nm and 4.1636 nm for the nanocomposites with barriers made of pure GaAs, pure AlGaAs, and mixed AlGaAs and GaAs respectively. Next, we calculated the efficiency of the FRET as a function of distance for these material systems. We determined that the efficiency of FRET transfer drops to 0% at barrier thickness of 10 nm as shown in the Figure 4.3. There are two important conclusions that can be drawn from this analysis. First, FRET is unlikely to be a significant energy transfer mechanism for barrier thicknesses of 12 nm. Second, the difference in FRET efficiency between GaAs and pure AlGaAs is never more than 10.4% and between GaAs and mixed GaAs/AlGaAs is never more than 4.1%. In contrast, the difference in PL decay rate between sample Yb and Yc is 25%. This confirms that the change in refractive index induced by replacing some of the GaAs barrier with AlGaAs cannot lead to a large enough change in FRET efficiency to explain the observed change in PL decay rate.

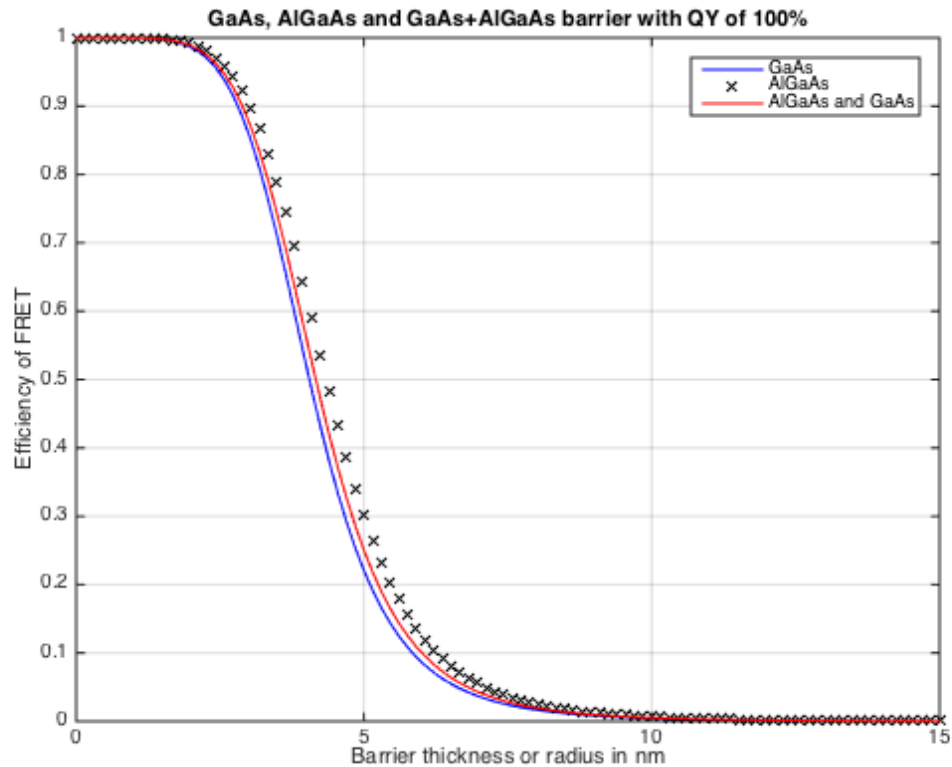


Figure 4.4: FRET efficiency as a function of thickness of the barrier composed of pure GaAs, pure AlGaAs, and AlGaAs and GaAs.

#### 4.7 Conclusions

Developing an understanding of charge transfer mechanism in ErAs hybrid nanocomposites is crucial for using these materials for future optoelectronic devices. To determine the dominant charge transfer mechanism in these systems, unique barriers were engineered to resolve individual contributions for the competing possible energy transfer mechanisms of tunneling and FRET. TRPL measurements were made on two ErAs hybrid composite structures each with equal barrier thickness but different composition and potential barrier height. Decay time measurements revealed a significant difference in the values for each of the samples. We then calculated the

Förster critical radius for each of the structures. We find that FRET efficiency drops to 0% at 10 nm and varies by less than 10% for samples with and without AlGaAs. Combining the experimental observations and computation model allows us to conclude that tunneling is the dominant mode of energy transfer.

## Chapter 5

### EXTRACTING PHYSICAL PARAMETER VALUES FROM QDM SPECTROSCOPY DATA

#### 5.1 Introduction

Quantum Dot Molecules (QDMs) are a promising platform for Quantum information processing (QIP) systems. With the capability to tune their emission frequency both during growth (by changing the size of QDs) and in situ (by applying electric fields), they can be engineered to couple to modal frequencies of photonic crystals (PC) and waveguides, providing a path to scalability that is not available with single QDs. Time integrated PL measurements have been extensively used to study single QDs and VQDMs.

#### 5.2 Structure of the VQDM studied

The VQDMs studied here are composed of two vertically stacked InAs QDs separated by a GaAs and  $\text{Al}_{0.3}\text{Ga}_{0.7}\text{As}$  barrier as shown in Figure 5.1. The top dot is 2.9 nm and the bottom dot is 2.6 nm. The VQDM structure is grown using MBE by the In flush technique discussed in chapter 2. This structure is then embedded in a n-type Schottky diode to allow precise tunability of the QD's energy levels relative to one another and the Fermi level of the doped substrate when an external electric field is applied. The difference in size and range of applied electric fields causes electron energy levels to be similar allowing coherent tunneling of the electron at certain values of the applied field. The relative difference in the size of the two QDs and the resulting

difference in hole state energies within this range of electric fields would normally cause holes to relax quickly to the top QD when the barrier is pure GaAs. The presence of the AlGaAs in the barriers leads to the formation of a metastable state: a “spectator” hole can be trapped in the higher energy ground state of the bottom dot.

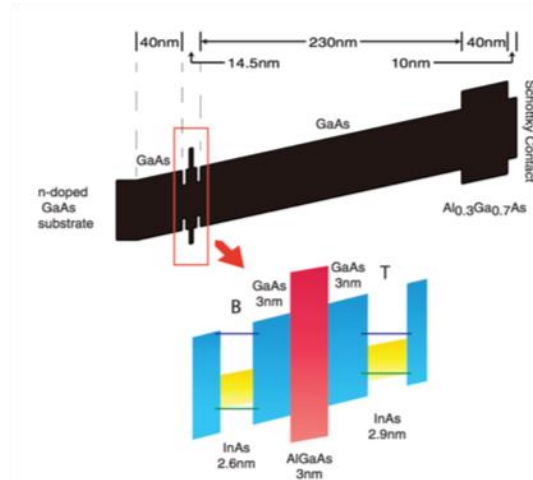


Figure 5.1: Schematic band diagram, composition, and size of VQDM sample studied.

### 5.3 Time integrated PL data from a QDM

Time integrated photo luminescence spectroscopy of VQDMs as a function of applied field generates a raw PL bias map, as shown in Figure 5.2 (a). Figure 5.2 (b) is generated from Figure 5.2 (a) using the traditional method of picking and plotting the points of highest PL intensity for each applied electric field value. Analysis of this extracted data (Figure 5.2(b)) is one of the best and most extensively used methods to analyze the energy level structure and charge interactions in nanostructured materials such as VQDMs.

In Fig 5.1(b) we observe several charge complexes, which we can identify through their characteristic spectroscopic signatures<sup>6,8,49</sup>. They include a single electron and hole pair forming a neutral exciton ( $X^0$ , green lines), a neutral exciton with an excess hole ( $X_h^0$ , black lines), a double negatively charged trion ( $X^{2-}$ , blue lines), and a double negatively charged trion with an excess hole ( $X_h^{2-}$  purple lines).

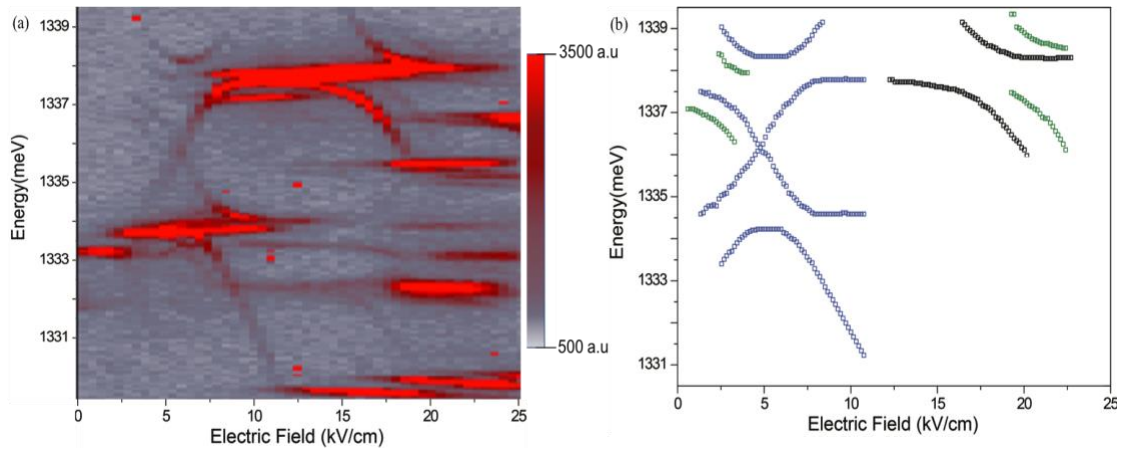


Figure 5.2: (a) Raw time integrated PL map from VQDM of sizes 2.9 nm and 2.6 nm separated by separated by a 6 nm GaAs barrier including 3 nm of AlGaAs at the center of the barrier under an applied electric field (b) Extracted TIPL map

Each charge complex is described completely using Hamiltonians with basis states. The following sections describe the formation of each charge state and the Hamiltonian used to describe it.

#### 5.4 Notations

For the following sections, we use  $\begin{pmatrix} e_T & e_B \\ h_T & h_B \end{pmatrix}$  to describe the atomic like states of VQDMs and the location of charges in the VQDMs.  $e_B(e_T)$  are the number of

electrons in the bottom (top) dot and  $h_B(h_T)$  are the corresponding number of holes. Underlines indicate charge carriers involved in photon emission. For example,  $\begin{pmatrix} 0 & \underline{1} \\ 1 & \underline{1} \end{pmatrix}$  describes optical emission from the  $X_{+h}^0$  state in which the electron and hole from the bottom dot recombine to emit the photon. The  $\begin{pmatrix} e_T & e_B \\ h_T & h_B \end{pmatrix}$  notation is also used to describe the basis states for the Hamiltonians that describe each state in the presence of applied electric fields and tunnel coupling between the two QDs. The Eigen energies of the system are computed by finding the eigenvalues of the matrix Hamiltonians that include these interactions. Differences in energy between the initial and final state Hamiltonians describe the energy of optical transitions, e.g. PL emission. i.e.

$$H_{PL} = H_f - H_i \quad (5.1)$$

Manybody terms or coulomb interaction terms are written as  $V \begin{pmatrix} e_T & e_B \\ h_T & h_B \end{pmatrix}$ , which explicitly identifies the number of charge carriers in each QD for the resulting Coulomb interaction energy.  $E_{X^{n\pm}}^D$  ( $E_{X^{n\pm}}^I$ ) denote the fundamental direct (indirect) exciton energies when the electron and hole are in the same (different) dot at the anticrossing field. In other words,  $\begin{pmatrix} 0 & \underline{1} \\ 1 & \underline{1} \end{pmatrix}$  is the same as  $E_{X_h^0}^D$ .

## 5.5 Spectroscopic Signatures and Hamiltonians

### 5.5.1 Anticrossing formation

One of the characteristic spectroscopic signatures of VQDMs is the formation of anti-crossings of PL spectral lines, as shown in Figure 5.3. For a neutral exciton, as shown in Fig 5.3, when the electron and hole undergoing recombination are from the same QD, we see a nearly the horizontal spectral line, i.e. with energy largely independent of applied electric field. This transition is also known as a direct

transition and the charge complex as the direct exciton. The diagonal “indirect” spectral lines with a strong dependence of energy on applied electric field are seen when electron and hole are in separate dots. The dependence of state energy on applied bias is described by the Stark energy  $\Delta E_{Stark} = edF$ , where  $ed$  is the excitonic dipole moment and  $d$  is the separation between the centers of the electron and hole wavefunctions. For a direct exciton the dipole moment is extremely small as the electron and hole are in the same QD. The resulting small shift is the well-known Quantum Confined Stark Effect of single QDs, with emission relatively flat as a function of applied field. On the other hand, for an indirect exciton, the separation between the electron and hole is determined predominantly by the separation distance between the two QDs, which results in a higher magnitude of exciton dipole moment. Thus emission from an indirect exciton is strongly tuned by an electric field and a steep diagonal emission line results<sup>50</sup>.

The energies of the direct and indirect transition are non-degenerate and separated by the Stark energy  $-edF$ , which depends on the applied electric field  $F$ . When the applied electric field is tuned such that these states are on resonance, i.e. degenerate, molecular orbitals are formed by the coherent tunneling of a charge particle, in this case a hole, between the quantum dots. The anticrossing depicted in figure 5.2 where the direct and indirect exciton lines would be expected to cross is the signature of this formation of molecular orbital states. The energies of the bonding and antibonding molecular orbital are  $E_D - t$  and  $E_D + t$  respectively, where  $E_D$  is the energy of the direct state. The magnitude of  $t$  can be measured from the difference of the energies of the molecular states<sup>19</sup>.

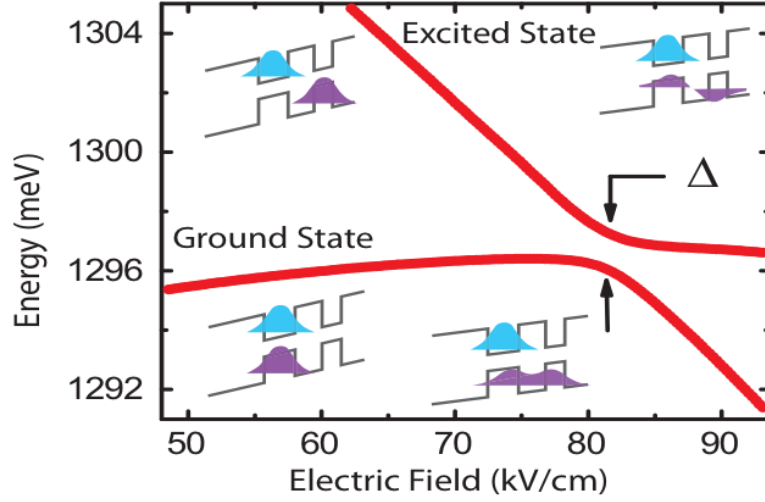


Figure 5.3: Formation of anti-crossing for a neutral exciton by tunneling of a single hole between dots in a VQDM under an applied electric field<sup>19</sup>

### 5.5.2 Hamiltonian for $X^0$ State

The neutral exciton represented in Figure 5.2 by green lines is formed by the recombination of single electron and hole in either the same dot or different dots. This state is often considered the gateway charge complex and forms at low excitation intensities of the laser. This charge complex is found when the intensity of laser is low enough to only excite only one electron hole pair and the applied electric field cannot overcome the inherent coulomb blockade of the single electron hole pair to tunnel any spectator charges into the QDM. The PL is modeled as the difference of the initial and the final states Hamiltonians. The Hamiltonian for the initial state with basis  $\begin{pmatrix} 0 & 1 \\ 0 & 1 \end{pmatrix}$

and  $\begin{pmatrix} 1 & 0 \\ 0 & 1 \end{pmatrix}$  is written as

$$H_{X^0}^i = \begin{bmatrix} E_{X^0}^D + V \begin{pmatrix} 0 & 1 \\ 0 & 1 \end{pmatrix} & -t_{X^0} \\ -t_{X^0} & E_{X^0}^I + V \begin{pmatrix} 1 & 0 \\ 0 & 1 \end{pmatrix} + ed(F - F_0) \end{bmatrix} \quad (5.2)$$

Here the  $t_{X^0}$  is the tunneling matrix element,  $F$  is the applied electric field and  $F_0$  is the electric field value at which the anticrossing for  $X^0$  is observed. For the neutral exciton, there are no charge carriers left after photon emission, hence we do not have a final state Hamiltonian. Thus, the energy of the PL is modeled by the Eigenvalues of equation 5.2, which are

$$E_{X^0} = \frac{1}{2} \left( E_{X^0}^D + V \begin{pmatrix} 0 & 1 \\ 0 & 1 \end{pmatrix} + E_{X^0}^I + V \begin{pmatrix} 1 & 0 \\ 0 & 1 \end{pmatrix} - ed(F - F_0) \right) \pm \frac{1}{2} \sqrt{(E_{X^0}^D + V \begin{pmatrix} 0 & 1 \\ 0 & 1 \end{pmatrix} - E_{X^0}^I - V \begin{pmatrix} 1 & 0 \\ 0 & 1 \end{pmatrix} + ed(F - F_0))^2 + 4(t_{X^0})^2} \quad (5.3)$$

All energies are referenced to the neutral exciton anti-crossing electric field and the Hamiltonian is constructed such that the states are degenerate in energy at  $F_0$ , therefore  $E_{X^0}^D$  can also be written as

$$E_{X^0}^D = E_{X^0}^I + V \begin{pmatrix} 1 & 0 \\ 0 & 1 \end{pmatrix} - V \begin{pmatrix} 0 & 1 \\ 0 & 1 \end{pmatrix} \quad (5.4)$$

### 5.5.3 Hamiltonian for the $X_{h^+}^0$ state

The neutral exciton with a dynamically trapped hole is a charge configuration seen for the particular VQDM studied here due to the barrier design with AlGaAs, which suppresses the relaxation of the hole to the top QD. This charge configuration with a single extra hole can be created when an optically-generated electron hole pair relaxes into the bottom dot, and then the electron tunnels out, leaving behind the hole. The AlGaAs hampers the tunneling of the hole into the top dot, effectively trapping it. Meanwhile, another electron hole pair is optically created in the top dot, resulting in emission from  $\begin{pmatrix} 0 & 1 \\ 1 & 1 \end{pmatrix}$ . The Hamiltonian for this state, using basis states  $\begin{pmatrix} 0 & 1 \\ 1 & 1 \end{pmatrix}$  and  $\begin{pmatrix} 1 & 0 \\ 1 & 1 \end{pmatrix}$ , is described as

$$H_{X_{h^+}^0}^i = \begin{bmatrix} E_{X^0}^D + V \begin{pmatrix} 0 & 1 \\ 1 & 1 \end{pmatrix} & -t_{X_{h^+}^0} \\ -t_{X_{h^+}^0} & E_{X^0}^I + V \begin{pmatrix} 1 & 0 \\ 1 & 1 \end{pmatrix} - ed(F - F_0) \end{bmatrix} \quad (5.5)$$

Here  $-t_{X_{h+}^0}$  is the tunneling coefficient for the neutral exciton with extra hole. The final state for this complex will only have a single trapped hole, and thus the final Hamiltonian doesn't contribute to the PL lines. The PL spectral lines from this state are modeled using the Eigenvalues of equation 5.5 and are

$$E_{X_{h+}^0} = \frac{1}{2} \left( E_{X^0}^D + V \begin{pmatrix} 0 & 1 \\ 1 & 1 \end{pmatrix} + E_{X^0}^I + V \begin{pmatrix} 1 & 0 \\ 1 & 1 \end{pmatrix} - ed(F - F_0) \right) \pm \frac{1}{2} \sqrt{(E_{X^0}^D + V \begin{pmatrix} 0 & 1 \\ 1 & 1 \end{pmatrix} - E_{X^0}^I - V \begin{pmatrix} 1 & 0 \\ 1 & 1 \end{pmatrix} + ed(F - F_0))^2 + 4(t_{X_{h+}^0})^2} \quad (5.6)$$

#### 5.5.4 Formation of X pattern

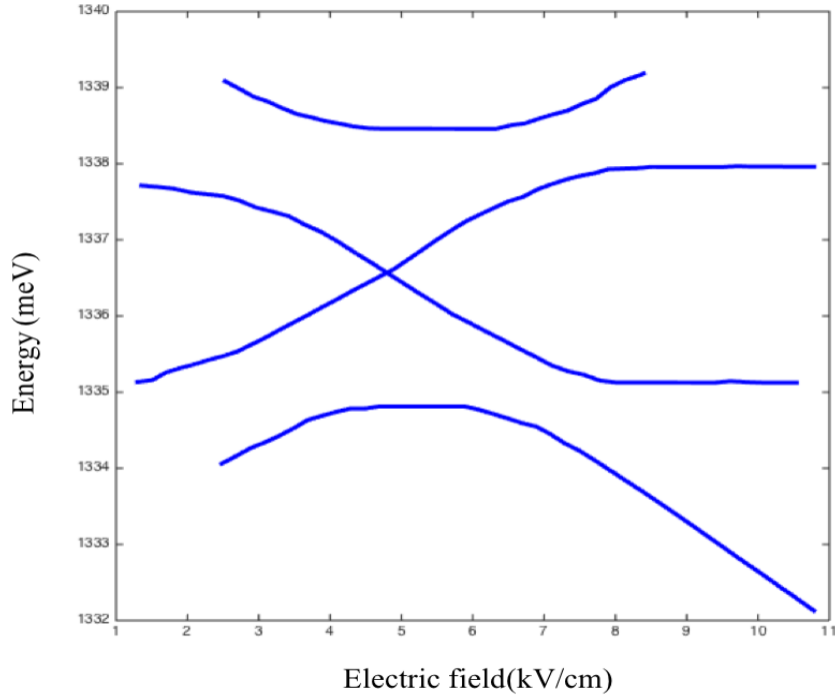


Figure 5.4: X pattern formation for the  $X^{2-}$  charge complex

A single anticrossing, as described above for the  $X^0$  state, is observed whenever coherent tunneling can arise in only the optically excited state. For complexes with more spectator charges, anticrossings can arise in both the optically excited and optical ground states. These anticrossings do not occur at the same value of applied electric field because the Coulomb interaction terms in the excited and ground states are different. As a result, the observed PL, which can be understood as the difference in energy between the excited and ground state Hamiltonians, has a characteristic “X” pattern. Figure 5.4 shows such an X pattern belonging to the charge complex  $X^{2-}$ . Four different anticrossings can be observed, two pairs at separate values of applied electric field. Each pair of anti-crossings originates from either the initial or the final state. We now turn to the Hamiltonians to explain the origin of the X pattern.

### 5.5.5 Hamiltonian for $X^{2-}$ state

The doubly charged negative trion state PL lines are the blue lines shown in Fig 1(b). The PL lines are modeled on the difference of Eigenvalues for the initial state ( $X^{2-}$ , 3 electrons and 1 hole in QDM) and final state ( $e^{2-}$ , 2 electrons left in QDM after recombination). This charge configuration is seen at higher applied electric fields where the ground state of the QDM is degenerate or below the Fermi level of the doped substrate, which results in the tunneling of extra electrons into the QDM. The presence of extra electrons leads to different Coulomb and spin interactions. The basis for the initial state Hamiltonian are  $\begin{pmatrix} 1 & 2 \\ 0 & 1 \end{pmatrix}$  and  $\begin{pmatrix} 2 & 1 \\ 0 & 1 \end{pmatrix}$  and the Hamiltonian is

$$H_{X^{2-}}^i = \begin{bmatrix} E_{X^0}^D + V \begin{pmatrix} 1 & 2 \\ 0 & 1 \end{pmatrix} - ed(F - F_0) & -t_{X^{2-}} \\ -t_{X^{2-}} & E_{X^0}^I + V \begin{pmatrix} 2 & 1 \\ 0 & 1 \end{pmatrix} - 2ed(F - F_0) \end{bmatrix} \quad (5.7)$$

The basis for the final state are  $\begin{pmatrix} 1 & 1 \\ 0 & 0 \end{pmatrix}$  and  $\begin{pmatrix} 2 & 1 \\ 0 & 0 \end{pmatrix}$  and the Hamiltonian is written as

$$H_{X^{2-}}^f = \begin{bmatrix} V \begin{pmatrix} 1 & 1 \\ 0 & 0 \end{pmatrix} - ed(F - F_0) & -t_{e^{2-}} \\ -t_{e^{2-}} & -E_{X^0}^D + E_{X^0}^I + V \begin{pmatrix} 2 & 0 \\ 0 & 0 \end{pmatrix} - 2ed(F - F_0) \end{bmatrix} \quad (5.8)$$

Here  $t_{X^{2-}}$  and  $t_{e^{2-}}$  are the tunneling matrix elements for  $X^{2-}$  and  $e^{2-}$  states, respectively. These Hamiltonians only describe the states that are seen in the PL map of Figure 5.2, which does not exhibit any triplet states. For this reason, interactions between different spin states aren't included in the Hamiltonian of Equation 5.7 and Equation 5.8. One can see that the different Coulomb interactions in the initial and final state Hamiltonians cause the direct and indirect optical transitions to be degenerate at different values of the applied electric field. As a result, there are two pairs of anticrossings observed, one corresponding to the degeneracy point in the initial state and one to the degeneracy point in the final state. This is the origin of the X pattern observed in Figure 5.4.

The analytical expressions for the 4 PL lines are generated from the difference between the Eigenvalues of the Hamiltonians. The Eigenvalues for the initial state's Hamiltonian are

$$E_{X^{2-}}^i = \frac{1}{2} \left( E_{X^0}^D + V \begin{pmatrix} 1 & 2 \\ 0 & 1 \end{pmatrix} + E_{X^0}^I + V \begin{pmatrix} 2 & 1 \\ 0 & 1 \end{pmatrix} - 3ed(F - F_0) \right) \pm \frac{1}{2} \sqrt{(E_{X^0}^D + V \begin{pmatrix} 1 & 2 \\ 0 & 1 \end{pmatrix} - E_{X^0}^I - V \begin{pmatrix} 2 & 1 \\ 0 & 1 \end{pmatrix} + ed(F - F_0))^2 + 4(t_{X^{2-}})^2} \quad (5.9)$$

Eigenvalues for the final Hamiltonian are written as

$$E_{X^{2-}}^f = \frac{1}{2} \left( -E_{X^0}^D + V \begin{pmatrix} 2 & 0 \\ 0 & 0 \end{pmatrix} + E_{X^0}^I + V \begin{pmatrix} 1 & 1 \\ 0 & 0 \end{pmatrix} - 3ed(F - F_0) \right) \pm \frac{1}{2} \sqrt{(E_{X^0}^D + V \begin{pmatrix} 1 & 1 \\ 0 & 0 \end{pmatrix} - E_{X^0}^I - V \begin{pmatrix} 2 & 0 \\ 0 & 0 \end{pmatrix} + ed(F - F_0))^2 + 4(t_{e^{2-}})^2} \quad (5.10)$$

### 5.5.6 Hamiltonian for $X_{h+}^{2-}$ state

The purple lines in the extracted PL map (Figure 5.2 (b)) describes the doubly negatively charged trion with an extra hole. This state can be thought of as an echo of the  $X^{2-}$  state with a small shift in energy due to the presence of the extra hole trapped in the bottom QD. The initial states's Hamiltonian is constructed using the basis of  $\begin{pmatrix} 1 & 2 \\ 1 & 1 \end{pmatrix}$  and  $\begin{pmatrix} 2 & 1 \\ 1 & 1 \end{pmatrix}$ . The Hamiltonian is as follows

$$H_{X_{h+}^{2-}}^i = \begin{bmatrix} E_{X^0}^D + V \begin{pmatrix} 1 & 2 \\ 1 & 1 \end{pmatrix} - ed(F - F_0) & -t_{X_{h+}^{2-}} \\ -t_{X_{h+}^{2-}} & E_{X^0}^I + V \begin{pmatrix} 2 & 1 \\ 1 & 1 \end{pmatrix} - 2ed(F - F_0) \end{bmatrix} \quad (5.11)$$

The final state's Hamiltonian is described as follows

$$H_{X_{h+}^{2-}}^f = \begin{bmatrix} V \begin{pmatrix} 1 & 1 \\ 1 & 0 \end{pmatrix} - ed(F - F_0) & -t_{e_{h+}^{2-}} \\ -t_{e_{h+}^{2-}} & -E_{X^0}^D + E_{X^0}^I + V \begin{pmatrix} 2 & 0 \\ 1 & 0 \end{pmatrix} - 2ed(F - F_0) \end{bmatrix} \quad (5.12)$$

With basis of  $\begin{pmatrix} 1 & 1 \\ 1 & 0 \end{pmatrix}$  and  $\begin{pmatrix} 2 & 0 \\ 1 & 0 \end{pmatrix}$ . The tunneling matrix elements for the  $X_{h+}^{2-}$  and  $e_{h+}^{2-}$  are  $-t_{X_{h+}^{2-}}$  and  $-t_{e_{h+}^{2-}}$  respectively. The Eigenvalues of the initial and final

Hamiltonians are

$$E_{X_{h+}^{2-}}^i = \frac{1}{2} \left( E_{X^0}^D + V \begin{pmatrix} 1 & 2 \\ 1 & 1 \end{pmatrix} + E_{X^0}^I + V \begin{pmatrix} 2 & 1 \\ 1 & 1 \end{pmatrix} - 3ed(F - F_0) \right) \pm \frac{1}{2} \sqrt{(E_{X^0}^D + V \begin{pmatrix} 1 & 2 \\ 1 & 1 \end{pmatrix} - E_{X^0}^I - V \begin{pmatrix} 2 & 1 \\ 1 & 1 \end{pmatrix} + ed(F - F_0))^2 + 4(t_{X_{h+}^{2-}})^2} \quad (5.13)$$

$$E_{X_{h+}^{2-}}^f = \frac{1}{2} \left( -E_{X^0}^D + V \begin{pmatrix} 2 & 0 \\ 1 & 0 \end{pmatrix} + E_{X^0}^I + V \begin{pmatrix} 1 & 1 \\ 1 & 0 \end{pmatrix} - 3ed(F - F_0) \right) \pm \frac{1}{2} \sqrt{(E_{X^0}^D + V \begin{pmatrix} 1 & 1 \\ 0 & 0 \end{pmatrix} - E_{X^0}^I - V \begin{pmatrix} 2 & 0 \\ 0 & 0 \end{pmatrix} + ed(F - F_0))^2 + 4(t_{e_{h+}^{2-}})^2} \quad (5.14)$$

The difference between these Eigenvalues gives analytical expressions for four spectral lines however in the PL map under study we see only 2 lines from this charge configuration and model on the visible lines.

## 5.6 Analytical expressions for observed spectral lines

Eigenvalues derived from the initial and final Hamiltonians for each of the charge configuration observed in the time integrated PL map in Fig 1 are used for generating the analytical expressions used to model PL lines. The expressions for PL lines for the neutral exciton and neutral exciton with a trapped hole are the Eigenvalues themselves. The expressions for the doubly charged trion and doubly charged trion with a trapped hole are the difference between the Eigenvalues of the initial and final states.

The analytical expressions for the spectral lines from the neutral exciton are as follows

$$y_{X^0}^1 = \frac{1}{2} \left( 2E_{X^0}^D + 2V \begin{pmatrix} 0 & 1 \\ 0 & 1 \end{pmatrix} + ed(F_0 - F) \right) + \frac{1}{2} \sqrt{(ed(F_0 - F))^2 + 4t_{X^0}^2} \quad (5.15)$$

$$y_{X^0}^2 = \frac{1}{2} \left( 2E_{X^0}^D + 2V \begin{pmatrix} 0 & 1 \\ 0 & 1 \end{pmatrix} + ed(F_0 - F) \right) - \frac{1}{2} \sqrt{(ed(F_0 - F))^2 + 4t_{X^0}^2} \quad (5.16)$$

Expressions for modelling neutral exciton with a trapped hole are

$$y_{X_{h+}^0}^3 = \frac{1}{2} \left( 2E_{X^0}^D + V \begin{pmatrix} 0 & 1 \\ 0 & 1 \end{pmatrix} - V \begin{pmatrix} 1 & 0 \\ 0 & 1 \end{pmatrix} + V \begin{pmatrix} 0 & 1 \\ 1 & 1 \end{pmatrix} + V \begin{pmatrix} 1 & 0 \\ 1 & 1 \end{pmatrix} + ed(F_0 - F) \right) + \frac{1}{2} \sqrt{(V \begin{pmatrix} 0 & 1 \\ 0 & 1 \end{pmatrix} - V \begin{pmatrix} 1 & 0 \\ 0 & 1 \end{pmatrix} - V \begin{pmatrix} 0 & 1 \\ 1 & 1 \end{pmatrix} + V \begin{pmatrix} 1 & 0 \\ 1 & 1 \end{pmatrix} + ed(F_0 - F))^2 + 4t_{X_{h+}^0}^2} \quad (5.17)$$

$$y_{X_{h^+}^0}^4 = \frac{1}{2} \left( 2E_{X^0}^D + V \begin{pmatrix} 0 & 1 \\ 0 & 1 \end{pmatrix} - V \begin{pmatrix} 1 & 0 \\ 0 & 1 \end{pmatrix} + V \begin{pmatrix} 0 & 1 \\ 1 & 1 \end{pmatrix} + V \begin{pmatrix} 1 & 0 \\ 1 & 1 \end{pmatrix} + ed(F_0 - F) \right) - \frac{1}{2} \sqrt{(V \begin{pmatrix} 0 & 1 \\ 0 & 1 \end{pmatrix} - V \begin{pmatrix} 1 & 0 \\ 0 & 1 \end{pmatrix} - V \begin{pmatrix} 0 & 1 \\ 1 & 1 \end{pmatrix} + V \begin{pmatrix} 1 & 0 \\ 1 & 1 \end{pmatrix} + ed(F_0 - F))^2 + 4t_{X_{h^+}^0}{}^2} \quad (5.18)$$

We have four expressions for modeling spectral lines arising from the doubly negatively charged trion configuration

$$y_{X^{2-}}^5 = \frac{1}{2} \left( 2E_{X^0}^D + V \begin{pmatrix} 1 & 2 \\ 0 & 1 \end{pmatrix} + V \begin{pmatrix} 2 & 1 \\ 0 & 1 \end{pmatrix} - V \begin{pmatrix} 1 & 1 \\ 0 & 0 \end{pmatrix} - V \begin{pmatrix} 2 & 0 \\ 0 & 0 \end{pmatrix} \right) - \frac{1}{2} \sqrt{\left( V \begin{pmatrix} 0 & 1 \\ 0 & 1 \end{pmatrix} - V \begin{pmatrix} 1 & 0 \\ 0 & 1 \end{pmatrix} + V \begin{pmatrix} 2 & 1 \\ 0 & 1 \end{pmatrix} - V \begin{pmatrix} 1 & 2 \\ 0 & 1 \end{pmatrix} + ed(F_0 - F) \right)^2 + 4t_{X^{2-}}{}^2} + \frac{1}{2} \sqrt{\left( V \begin{pmatrix} 0 & 1 \\ 0 & 1 \end{pmatrix} - V \begin{pmatrix} 1 & 0 \\ 0 & 1 \end{pmatrix} - V \begin{pmatrix} 1 & 1 \\ 0 & 0 \end{pmatrix} + V \begin{pmatrix} 2 & 0 \\ 0 & 0 \end{pmatrix} + ed(F_0 - F) \right)^2 + 4t_{e^{2-}}{}^2} \quad (5.19)$$

$$y_{X^{2-}}^6 = \frac{1}{2} \left( 2E_{X^0}^D + V \begin{pmatrix} 1 & 2 \\ 0 & 1 \end{pmatrix} + V \begin{pmatrix} 2 & 1 \\ 0 & 1 \end{pmatrix} - V \begin{pmatrix} 1 & 1 \\ 0 & 0 \end{pmatrix} - V \begin{pmatrix} 2 & 0 \\ 0 & 0 \end{pmatrix} \right) - \frac{1}{2} \sqrt{\left( V \begin{pmatrix} 0 & 1 \\ 0 & 1 \end{pmatrix} - V \begin{pmatrix} 1 & 0 \\ 0 & 1 \end{pmatrix} + V \begin{pmatrix} 2 & 1 \\ 0 & 1 \end{pmatrix} - V \begin{pmatrix} 1 & 2 \\ 0 & 1 \end{pmatrix} + ed(F_0 - F) \right)^2 + 4t_{X^{2-}}{}^2} - \frac{1}{2} \sqrt{\left( V \begin{pmatrix} 0 & 1 \\ 0 & 1 \end{pmatrix} - V \begin{pmatrix} 1 & 0 \\ 0 & 1 \end{pmatrix} - V \begin{pmatrix} 1 & 1 \\ 0 & 0 \end{pmatrix} + V \begin{pmatrix} 2 & 0 \\ 0 & 0 \end{pmatrix} + ed(F_0 - F) \right)^2 + 4t_{e^{2-}}{}^2} \quad (5.20)$$

$$y_{X^{2-}}^7 = \frac{1}{2} \left( 2E_{X^0}^D + V \begin{pmatrix} 1 & 2 \\ 0 & 1 \end{pmatrix} + V \begin{pmatrix} 2 & 1 \\ 0 & 1 \end{pmatrix} - V \begin{pmatrix} 1 & 1 \\ 0 & 0 \end{pmatrix} - V \begin{pmatrix} 2 & 0 \\ 0 & 0 \end{pmatrix} \right) + \frac{1}{2} \sqrt{\left( V \begin{pmatrix} 0 & 1 \\ 0 & 1 \end{pmatrix} - V \begin{pmatrix} 1 & 0 \\ 0 & 1 \end{pmatrix} + V \begin{pmatrix} 2 & 1 \\ 0 & 1 \end{pmatrix} - V \begin{pmatrix} 1 & 2 \\ 0 & 1 \end{pmatrix} + ed(F_0 - F) \right)^2 + 4t_{X^{2-}}{}^2} + \frac{1}{2} \sqrt{\left( V \begin{pmatrix} 0 & 1 \\ 0 & 1 \end{pmatrix} - V \begin{pmatrix} 1 & 0 \\ 0 & 1 \end{pmatrix} - V \begin{pmatrix} 1 & 1 \\ 0 & 0 \end{pmatrix} + V \begin{pmatrix} 2 & 0 \\ 0 & 0 \end{pmatrix} + ed(F_0 - F) \right)^2 + 4t_{e^{2-}}{}^2} \quad (5.21)$$

$$\begin{aligned}
y_{X^{2-}}^8 &= \frac{1}{2} \left( 2E_{X^0}^D + V \begin{pmatrix} 1 & 2 \\ 0 & 1 \end{pmatrix} + V \begin{pmatrix} 2 & 1 \\ 0 & 1 \end{pmatrix} - V \begin{pmatrix} 1 & 1 \\ 0 & 0 \end{pmatrix} - V \begin{pmatrix} 2 & 0 \\ 0 & 0 \end{pmatrix} \right) + \\
&\frac{1}{2} \sqrt{\left( V \begin{pmatrix} 0 & 1 \\ 0 & 1 \end{pmatrix} - V \begin{pmatrix} 1 & 0 \\ 0 & 1 \end{pmatrix} + V \begin{pmatrix} 2 & 1 \\ 0 & 1 \end{pmatrix} - V \begin{pmatrix} 1 & 2 \\ 0 & 1 \end{pmatrix} + ed(F_0 - F) \right)^2 + 4t_{X^{2-}}^2 -} \\
&\frac{1}{2} \sqrt{\left( V \begin{pmatrix} 0 & 1 \\ 0 & 1 \end{pmatrix} - V \begin{pmatrix} 1 & 0 \\ 0 & 1 \end{pmatrix} - V \begin{pmatrix} 1 & 1 \\ 0 & 0 \end{pmatrix} + V \begin{pmatrix} 2 & 0 \\ 0 & 0 \end{pmatrix} + ed(F_0 - F) \right)^2 + 4t_{e^{2-}}^2} \quad (5.22)
\end{aligned}$$

Theoretically we compute four expressions for the  $X_{h^+}^{2-}$  state however for the VQDMS studied here we only observe two spectral lines. We plotted all four lines and matched the analytical expressions to the visible lines. The observed spectral lines are modeled by the following expressions

$$\begin{aligned}
y_{X_{h^+}^{2-}}^9 &= \frac{1}{2} \left( 2E_{X^0}^D + V \begin{pmatrix} 1 & 2 \\ 1 & 1 \end{pmatrix} + V \begin{pmatrix} 2 & 1 \\ 1 & 1 \end{pmatrix} - V \begin{pmatrix} 1 & 1 \\ 1 & 0 \end{pmatrix} - V \begin{pmatrix} 2 & 0 \\ 1 & 0 \end{pmatrix} \right) + \\
&\frac{1}{2} \sqrt{\left( V \begin{pmatrix} 0 & 1 \\ 0 & 1 \end{pmatrix} - V \begin{pmatrix} 1 & 0 \\ 0 & 1 \end{pmatrix} + V \begin{pmatrix} 2 & 1 \\ 1 & 1 \end{pmatrix} - V \begin{pmatrix} 1 & 2 \\ 1 & 1 \end{pmatrix} + ed(F_0 - F) \right)^2 + 4t_{X_{h^+}^{2-}}^2 +} \\
&\frac{1}{2} \sqrt{\left( V \begin{pmatrix} 0 & 1 \\ 0 & 1 \end{pmatrix} - V \begin{pmatrix} 1 & 0 \\ 0 & 1 \end{pmatrix} - V \begin{pmatrix} 1 & 1 \\ 1 & 0 \end{pmatrix} + V \begin{pmatrix} 2 & 0 \\ 1 & 0 \end{pmatrix} + ed(F_0 - F) \right)^2 + 4t_{e_{h^+}^{2-}}^2} \quad (5.23)
\end{aligned}$$

$$\begin{aligned}
y_{X_{h^+}^{2-}}^{10} &= \frac{1}{2} \left( 2E_{X^0}^D + V \begin{pmatrix} 1 & 2 \\ 1 & 1 \end{pmatrix} + V \begin{pmatrix} 2 & 1 \\ 1 & 1 \end{pmatrix} - V \begin{pmatrix} 1 & 1 \\ 1 & 0 \end{pmatrix} - V \begin{pmatrix} 2 & 0 \\ 1 & 0 \end{pmatrix} \right) + \\
&\frac{1}{2} \sqrt{\left( V \begin{pmatrix} 0 & 1 \\ 0 & 1 \end{pmatrix} - V \begin{pmatrix} 1 & 0 \\ 0 & 1 \end{pmatrix} + V \begin{pmatrix} 2 & 1 \\ 1 & 1 \end{pmatrix} - V \begin{pmatrix} 1 & 2 \\ 1 & 1 \end{pmatrix} + ed(F_0 - F) \right)^2 + 4t_{X_{h^+}^{2-}}^2 -} \\
&\frac{1}{2} \sqrt{\left( V \begin{pmatrix} 0 & 1 \\ 0 & 1 \end{pmatrix} - V \begin{pmatrix} 1 & 0 \\ 0 & 1 \end{pmatrix} - V \begin{pmatrix} 1 & 1 \\ 1 & 0 \end{pmatrix} + V \begin{pmatrix} 2 & 0 \\ 1 & 0 \end{pmatrix} + ed(F_0 - F) \right)^2 + 4t_{e_{h^+}^{2-}}^2} \quad (5.24)
\end{aligned}$$

These expressions are used for calculate physical parameter values from extracted PL data.

## 5.7 Importance of physical parameters for device development

Quantum optical devices would ideally have an array of optically-active two-level systems strongly coupled by a network of photonic waveguides and cavities. One would ideally like to be able to coherently manipulate the state of the two-level system using only optical pulses. Many, but not all, of these capabilities have been demonstrated in single QDs<sup>51,52</sup>. QDMs offer a number of unique features, such as indirect excitons and hole spin mixing, that make them especially promising for a scalable device paradigm<sup>53</sup>. For example, orthogonal hole spin projections that are energetically separated in the optical ground state could provide the logical basis states. Optical pulses could create coherent superpositions of these states if the pulses are applied at an applied electric field value in which the optically-excited states are coherently coupled [e.g. Figure 5.4]. As can be seen from the above Hamiltonians [e.g. Equation 5.7 and Equation 5.8] the precise electric field values at which such coherent coupling occurs depends on the precise value of Coulomb interaction terms. Designing scalable and robust architectures for quantum optical devices therefore requires a detailed understanding of the origin and magnitude of such Coulomb interaction terms, their variation from nanostructure to nanostructure, and the ways in which material composition and structure influence the magnitude of these terms. The present method for deriving the values for these terms is described in the following section.

## 5.8 Traditional Data Extraction

The traditional data extraction method starts with manually picking points of highest intensity at the specific field values from Fig 5.2(a) and generating the PL map

as shown in Fig 5.2(b). The extracted spectral lines are modeled using the analytical expression listed in the previous section. Let's take the example of one of the lines of the neutral exciton with a trapped hole, for which the analytical expression is given by Eigenvalue which is

$$y_{x^0}^2 = \frac{1}{2} \left( 2E_{x^0}^D + 2V \begin{pmatrix} 0 & 1 \\ 0 & 1 \end{pmatrix} + ed(F_0 - F) \right) - \frac{1}{2} \sqrt{(ed(F_0 - F))^2 + 4t_{x^0}^2} \quad (5.25)$$

Of the 7 parameters in this expression, only 2 parameters,  $t_{x^0}$  and  $edF$ , can be extracted directly from the raw PL data. The tunneling coefficients are the rate of tunneling of charge particles between the quantum dots and are extracted from the anti-crossing gap  $\Delta E = 2t$ <sup>54</sup>.  $F$  is the applied bias,  $e$  is fundamental charge and  $d$  is the center to center distance between the two quantum dots. Using these values, we calculate  $edF$ . These experimentally extracted values are inherently dependent on the precision of the data extraction process for tunneling coefficients and the distance between QDs, both of which are riddled with imprecision.

The next step is plotting the line with the best estimate values for all the other parameters. Let's start with fitting the  $E_{x^0}^D + V \begin{pmatrix} 0 & 1 \\ 0 & 1 \end{pmatrix}$  term for the best fit to the data.

Changing its value from 1338 meV to 1337.85 meV gives the fits shown in Figure 5.5.

We then choose the value that looks to be the best fit to the data and start estimating other parameters. The other 4 parameters are variables that are used as fit parameters and their values are manually tweaked until a particular set is best fit to the traditionally processed experimental data. This final set of parameters for each line is considered the best fit values for the fundamental parameters and added to the knowledge repository to be used in the future to grow and study nanostructures. One could use a chi-squared optimization, but with 5 fit parameters for each individual

expression, it is not clear that the obtained values would necessarily have physical meaning, nor would we have any knowledge of our confidence in each value.

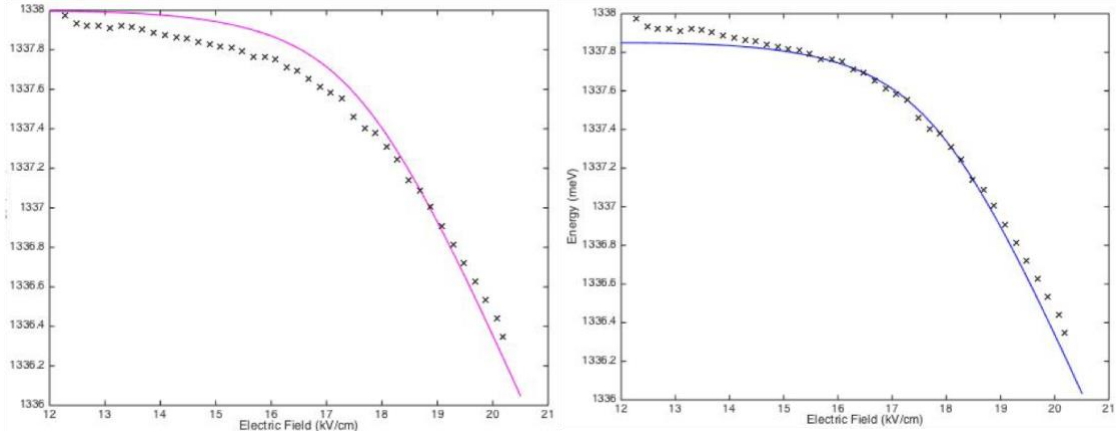


Figure 5.5: Manual iterative fits for the neutral exciton line by varying the term  $E_{X_0}^D + V \begin{pmatrix} 0 & 1 \\ 0 & 1 \end{pmatrix}$  from 1338 meV to 1337.85 meV.

## 5.9 Limitations of the traditional data extraction

The conventional approach for extracting fundamental physical parameters is described in the previous section. At the end of the analysis, we have a set of values that are generated through manual iterative fits to partial data. Conventionally fitting methods have significant limitations.

1. Iterative manual fitting does not guarantee a global fit. The analytical expression for each charge complex is manually fit only to individual charge complexes and not to all the states simultaneously. This approach increases the probability of the charge specific values being local best fits and not global fits.
2. Inability to assess the confidence of the estimated values. No statistical analysis is done post evaluation to the value sets. Visual best fit decisions are

made by the data analyzer with no quantifiable fit analysis. As shown in Fig 5.5, both fits are visually just as good. Thus, such fit values cannot be used as benchmarks to design devices.

3. Use of only a partial data set. The first step of traditional data extraction is picking points with the highest intensity to form the extracted PL map. This PL map is the skeleton for modeling the analytical expression, propagating the inaccuracy to the next steps. Information related to the confidence of our fit, like the resolution of our measuring tool or spectral wandering are not accounted for in the fitting process.

These limitations reveal two requirements. One, a comprehensive data extraction technique must include information crucial to the confidence of the final fits. Second, we need a statistically valid data analysis tool robust enough to be implemented on the sparse data sets associated with studies of novel nanostructured materials.

In the following chapters we demonstrate and adapted MCMC approach which overcomes all of these limitations.

## Chapter 6

### MARKOV CHAIN MONTE CARLO INTEGRATION

Markov chain Monte Carlo integration (MCMC) simulations have provided a framework for realistic statistical modeling for complex problems. Originating in statistical physics, MCMC in the past decade has found many applications in fields ranging from predicting conditions of railway bridge elements<sup>55</sup> to estimating the probability of developing AIDs after exposure to HIV<sup>56</sup> and computer vision<sup>57</sup>. We use the MCMC technique because it allows us to calculate an expectation value for a model parameter with fairly high accuracy without complete knowledge of all the other parameters.

#### 6.1 Bayesian Inference

MCMC implements the principles of Bayesian inference. Bayesian inference is a data analysis tool which uses Bayes' theorem to deduce statistical properties like the mean and the variance of the underlying probability distribution. Bayesian inference is a powerful tool for modelling of complex systems to extract predictive information from both sparse and dense data sets.

In Bayesian statistics, both observables and parameters are statistically random quantities. Establishing an inference requires building a joint probability distribution over all random quantities. Let  $D$  denote the observed data, and  $\theta$  denote model parameters and missing data. The joint probability distribution  $P(D, \theta)$  comprises two parts

$$P(D, \theta) = P(D|\theta)P(\theta) \quad (6.1)$$

where  $P(D|\theta)$  is the likelihood or conditional probability and  $P(\theta)$  is the prior distribution. The conditional probability,  $P(D|\theta)$ , is the probability of occurrence of observed data  $D$  given that  $\theta$  exists. The prior probability distribution represents all the known information about  $\theta$ . Specifying the likelihood and the prior distribution builds a full probability model. Since we possess the observed data  $D$ , we can determine the distribution of all the model parameters and missing data  $\theta$  by using Bayes theorem as follows:

$$P(\theta|D) = \frac{P(\theta)P(D|\theta)}{\int P(\theta)P(D|\theta)d\theta} \quad (6.2)$$

$P(\theta|D)$  is called the posterior distribution of  $\theta$  and any of its feature can be used for the Bayesian inference<sup>58</sup>. If prior distribution is not well-characterized, we must take care to select non-informative priors, meaning  $P(\theta)$  is sufficiently broad that it does not affect our estimate of the posterior<sup>59</sup>.

Bayes theorem can be applied to all location and scale parameters such as mean, expectation, variance and standard deviation. The expectation value of a function is a particularly useful value to calculate. The expectation of a variable can be defined as the average value acquired by a variable. The posterior expectation of a function  $M(\phi)$ , when we know the observed data  $N$ , can be calculated as

$$E[M(\phi)|N] = \frac{\int M(\phi)P(\phi)P(N|\phi)d\phi}{\int P(\phi)P(N|\phi)d\phi} \quad (6.3)$$

For higher dimension models, the integrations in this expression are difficult to calculate. For such high dimensional calculations, i.e. large number of variables, analytical approximation techniques like Laplace approximation and Monte Carlo integration are used.

## 6.2 Markov chain Monte Carlo

The principle idea behind MCMC for predictive analysis is building a proper posterior distribution for a parameter by calculating its expectation value. A posterior distribution is the parameter distribution generated after running a statistical simulation, MCMC in this case, on the prior distribution or known distribution of the parameter. This expectation value is calculated using Monte Carlo integration for samples drawn from Markov chains. In other words, building a probability distribution function for a parameter by using its sampled average. The sample average is generated by sampling each state of the Markov chain.

### 6.2.1 Monte Carlo integration

Monte Carlo integration is a random sampling technique used for approximate evaluation of parameters. This numerical estimation technique is used extensively for calculating complex integrals (like those in Bayes theorem). It first gained prominence in the late 1940s for use in simulations in the Manhattan project<sup>60</sup>.

Here we demonstrate implementation of Monte Carlo integration to calculate an expectation for  $M(X)$  where  $X$  is a vector of  $k$  random variables and with distribution  $\omega(\cdot)$ . The expectation can be simply written as

$$E[f(X)] = \frac{\int M(x)\omega(x)dx}{\int \omega(x)dx} \quad (6.4)$$

Monte Carlo integration allows us to write the same expectation by approximating to the mean of the samples  $\{X_t, t = 1, \dots, n\}$  drawn from the distribution  $\{\omega(\cdot)\}$  which is written as:

$$E[M(X)] \approx \frac{1}{n} \sum_{t=1}^n M(X_t) \quad (6.5)$$

The laws of large numbers ensure that this holds true when samples of  $\{X_t\}$  are drawn throughout the subset of all possible values of  $\omega(\cdot)$ . The accuracy of the estimate is independent of the dimension of the integral and dependent only on the number of samples taken. Increasing the number of samples increases the accuracy of the estimated value because the error is proportional to  $n^{-\frac{1}{2}}$ .

### 6.2.2 Markov Chain

Drawing a large number of samples can be done by any process. One way of doing this is by building a Markov chain with a stationary distribution (independent of time and starting point). We generate a Markov chain  $\{X_0, X_1, \dots\}$ , such that at each time  $t \geq 0$ , the next sample is from the transition kernel  $P(X_{t+1}|X_t)$  which only depends on the current state of the chain. After multiple draws, the generated chain will forget its initial states and the transition kernel converges to an invariant distribution. The main goal is to build a chain with stationary distribution which matches as closely as possible the distribution of interest  $\omega(\cdot)$ . After a period of burn in, where all the draws are invariant, we use the outcome of the Markov chain to estimate, using Monte Carlo integration, the expectation of  $M(X)$  given by the estimator

$$\bar{M} = \frac{1}{n-l} \sum_{i=l+1}^n M(X_i) \quad (6.6)$$

For this calculation, the first  $l$  values which are the burn in values are not considered. The convergence of the estimator to the required expectation is ensured by the ergodic theorem which states that the time average is equal to the space average for this measure preserving transform. This process of using outputs of a Markov chain as the samples for Monte Carlo integration to estimate the expectation of a variable is called Markov chain Monte Carlo.

### 6.2.3 Conventional MCMC

The traditional MCMC method is implemented using a Metropolis-Hastings (MH) algorithm. The driving principle behind MH – MCMC is to construct the chain by drawing samples from full probability distributions and independent prior distributions, which will match the distribution of interest. The first step is sampling a nominee point  $A$  from the prior distribution. This sample is accepted depending on an acceptance probability. If the acceptance rule is met, the nominee point is the next sample of the Markov chain. The acceptance rule in MH MCMC is designed to maintain a detailed balance<sup>58</sup> between the following two main conditions. First, the sampler should search over all space. Second, the sampler should search for higher probabilities under the full joint distribution i.e. try sampling in regions where all dimensions within  $X$  have a probability together. Maintaining this balance ensures the resulting stationary distribution is the target distribution. The Hastings modification to the acceptance rule of the original Metropolis algorithm is the inclusion of a random candidate set, which ensures that the sampler isn't trapped in a local extremum.

For multivariate analysis, implementing MH-MCMC involves generating a new nominee for each iteration and calculating the acceptance probability for each variable. If the acceptance rule is satisfied by all the variables at the time, then this variable set is accepted and it becomes a part of the chain. If the acceptance rule isn't satisfied the chain does not move forward and the previous chain value is repeated and evaluated against the acceptance rule. This results in a significantly longer convergence time for MH-MCMC implementation, but does ensure adequate sampling for highly correlated pairs, i.e variables that are interdependent.

#### **6.2.4 MCMC using Gibbs sampling**

Gibbs sampling is a special case of the Metropolis Hastings algorithm. Most MCMC applications prefer Gibbs sampling over the MH algorithm because Gibbs sampling has a relatively shorter convergence time for higher dimensional models. For each sampling iteration, Gibbs sampling chooses a candidate sample from a conditional posterior distribution. For multivariate analysis, unlike MH, it samples only one candidate dimension at a time keeping all the other dimensions the same. If this multidimensional set satisfies the acceptance rule, the sampler changes the value of the next dimension sequentially and not simultaneously. When using Gibbs sampling, the starting values for each parameter don't have to be from the prior distribution and can be determined randomly because the initial starting values will not impact the outcome if a sufficient burn in length is used. Changing a single variable at a time reduces the convergence time, but for highly correlated distributions it may lead the sampler to generate inaccurate estimates of the posterior covariances.

To ensure efficient Gibbs sampling, the Markov chains should be run for a long time or correlated parameters should be blocked to ensure sufficient mixing of the chains. Blocking means grouping highly correlated parameters together to form a higher dimensional body that is updated at each sampling iteration instead of randomly changing only a single parameter. The easiest check to evaluate chain mixing is to run multiple chains from different starting points and see if they converge to similar outcomes.

## Chapter 7

### IMPLEMENTING MCMC ON QDM SPECTROSCOPY DATA

We developed and demonstrate the first of its kind application of MCMC to calculate the best-fit parameters for nanostructure optical spectroscopy data. We implemented and adapted MCMC on the PL for vertically stacked QDMs under applied electric fields as described in chapter 5.

The two-step approach demonstrated here overcomes all of the limitations of the traditional data analysis techniques for understanding spectroscopy data from nanostructured material as described in section 5.9. The first step is implementing a novel data extraction method that captures and utilizes all of the information generated in a raw, time integrated, spectral map. The second step is the implementation of a novel adaptation of MCMC simulation on the extracted spectroscopy data.

For implementing MCMC on extracted spectroscopy data, we first simulate the analytical expression for each of the spectral lines observed in the PL map with best estimates of values of the physical parameters. The next step is to compare the virtual spectral map to the processed PL map to check for a goodness of fit. Depending on the goodness of fit we either retain the initial guesses or discard them and iterate the process thousands of times. The end product of this complete simulation is a set of values that are then used as the starting point for the next simulation. This cycle continues till an acceptable magnitude for “goodness of fit” or likelihood is achieved. The following sections present the details for implementation of this process.

## 7.1 Data extraction procedure

As described in Chapter 5, conventional data extraction techniques include only selection of points with the highest intensity. Using a single data point gives only a point estimate with no statistical information about its repeatability. Instead of using only point estimates, we use all of the data at the particular value of applied electric field, thus overcoming this constraint of the traditional methods.

The Lorentzian data extraction we use is implemented in three steps, which we illustrate with reference to Figure 7.1. The first step is extracting the complete slice of information at a single value of electric field (i.e. figure 7.1(a) is the data extracted for the single electric field value represented by the green line in Fig 7.1(b)). In figure 7.1(a), we observe two peaks, centered on yellow and blue lines. These two peaks belong to two different spectral lines. We fit the curves to a Lorentzian to determine the center energy value and the full width half max (FWHM) of the curve<sup>62</sup>. The third step is using the standard deviation of the center energy value, which is derived from the FWHM value, as the confidence interval for each energy value. By using the standard deviation of the center value, we conserve the information about the resolution of our measuring tool (the resolution of our spectrometer and other effects such as spectral wandering).

Consider figure 7.2 in which each slice is extracted and fit to a Lorentzian curve. Slice 1 has a weak intensity, and as a consequence has a larger FWHM and hence a larger error associated with its center energy value. Slice 2 is significantly brighter and is fit with a Lorentzian that has a smaller error bar for the energy value.

Figure 7.3 shows the extracted data for the complete TIPL map for a single VQDM pair. Each energy value was extracted by fitting extracted electric field specific data slice to a Lorentzian to generate point specific error bars.

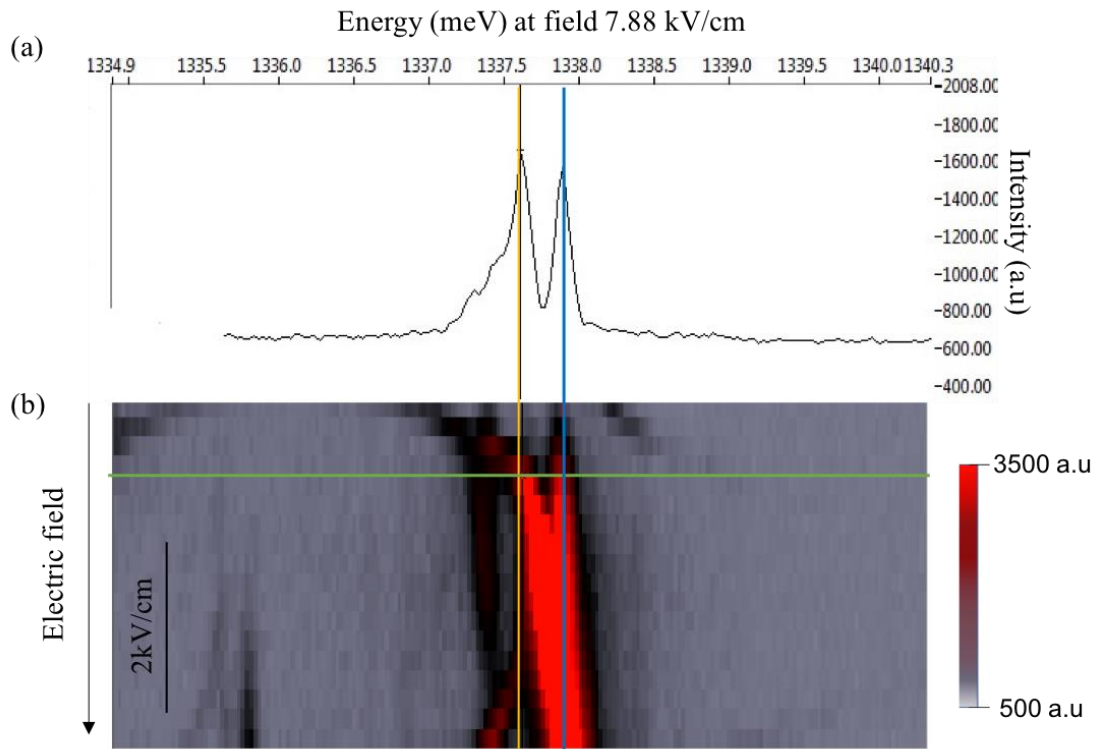


Figure 7.1: (a) Raw intensity plot extracted at 7.88kV/cm from TIPL data from a single VQDM under applied electric field (b) Section of the raw TIPL map extracted from TIPL data for a single VQDM under electric field being fit to the lorentzian

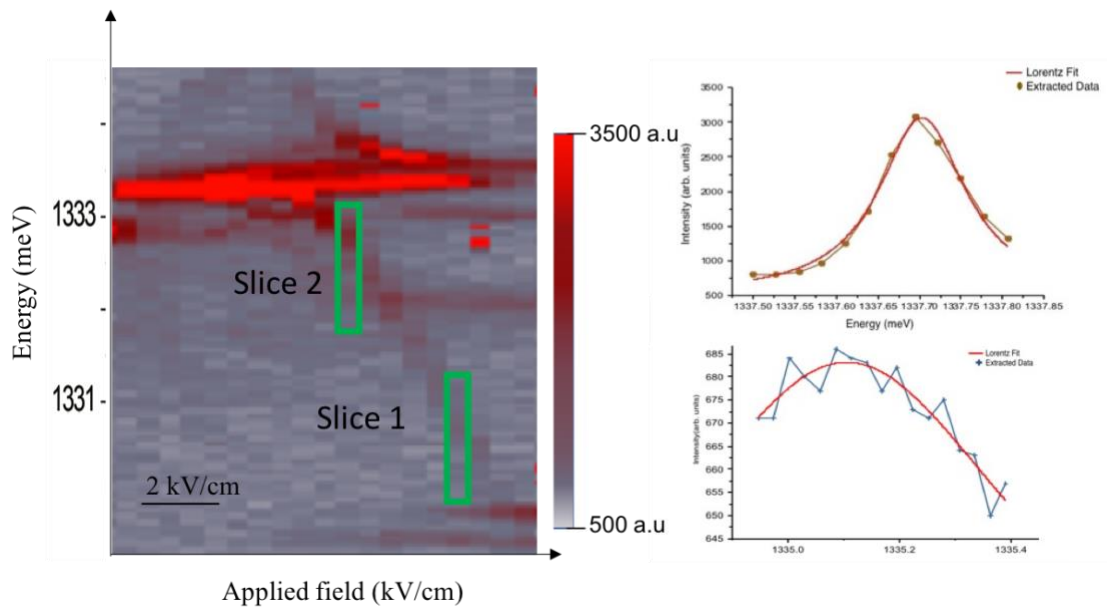


Figure 7.2: Lorentzian fit to raw PL data at two different field values for a single VQDM under applied electric field

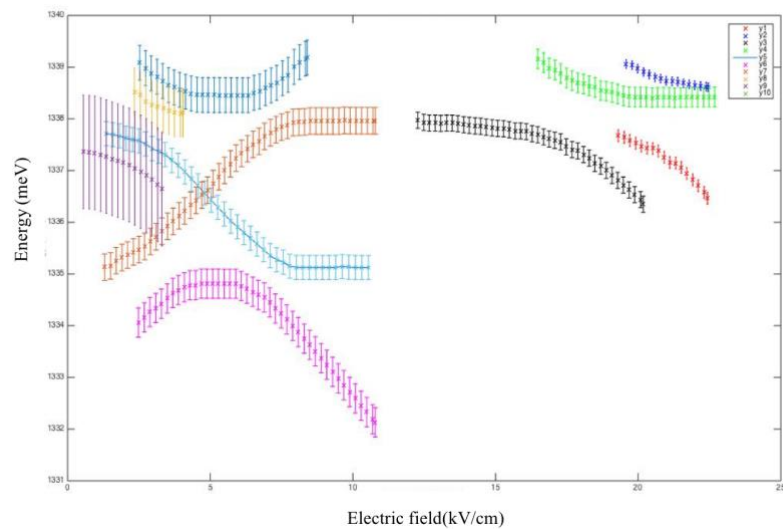


Figure 7.3: Processed TIPL map with extracted peak energy and error bars generated from the Lorentzian fits on extracted data from raw TIPL map for a single VQDM under applied electric field

If we attempt to use a manual fitting method to extract parameters from this data, we find that multiple parameter values could fit the data equally well. For example, in Figure 7.4 we show the black cross data points that are from the neutral exciton PL line that is described by the expression derived in section 5.5.

$$y_{x^0}^2 = \frac{1}{2} \left( 2E_{x^0}^D + 2V \begin{pmatrix} 0 & 1 \\ 0 & 1 \end{pmatrix} + ed(F_0 - F) \right) - \frac{1}{2} \sqrt{(ed(F_0 - F))^2 + 4t_{x^0}^2} \quad (7.1)$$

The pink and the blue fit lines shown in Figure 7.4 are generated by changing the  $E_{x^0}^D + V \begin{pmatrix} 0 & 1 \\ 0 & 1 \end{pmatrix}$ , from 1338 meV to 1337.85 meV. Both of these values fit the data within error bars, but without any statistical analysis we have no basis by which to choose one value over the other. The MCMC approach we develop here allows us to overcome this limitation of traditional fitting methods.

## 7.2 Implementing adapted MCMC

One of the crucial prerequisites for MCMC implementation is a robust theoretical model on which the simulation can be built. In our case, the analytical expressions that describe the PL of a VQDM are derived from well-established matrix Hamiltonians that have been validated in multiple experiments<sup>6,63,64</sup>. Second, the variables on which we run MCMC should be mathematically unique within the constructs of the theoretical model. The following sections will describe each step in the development of a MCMC method for fitting our experimental data. The approach is generalizable to analysis of any relatively sparse experimental data that can be described by a theoretical model that includes numerous parameters.

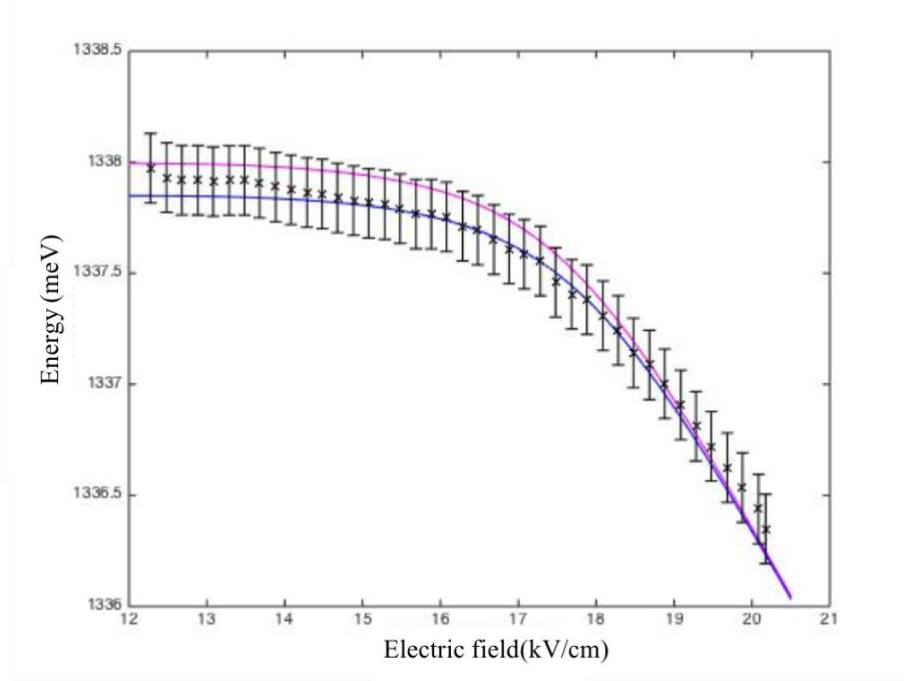


Figure 7.4: Manual fitting of parameter for neutral exciton line for a single VQDM under applied electric field using two values for  $E_{x^0}^D + V \begin{pmatrix} 0 & 1 \\ 0 & 1 \end{pmatrix}$ , pink (1338 meV) and blue (1337.85 meV). Each simulated line is within error bars.

### 7.2.1 Uniquely identifiable parameters

All of the spectral lines seen in the PL map of the QDM in figure 7.3 are described using analytical expressions that are generated from using the Eigen energies of the Hamiltonian for that charge state, as shown in section 5.5. Consider the example of the neutral exciton, described by the analytical expression in Equation 7.1. This expression has 7 independent physical parameters. When we consider all of the analytical expressions for a full set of 10 spectral lines, we find that there are 21 physical parameters that appear. Table 7.1 lists all the physical parameters.

Table 7.1: List of all physical parameters that describe the TIPL map of VQDMs

$E_{X^0}^D$	Energy Difference between s-like energy states for electrons and holes in top QD.
$E_{X^0}^I$	Energy difference between s-like electron in the bottom dot and hole in top QD.
$V \begin{pmatrix} 0 & 1 \\ 0 & 1 \end{pmatrix}$	Coulomb interaction term with an electron and hole both in the top QD.
$V \begin{pmatrix} 1 & 0 \\ 0 & 1 \end{pmatrix}$	Coulomb interaction term with an electron in the bottom QD and a hole in the top QD.
$V \begin{pmatrix} 0 & 1 \\ 1 & 1 \end{pmatrix}$	Coulomb interaction term with an electron in the top QDs and a hole in both the QDs.
$V \begin{pmatrix} 1 & 0 \\ 1 & 1 \end{pmatrix}$	Coulomb interaction term with an electron in the bottom QDs and a hole in both the QDs.
$V \begin{pmatrix} 1 & 2 \\ 0 & 1 \end{pmatrix}$	Coulomb interaction term with one electron in the bottom QD, two electrons in the top QD and a single hole in the top QD.
$V \begin{pmatrix} 2 & 1 \\ 0 & 1 \end{pmatrix}$	Coulomb interaction term with two electrons in the bottom QD, single electron in the top QD and a single hole in the top QD.
$V \begin{pmatrix} 1 & 1 \\ 0 & 0 \end{pmatrix}$	Coulomb interaction term with a single electron in the top and bottom dot.
$V \begin{pmatrix} 2 & 0 \\ 0 & 0 \end{pmatrix}$	Coulomb interaction term with two electrons in the bottom dot.
$V \begin{pmatrix} 1 & 2 \\ 1 & 1 \end{pmatrix}$	Coulomb interaction term with one electron in the bottom dot, two electrons in the top dot and one hole in each of the dots
$V \begin{pmatrix} 2 & 1 \\ 1 & 1 \end{pmatrix}$	Coulomb interaction term with one electron in the top dot, two electrons in the bottom dot and a hole in each of the dots.
$V \begin{pmatrix} 1 & 1 \\ 1 & 0 \end{pmatrix}$	Coulomb interaction term with one electron in each of the dots and a single hole in the bottom QD.
$V \begin{pmatrix} 2 & 0 \\ 1 & 0 \end{pmatrix}$	Coulomb interaction term with one hole and two electrons in the bottom QD.
$edF_0$	Electric field at which $X^0$ anti crossing occurs
$t_{X^0}$	Tunneling coefficient for $X^0$ state
$t_{X_h^0}$	Tunneling coefficient for $X_h^0$ state
$t_{X^{2-}}$	Tunneling coefficient for $X^{2-}$ state
$t_{e^{2-}}$	Tunneling coefficient for $e^{2-}$ state
$t_{X_h^{2-}}$	Tunneling coefficient for $X_h^{2-}$ state
$t_{e_h^{2-}}$	Tunneling coefficient for $e_h^{2-}$ state

Of these 21 physical parameter, 6 tunneling coefficients values (e.g.  $t_{X^0}$ ) appear independently, and  $E_{X^0}^D$  and  $E_{X^0}^I$  relationship is defined in Chapter 5. The remaining 14 physical parameters appear in analytical expressions as sums and differences which means that they are not uniquely identifiable. To find the number of uniquely identifiable parameters, we first find the number of degrees of freedom of our system. For our system, we find 10 linear combinations of the 14 parameters that are uniquely identifiable. We now explain how we identify the number and definition of these uniquely identifiable linear combinations.

We first rewrite the analytical expressions of the spectral lines into matrix form which is called the linear identifiable matrix. Each row of the matrix corresponds to a single analytical expression of every PL line seen. Each column of the matrix corresponds to the appearance of a single parameter in each equation, with the column specified in Table 7.1.

$$\begin{bmatrix} L1 \\ L2 \\ L3 \\ L4 \\ L5 \\ L6 \\ L7 \\ L8 \\ L9 \\ L10 \end{bmatrix} = \begin{bmatrix} 2 & 2 & 0 & 0 & 0 & 0 & 0 & 0 & 0 & 0 & 0 & 0 & 0 & 1 \\ 0 & 0 & 0 & 0 & 0 & 0 & 0 & 0 & 0 & 0 & 0 & 0 & 0 & 1 \\ 2 & 1 & -1 & 1 & 1 & 0 & 0 & 0 & 0 & 0 & 0 & 0 & 0 & 1 \\ 0 & 1 & -1 & -1 & 1 & 0 & 0 & 0 & 0 & 0 & 0 & 0 & 0 & 1 \\ 2 & 0 & 0 & 0 & 0 & 1 & 1 & -1 & -1 & 0 & 0 & 0 & 0 & 0 \\ 0 & 1 & -1 & 0 & 0 & -1 & 1 & 0 & 0 & 0 & 0 & 0 & 0 & 1 \\ 0 & 1 & -1 & 0 & 0 & 0 & 0 & -1 & 1 & 0 & 0 & 0 & 0 & 1 \\ 2 & 0 & 0 & 0 & 0 & 0 & 0 & 0 & 0 & 1 & 1 & -1 & -1 & 0 \\ 0 & 1 & -1 & 0 & 0 & 0 & 0 & 0 & 0 & -1 & 1 & 0 & 0 & 1 \\ 0 & 1 & -1 & 0 & 0 & 0 & 0 & 0 & 0 & 0 & 0 & -1 & 1 & 1 \end{bmatrix} \begin{bmatrix} E_{x_0}^D \\ V \begin{pmatrix} 0 & 1 \\ 0 & 1 \end{pmatrix} \\ V \begin{pmatrix} 1 & 0 \\ 0 & 1 \end{pmatrix} \\ V \begin{pmatrix} 0 & 1 \\ 1 & 1 \end{pmatrix} \\ V \begin{pmatrix} 1 & 0 \\ 1 & 1 \end{pmatrix} \\ V \begin{pmatrix} 1 & 2 \\ 0 & 1 \end{pmatrix} \\ V \begin{pmatrix} 2 & 1 \\ 0 & 1 \end{pmatrix} \\ V \begin{pmatrix} 1 & 1 \\ 0 & 0 \end{pmatrix} \\ V \begin{pmatrix} 2 & 0 \\ 0 & 0 \end{pmatrix} \\ V \begin{pmatrix} 1 & 2 \\ 1 & 1 \end{pmatrix} \\ V \begin{pmatrix} 2 & 1 \\ 1 & 1 \end{pmatrix} \\ V \begin{pmatrix} 1 & 1 \\ 1 & 0 \end{pmatrix} \\ V \begin{pmatrix} 2 & 0 \\ 1 & 0 \end{pmatrix} \\ edF_0 \end{bmatrix} \quad (7.2)$$

Matrix multiplication gives the L's, which could be used to rewrite the all of the analytical expressions. Instead, we first compute the observables (Ms) by using ranks of the transformation matrix, which is calculated by finding the orthonormal null space of the linear identifiable matrix. In other words, we first reduce the linear identifiable matrix to a simpler form. We generate the orthogonal matrix in Matlab

using the code in the appendix. This allows us to define the vector M in terms of the physical parameters as follows

$$\begin{bmatrix} M1 \\ M2 \\ M3 \\ M4 \\ M5 \\ M6 \\ M7 \\ M8 \\ M9 \\ M10 \end{bmatrix} = \begin{bmatrix} 1 & 1 & 0 & 0 & 0 & 0 & 0 & 0 & 0 & 0 & 0 & 0 & 0 \\ 1 & 0 & 0 & 1 & 0 & 0 & 0 & 0 & 0 & 0 & 0 & 0 & 0 \\ 0 & 0 & -1 & 0 & 1 & 0 & 0 & 0 & 0 & 0 & 0 & 0 & 0 \\ -1 & 0 & -1 & 0 & 0 & -1 & 1 & 0 & 0 & 0 & 0 & 0 & 0 \\ -1 & 0 & 0 & 0 & 0 & -1 & 0 & 1 & 0 & 0 & 0 & 0 & 0 \\ -2 & 0 & -1 & 0 & 0 & -1 & 0 & 0 & 1 & 0 & 0 & 0 & 0 \\ -1 & 0 & -1 & 0 & 0 & 0 & 0 & 0 & 0 & -1 & 1 & 0 & 0 \\ -1 & 0 & 0 & 0 & 0 & 0 & 0 & 0 & 0 & -1 & 0 & 1 & 0 \\ -2 & 0 & -1 & 0 & 0 & 0 & 0 & 0 & 0 & -1 & 0 & 0 & 1 \\ 0 & 0 & 0 & 0 & 0 & 0 & 0 & 0 & 0 & 0 & 0 & 0 & 1 \end{bmatrix} \begin{bmatrix} E_{x0}^D \\ V \begin{pmatrix} 0 & 1 \\ 0 & 1 \end{pmatrix} \\ V \begin{pmatrix} 1 & 0 \\ 0 & 1 \end{pmatrix} \\ V \begin{pmatrix} 0 & 1 \\ 1 & 1 \end{pmatrix} \\ V \begin{pmatrix} 1 & 0 \\ 1 & 1 \end{pmatrix} \\ V \begin{pmatrix} 1 & 2 \\ 0 & 1 \end{pmatrix} \\ V \begin{pmatrix} 2 & 1 \\ 0 & 1 \end{pmatrix} \\ V \begin{pmatrix} 1 & 1 \\ 0 & 0 \end{pmatrix} \\ V \begin{pmatrix} 2 & 0 \\ 0 & 0 \end{pmatrix} \\ V \begin{pmatrix} 1 & 2 \\ 1 & 1 \end{pmatrix} \\ V \begin{pmatrix} 2 & 1 \\ 1 & 1 \end{pmatrix} \\ V \begin{pmatrix} 1 & 1 \\ 1 & 0 \end{pmatrix} \\ V \begin{pmatrix} 2 & 0 \\ 1 & 0 \end{pmatrix} \\ edF_0 \end{bmatrix} \quad (7.3)$$

The relationship between L's and M's is described as follows

$$\begin{bmatrix} M1 \\ M2 \\ M3 \\ M4 \\ M5 \\ M6 \\ M7 \\ M8 \\ M9 \\ M10 \end{bmatrix} = \begin{bmatrix} 2 & 0 & 0 & 0 & 0 & 0 & 0 & 0 & 0 & 1 \\ 0 & 0 & 0 & 0 & 0 & 0 & 0 & 0 & 0 & 1 \\ 1 & 1 & 1 & 0 & 1 & 0 & 0 & 0 & 0 & 1 \\ 1 & -1 & 1 & 0 & 0 & 0 & 0 & 0 & 0 & 1 \\ 0 & 0 & 0 & 1 & -1 & -1 & 0 & 1 & 0 & 0 \\ 1 & 0 & 0 & 1 & 0 & 0 & 0 & 0 & 1 & 1 \\ 1 & 0 & 0 & 0 & -1 & 1 & 0 & 0 & 0 & 1 \\ 0 & 0 & 0 & 0 & 0 & 0 & 1 & -1 & -1 & 0 \\ 1 & 0 & 0 & 0 & 0 & 0 & 1 & 0 & 0 & 1 \\ 1 & 0 & 0 & 0 & 0 & 0 & 0 & -1 & 1 & 1 \end{bmatrix} \begin{bmatrix} L1 \\ L2 \\ L3 \\ L4 \\ L5 \\ L6 \\ L7 \\ L8 \\ L9 \\ L10 \end{bmatrix} \quad (7.4)$$

We next rewrite all then analytical expressions using the observables as defined in equation 7.3:

$$y_{X^0} = \frac{1}{2} \left\{ (2 * M1 + M10 - ed(X)) \pm \sqrt{(M10 - ed(X))^2 + 4t_{X^0}{}^2} \right\} \quad (7.5)$$

$$y_{X_{h+}^0} = \frac{1}{2} \left\{ (M1 + M2 + M3 + M10 - ed(X)) \pm \sqrt{(M1 - M2 + M3 + M10 - ed(X))^2 + 4t_{X_{h+}^0}{}^2} \right\} \quad (7.6)$$

$$y_{X^{2-}} = \frac{1}{2} \left\{ (M4 - M5 - M6) \pm \sqrt{(M1 + M4 + M10 - ed(X))^2 + 4t_{X^{2-}}{}^2} \pm \sqrt{(M1 - M5 + M6 + M10 - ed(X))^2 + 4t_{e^{2-}}{}^2} \right\} \quad (7.7)$$

$$y_{X_{h+}^{2-}} = \frac{1}{2} \left\{ (M7 - M8 - M9) + \sqrt{(M1 + M7 + M10 - ed(X))^2 + 4t_{X_{h+}^{2-}}{}^2} \pm \sqrt{(M1 - M8 + M9 + M10 - ed(X))^2 + 4t_{e_{h+}^{2-}}{}^2} \right\} \quad (7.8)$$

These transformed analytical expressions are then used as the theoretical model for our adapted MCMC simulation.

### 7.2.2 Initialization of MCMC

In principle, MCMC does not require good starting values for any parameter to simulate the theoretical model that describes the observed PL map. However, in practice, the burn in time can be reduced by good initial guesses for each of the parameters. A representative set of initial guesses used for the first simulation are as follows.

Table 7.2: List of initial values used for all observables and tunneling coefficients

M1	1337.90494486099	$E_{X^0}^D + V \begin{pmatrix} 0 & 1 \\ 0 & 1 \end{pmatrix}$
M2	1349.58433390299	$E_{X^0}^D + V \begin{pmatrix} 0 & 1 \\ 1 & 1 \end{pmatrix}$
M3	-13.4219046133749	$-V \begin{pmatrix} 1 & 0 \\ 0 & 1 \end{pmatrix} + V \begin{pmatrix} 1 & 0 \\ 1 & 1 \end{pmatrix}$
M4	-1350.31788317399	$-E_{X^0}^D - V \begin{pmatrix} 1 & 0 \\ 0 & 1 \end{pmatrix} - V \begin{pmatrix} 1 & 2 \\ 0 & 1 \end{pmatrix} + V \begin{pmatrix} 2 & 1 \\ 0 & 1 \end{pmatrix}$
M5	-1337.87276029558	$-E_{X^0}^D + V \begin{pmatrix} 1 & 1 \\ 0 & 0 \end{pmatrix} - V \begin{pmatrix} 1 & 2 \\ 0 & 1 \end{pmatrix}$
M6	-2684.74948335288	$-2E_{X^0}^D - V \begin{pmatrix} 1 & 0 \\ 0 & 1 \end{pmatrix} - V \begin{pmatrix} 1 & 2 \\ 0 & 1 \end{pmatrix} + V \begin{pmatrix} 2 & 0 \\ 0 & 0 \end{pmatrix}$
M7	-1338.35041463641	$-E_{X^0}^D - V \begin{pmatrix} 1 & 0 \\ 0 & 1 \end{pmatrix} - V \begin{pmatrix} 1 & 2 \\ 1 & 1 \end{pmatrix} + V \begin{pmatrix} 2 & 1 \\ 1 & 1 \end{pmatrix}$
M8	-1322.3916578874	$-E_{X^0}^D + V \begin{pmatrix} 1 & 1 \\ 1 & 0 \end{pmatrix} - V \begin{pmatrix} 1 & 2 \\ 1 & 1 \end{pmatrix}$
M9	-2671.74994554669	$-2E_{X^0}^D - V \begin{pmatrix} 1 & 0 \\ 0 & 1 \end{pmatrix} - V \begin{pmatrix} 1 & 2 \\ 1 & 1 \end{pmatrix} + V \begin{pmatrix} 2 & 0 \\ 1 & 0 \end{pmatrix}$
M10	13.2709672857624	$edF_0$
$F_0$	18	$X^0$ Anti-crossing Field
$t_{X^0}$	0.64950806	Tunneling coefficient for $X^0$ state
$t_{X_h^0}$	0.52678134	Tunneling coefficient for $X_h^0$ state
$t_{X^{2-}}$	.017	Tunneling coefficient for $X^{2-}$ state
$t_{X_h^{2-}}$	.95912583	Tunneling coefficient for $X_h^{2-}$ state
$t_{e^{2-}}$	.32436786	Tunneling coefficient for $e^{2-}$ state
$t_{e_h^{2-}}$	.50065926	Tunneling coefficient for $e_h^{2-}$ state

The tunneling coefficient values were extracted from the raw PL data and the values for M's were best guesses based on the published data for the particular VQDM sample.

### 7.2.3 MCMC simulation: what happens in a single iteration?

MCMC operates using millions and millions of iterations through parameter space. To understand the evolution of the final simulated data set, it is vital to understand a single iteration and a single run (the collection of thousands of iterations).

The first step for a single iteration is the initialization of the parameters that are being simulated. The selection rules for the values set is discussed in the previous section. Using these values and the theoretical model (e.g. Equation 7.5), MCMC recreates the spectral map and compares it to the real map. For each observable set, it calculates a likelihood value. This likelihood value is the sums of the log of the normal distribution density for each data point and the associated analytical expression and can be written as

$$Likelihood = \sum_{i=1}^{10} \log\left(\frac{1}{ye_i\sqrt{2\pi}} \exp - \frac{(y_i-yd_i)^2}{ye_i^2}\right) \quad (7.9)$$

where  $y_i$  is the experimental data,  $yd_i$  is the simulated line and  $ye_i$  is the confidence for each data point.  $y_i$  is the peak energy and  $ye_i$  is the confidence interval (standard deviation) of the peak calculated from the full width half maximum (FWHM) for each slice as described in section 7.1. The FWHM and standard deviation are related by

$$\sigma = \frac{FWHM}{2\sqrt{2\ln 2}} \quad (7.10)$$

In other words, the likelihood function is a sum over a point-by-point comparison of the experimental data to the theoretical PL energy values generated for a particular set of parameter values. This “goodness of fit” is weighted by the standard deviation. After the likelihood is generated, the program stores the Likelihood value associated with that particular observable set, i.e. the parameter values used for that simulation. This is a single iteration.

As multiple iterations are run, the program implements a Gibbs sampling in which it samples from the prior distribution by sequentially going through one observable at a time. In other words, for the 19 variables we are searching through, it varies only 1 parameter at a time, keeping the other 18 the same. After each parameter variation it calculates the likelihood with this new observable set. If the new likelihood is greater than the old likelihood, this variable set is retained and the previous dataset is discarded. This decision process forms a part of the acceptance rule. Our acceptance rule is based on the Hasting’s algorithm and is written as

$$\textit{If Likelihood}_{\textit{new}} > \textit{Likelihood} + \log(\textit{Random Number}) \quad (7.11)$$

If the log term were not included, the program would iterate to a “Best fit” as defined by the maximum value for the likelihood function. The inclusion of the log of a random number ensures that sporadically worse likelihood values are included. This ensures that the loop does not get trapped in a local maximum and instead samples a large enough range of values to find a global maximum. This entire process is looped and repeated thousands of times. We call this entire loop a single run.

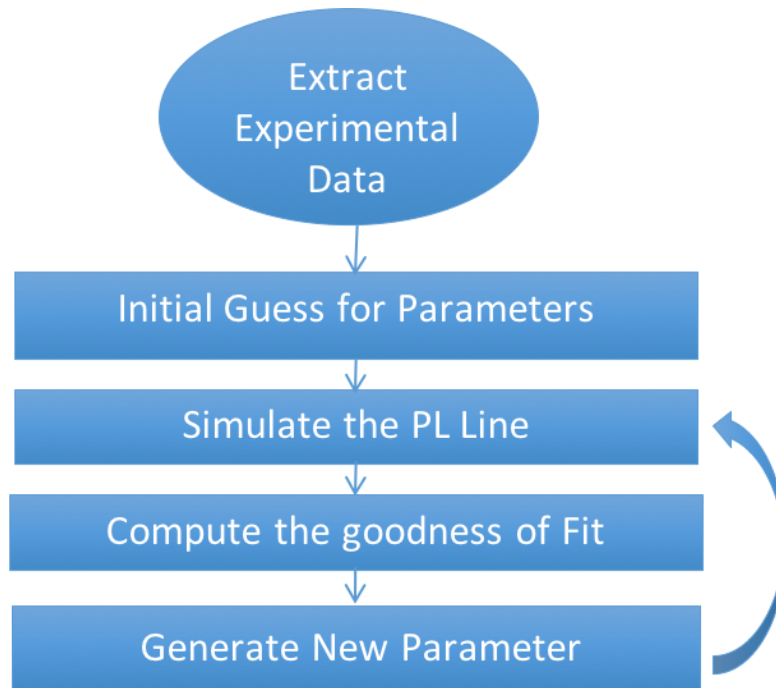


Figure 7.5: Flowchart for implementation of a single run of MCMC

#### 7.2.4 Burn in

Early iterations of MCMC do not have a high likelihood value associated with their simulated observable values. This is because the initial starting values are best guess and may not be from their prior distribution. These early runs are thus discarded and these discarded iterations are referred to as the “burn-in” period. During the “burn-in” period, the likelihood increases as more accurate parameter values are identified. The end of the “burn-in” period is marked by the end of the increase in likelihood.

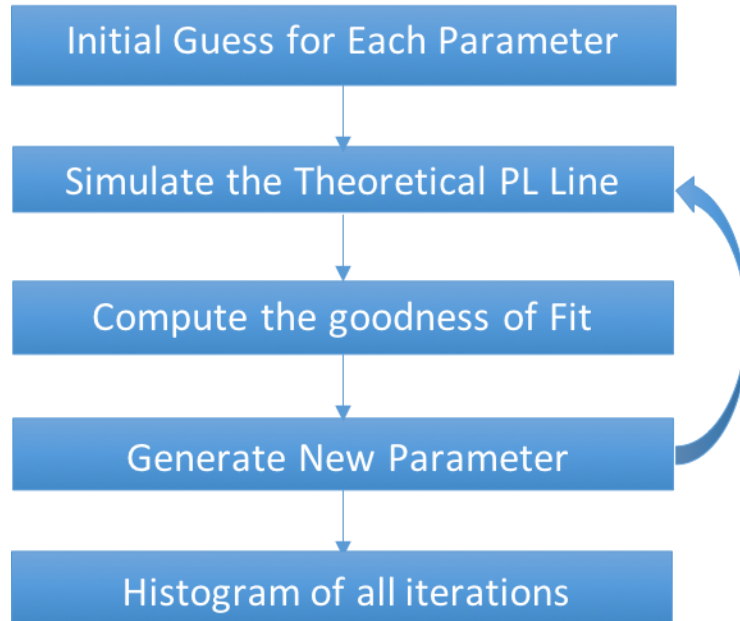


Figure 7.6: Flowchart for the final implementation of MCMC

### 7.2.5 MCMC Implementation

The fundamental difference between the burn-in and final implementation is the number of iterations for each run. For the case of the burn-in implementations, we only need good initial values and the number of runs can be small because our objective is to evolve to an observable set that would be good starting point for the final implementation. However, for the final implementation, ideally the program should search over as large a parameter space as possible. This is especially important when the number of parameters we are searching over is rather large, in our case 19. For our final implementation, the number of iteration used was 13.6 billion.

The observable dataset generated at the end of the burn in period is used as the initial values for the final implementation. Similar to the precursory implementation, Gibbs sampling is used to sequentially vary one variable at a time and likelihood is

calculated at each step. The same acceptance rule is implemented for each iteration. We simultaneously fit all experimental data to the analytical expressions. The algorithm explores a range of values for each observable and returns a histogram of all the values that give us an acceptable fit. A set of these histograms are shown in Figure 7.8. All the histograms are depicted as a figure in the appendix.

From the histogram of possible observable values, we determine the maximum likelihood value, the average value and the 95% confidence interval for each parameter. The complete set of observables are listed in table 7.3. These values are statistically distinct as measured by the 95% confidence intervals. This statistical difference validates the assertion that the returned values have a physical meaning and are not a result of fitting with too many free parameters. Figure 7.7 depicts the spectral map drawn using the observable values generated from the simulation. The blue line is simulated data and the red data points are the experimental data.

Table 7.3: Mean and confidence interval values for the observables generated using MCMC simulations

Observables	Mean	95% Conf. Interval
M1	1337.927351	[1337.927267, 1337.927436]
M2	1350.085848	[1350.085687, 1350.086009]
M3	-14.01516788	[-14.0153576, -14.01497816]
M4	-1349.995807	[-1349.99593, -1349.995684]
M5	-1337.941641	[-1337.941679, -1337.941603]

M6	-2684.94144	[-2684.941574, -2684.941306]
M7	-1320.226456	[-1320.232208, -1320.220703]
M8	-1305.53267	[-1305.538112, -1305.527227]
M9	-2655.588275	[-2655.593704, -2655.582846]
M10	13.90462226	[13.90442476, 13.90481977]
F0	20.10854015	[20.10845479, 20.10862551]
tX0	0.489842164	[0.489819389, 0.48986494]
tX0h	0.44574922	[0.445721585, 0.445776854]
tX2	0.378504916	[0.37848655, 0.378523283]
tX2h	70.04581657	[70.00867818, 70.08295497]
te2	0.260153293	[0.260128002, 0.260178584]
te2h	0.437334189	[0.437174286, 0.437494092]

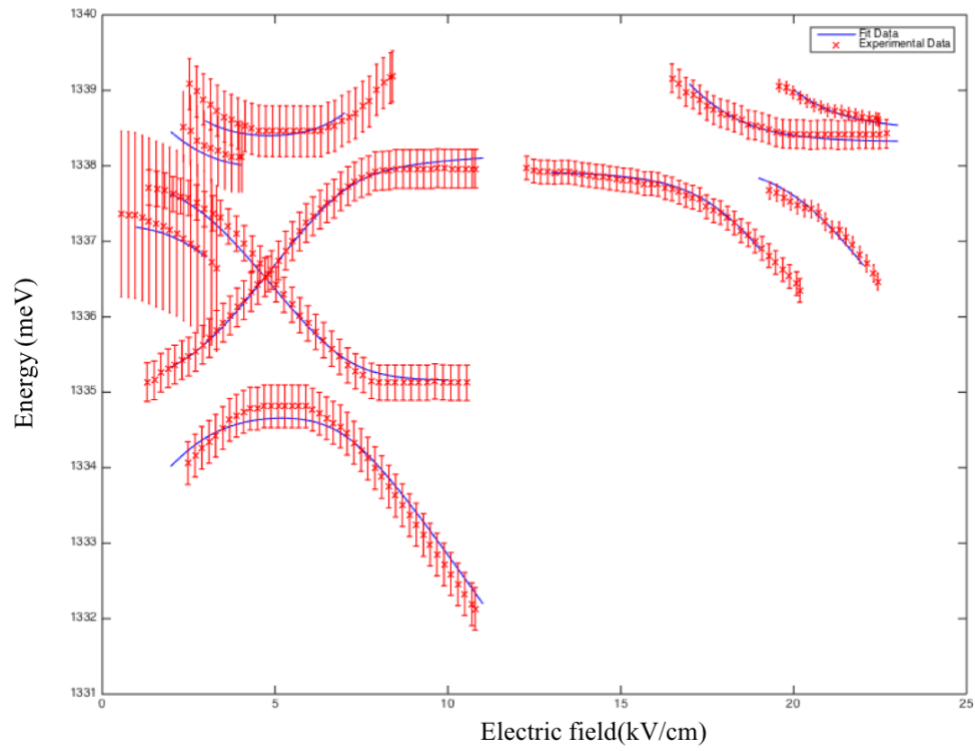


Figure 7.7: Spectral map reproduced using observable values generated from the MCMC run (blue line) against the experimental data (red points)

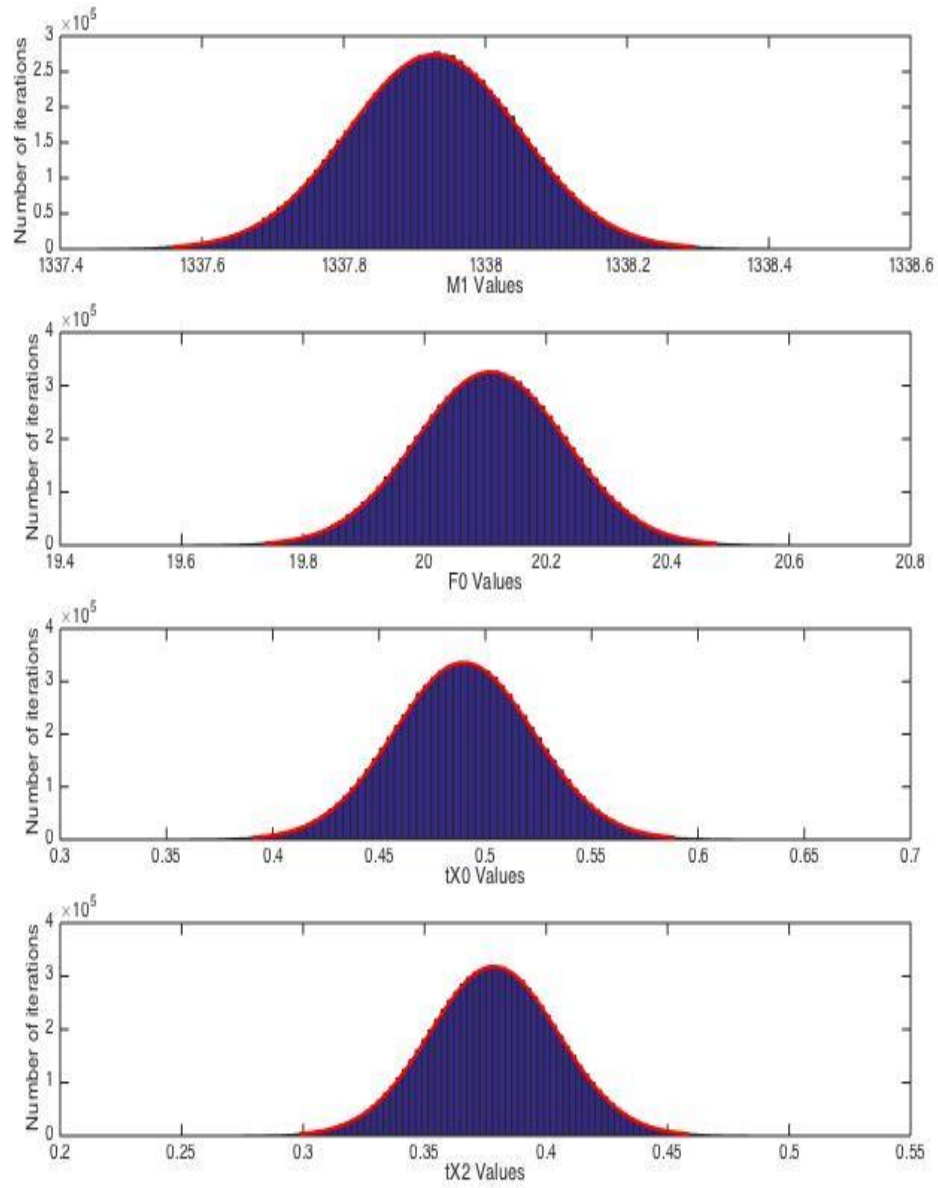


Figure 7.8 : Histogram of four observables generated at the end of the MCMC simulation.

### 7.3 Conclusions

The data extraction method demonstrated in this chapter allows us to extract comprehensive information from spectral lines. Complete information from spectral lines includes instrumental resolution and spectral broadening both of which were previously discarded. Overcoming this limitation enables us to extract accurate energy values from VQDM data with assigned error which hasn't been done previously. We also demonstrate the development and implementation of a novel adaptation of MCMC for analysis of spectroscopy data. This statistical technique allows us to extract accurate statistically valid quantitative values for uniquely identifiable parameters. As depicted in Figure 7.7, the excellent agreement of the analytical solutions within the confidence interval of the data demonstrates a conceptual check on the accuracy of the developed method. In the following chapter, we validate the robustness of this method to understand the scope of its implementation to other sparse and complex data systems.

## Chapter 8

### VALIDATION OF ADAPTED MCMC SIMULATION FOR SPECTROSCOPY DATA

The MCMC approach described in Chapter 7 returns millions of values for observables that are statistically distinct. To assess whether these results are dependent on the methods by which MCMC are implemented, we recompute the MCMC simulation using a variety of different starting values and computational approaches. Specifically, we vary the density of data points and size of the error bars. In all cases we compute and compare the mean, the maximum likelihood value, the confidence intervals and the prediction intervals for each of the different cases.

#### 8.1 Dependence on density of data point

##### 8.1.1 Dense data set

MCMC is known to be a relatively effective method for extracting results from sparse data sets<sup>65,66</sup>, but of course more and higher quality data will always yield more precise results. To understand the impact of the density of data points, we computed statistical properties of the generated distributions for two data sets. The “dense” data set is the data set extracted from the raw TIPL map using Lorentzian data analysis as described in Chapter 7, which is shown again in Figure 8.1. Implementing the novel data extraction technique described in Chapter 5 with the dense data set returns a set of mean values, confidence intervals, and most likely values for the observable parameters. These results are listed in Table 8.1.

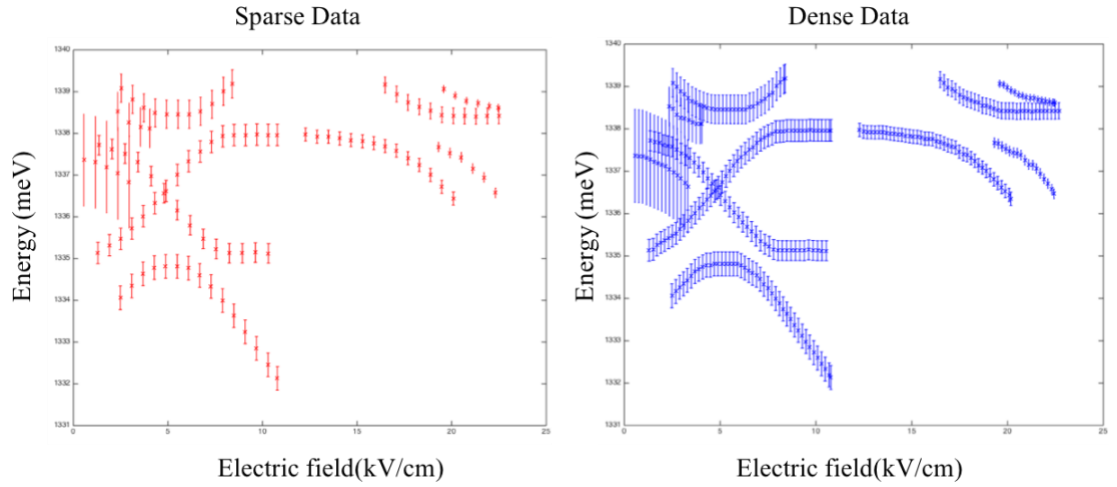


Figure 8.1: Sparse and dense data sets used to validate the robustness of MCMC

Table 8.1: Mean, maximum likelihood value and confidence interval values for the observables generated using a dense data set

Observables	Mean	95% Conf. Range	Highest Likelihood
M1	1337.927351	[1337.927267, 1337.927436]	1337.92091
M2	1350.085848	[1350.085687, 1350.086009]	1350.15868
M3	-14.01516788	[-14.0153576, -14.01497816]	-14.094965
M4	-1349.995807	[-1349.99593, -1349.995684]	-1350.0495
M5	-1337.941641	[-1337.941679, -1337.941603]	-1337.9321
M6	-2684.94144	[-2684.941574, -2684.941306]	-2684.9933
M7	-1320.226456	[-1320.232208, -1320.220703]	-1311.1547
M8	-1305.53267	[-1305.538112, -1305.527227]	-1296.9041

M9	-2655.588275	[-2655.593704, -2655.582846]	-2646.8719
M10	13.90462226	[13.90442476, 13.90481977]	13.9880184
F0	20.10854015	[20.10845479, 20.10862551]	20.0901329
tX0	0.489842164	[0.489819389, 0.48986494]	.48587813
tX0h	0.44574922	[0.445721585, 0.445776854]	.43219981
tX2	0.378504916	[0.37848655, 0.378523283]	.37842012
tX2h	70.04581657	[70.00867818, 70.08295497]	78.1458758
te2	0.260153293	[0.260128002, 0.260178584]	.26000817
te2h	0.437334189	[0.437174286, 0.437494092]	.41943924

The MCMC results for the dense data set are summarized in Table 8.1. The prediction intervals that are obtained using these values for the dense data set are plotted in Figure 8.2. The red points are the raw data extracted from the experimental data using the Lorentzian fits. The blue lines are the upper and lower bounds of the prediction interval. The black line is the simulated line using the maximum likelihood parameter values generated from the MCMC simulation.

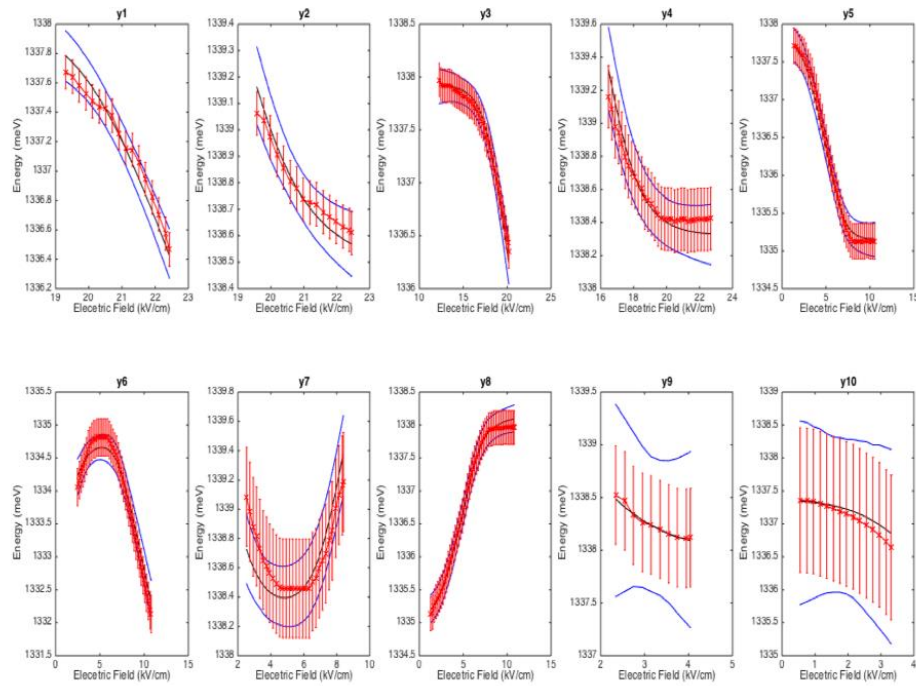


Figure 8.2: Individual plots for each spectral line depicting the simulated data generated from the maximum likelihood value for the observables (black), the experimental data (red) and the prediction interval (blue) for dense data set.

### 8.1.2 Sparse data set

The “sparse” data set shown in Figure 8.1 is constructed by discarding every other data point from the dense data set. We then repeat the MCMC simulation described in Chapter 7 using the sparse data set. The mean, 95% confidence interval, and highest likelihood values computed for the sparse data sets are listed in Table 8.2.

Table 8.2: Mean, maximum likelihood value and confidence interval values for the observables generated using a sparse data set

Observables	Mean	95% Conf. Range	Highest Likelihood
M1	1337.92341591418	[1337.92355126372, 1337.92328056464]	1337.87400448469
M2	1350.04159192867	[1350.04182191468, 1350.04136194265]	1350.05825607982
M3	-13.9538404918710	[-13.9535786698935, -13.9541023138485]	-14.0150712253153
M4	-1349.92018132470	[-1349.92000452397, -1349.92035812543]	-1349.88436103425
M5	-1337.93087989280	[-1337.93081557614, -1337.93094420946]	-1337.89122633014
M6	-2684.86231438427	[-2684.86212027240, -2684.86250849615]	-2684.82818404179
M7	-1323.06394202347	[-1323.05630383123, -1323.07158021571]	-1312.99012932288
M8	-1307.27763388172	[-1307.27078679044, -1307.28448097300]	-1296.98283683747
M9	-2657.28820868921	[-2657.28138694400, -2657.29503043442]	-2647.50374829147
M10	13.8381704239948	[13.8384438002335, 13.8378970477561]	13.9113599615551
F0	20.0479574450971	[20.0481062655012, 20.0478086246929]	20.0600009398205
tX0	0.482431985696073	[0.482473329059964, 0.482390642332181]	0.478835889775279
tX0h	0.438639485275929	[0.438691699074308, 0.438587271477551]	0.453131634055440
tX2	0.388986830172026	[0.389009624955479, 0.388964035388574]	0.398345350698992
tX2h	96.2513845340860	[96.3071060625039, 96.1956630056681]	131.678665172065
te2	0.267248244740020	[0.267296273484094, 0.267296273484094]	0.260791116050299

		0.267200215995945]	
te2h	0.397751269683208	[0.397968189741725, 0.397534349624692]	0.543066772217423

The prediction intervals that are obtained using these values for the dense data set are plotted in Figure 8.3. The red points are the raw data extracted from the experimental data using the Lorentzian fits. The blue lines are the upper and lower bounds of the prediction interval. The black line is the simulated line using the maximum likelihood parameter values generated from the MCMC simulation.

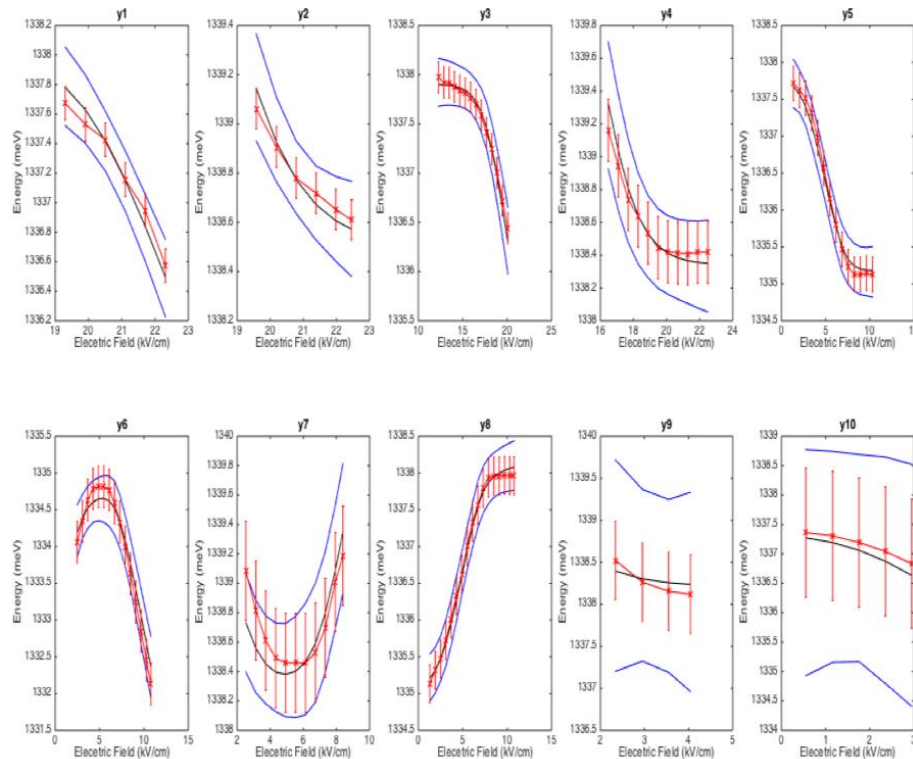


Figure 8.3: Individual plots for each spectral line depicting the simulated data generated from the maximum likelihood value for the observables (black), the experimental data (red) and the prediction interval (blue) for sparse data set.

### 8.1.3 Comparison between MCMC simulations using dense and sparse data sets

To compare the results of the fits to the dense and sparse data sets, we compute the percentage difference between the two results. The percentage difference between the mean and the max likelihood values are reported in Table 8.3

Table 8.3: Comparison of mean and maximum likelihood values of observables generated from dense and sparse data

Observables	Maximum Likelihood % Diff	Mean % Diff
M1	0.0035062	0.000294118
M2	0.0074382	0.003278019
M3	0.56682402	0.437578691
M4	0.01223284	0.005601919
M5	0.00305458	0.000804303
M6	0.00614992	0.002947015
M7	-0.1399849	-0.214924191
M8	-0.0060679	-0.133659151
M9	-0.0238725	-0.064013451
M10	0.54802943	0.477911839
F0	0.14998392	0.301278484
tX0	1.4493849	1.512768571
tX0h	-4.84309	1.595007777
tX2	-5.2653741	-2.769294064

tX2h	-68.503666	-37.41203864
te2	0.39864341	-2.7272
te2h	-14.073636	9.050954696

The  $M_s$  and  $F_0$  values differ by no more than .5%, which suggests that the MCMC approach has a high degree of precision even for systems with sparse data sets. The  $t$  values, on the other hand, have a larger percentage difference. This likely arises because the number of data points at the anti-crossings, which are essential to deriving  $t$  values are reduced in the sparse data sets. We note that the percent error is significantly higher for  $t_{h^+}^{X^{2-}}$  and  $t_{h^+}^{e^{2-}}$ . We believe this occurs because there are relatively few extracted data points at the anticrossing for these spectral lines even in the dense data set. This comparison shows that the MCMC approach is robust against data density.

## 8.2 Sensitivity to size of error bars

As discussed in Chapter 7, the standard deviation used as the measurement errors for the MCMC simulations were generated from the FWHM values of the Lorentzian fit. To assess the sensitivity of our results to this step, we reran the simulations under two different conditions: increasing and decreasing the error bars by 25%. Again, we assess the sensitivity with a percentage comparison between the mean values for the parameters using these two approaches. In Table 8.4, we report the

percentage difference, relative to the results computed with the standard error bars (Table 8.1), for the data sets with 25% larger and 25% smaller error bars.

Table 8.4: Comparison of mean values of parameters for data sets with 25% larger error and 25% smaller error

Observables	Larger Error Bars	Smaller Error Bars
M1	0.00775499	-0.0005014
M2	0.0063925	-0.0024913
M3	0.04359681	-0.2287486
M4	0.00709292	-0.0018406
M5	0.00486922	-0.000007189
M6	0.0035725	-0.0010408
M7	2.30745787	-0.4138154
M8	2.53941126	-0.2794596
M9	1.2519261	-0.137636356
M10	-0.1343313	-0.2115977
F0	-0.0656882	0.00119073
tX0	-0.2581013	0.1538147
tX0h	2.10752922	-0.1628648
tX2	-2.8924852	-0.4120246
tX2h	-359.3316	-61.499589
te2	-1.6242555	0.37963208
te2h	13.1833502	7.61873969

We see that the error is below 3 % for all parameters except the tunneling coefficients, which suggests that the MCMC approach is relatively insensitive to the magnitude of the measurement error. We know from implementing MCMC on dense data sets that there is a strong dependence of the tunneling coefficient value on the density of data points from the anticrossing region. Changing the size of error bars changes the confidence interval and thus the range of acceptable values possible at the

anticrossing. The large percentage difference for these parameters is therefore attributed to the sensitivity of these parameters to the data at the anticrossing. Both increased density of data points and tighter error bars will improve the precision of the MCMC parameter estimation.

### **8.3 Summary**

We sought to assess the robustness of the adapted MCMC model by analyzing the dependence of the simulated observable data set on the density of data points and size of the error bars. First, we studied the dependence on the density of data points and observed no more than 0.5% difference between the dense and sparse data sets. We then varied the size of the error associated with the data set and again observed a small difference in the mean values generated from the distribution of the observables generated from the two error bar varied data sets. However, tunneling coefficient values show significantly larger sensitivity to both data density and size of error bars. We believe this is due to the inherent strong dependence of the tunneling values on the data at the anti-crossing. These robustness validations demonstrate the strength of the developed model against variations in data density size and error, but they also highlight the importance of obtaining more and more precise values at the anti-crossing points.

## Chapter 9

### SUMMARY AND FUTURE WORK

The objective of this dissertation was to utilize experimental and data analysis methods to characterize nanostructured semiconductors of interest for next generation optoelectronic devices. First, we investigated the mechanism of charge carrier transfer in a nanocomposite consisting of rare earth nanoinclusions and InAs QDs within a III-V host. Second, we developed, demonstrated, and assessed the sensitivity of a new Markov Chain Monte Carlo method for extracting statistically-valid values for observables from spectroscopic data of vertically-coupled InAs QD complexes called Quantum Dot Molecules. Here we summarize the results.

Past studies of ErAs NP hybrid composites concluded that both tunneling and FRET were possible charge carrier transfer mechanisms in this material system. To conclusively determine the dominant transfer mechanism, we used time resolved photoluminescence measurements to quantify the PL lifetime of ErAs hybrid nanocomposites as a function of sample structure. We investigated three samples, which were designed with and without AlGaAs in the barrier separating the ErAs NP from the InAs QDs. Fluence- and temperature-dependence time resolved measurements revealed a difference in the QD PL lifetime of .2ns between the samples of equal barrier thickness but different barrier composition. FRET efficiency calculations that account for the difference in dielectric constant between these two structures predict that there should be no statistically-significant difference in the rate of carrier transfer. Moreover, these calculations show that there is a very low

probability of FRET transfer on the length scales being studied in these samples. These two pieces of evidence conclusively establish tunneling as the dominant mechanism of charge transfer. The method employed and described here can be applied to study charge carrier dynamics and material properties in other composite hybrids such as TbAs:GaAs, TbAs:InGaAs and ErAs:InGaAs. TbAs:GaAs<sup>67</sup> and ErAs:InGaAs<sup>68</sup> have been studied previously with optical pump and terahertz probe transient absorption spectroscopy, but not with time resolved photoluminescence spectroscopy to probe the charge carrier dynamics when the rare earth nanoinclusions are coupled to an optically active component such as a QD. Performing such an analysis will add to the body of knowledge that supports the development of novel optoelectronic devices.

Vertically-stacked QDMs are of great interest for QIP because of tunable emission and other properties that provide additional tools to manipulate quantum state. Design and development of scalable devices based on QDMs depends critically on the quantitative values for the physical parameters such as tunneling coefficients, stark shifts, and many body interactions. Values for these parameters have conventionally been derived from visually-analyzed spectral data. The limitations of this conventional data analysis technique transfer statistical uncertainty to the derived physical parameter values. The focus of this dissertation was to develop a raw data extraction and processed data analysis technique that would overcome the limitations of the conventional data analysis. There were three major components to this effort. First, we developed data extraction process that allows the inclusion of information from the resolution of the instrument and broadening of spectral lines. The process of fitting individual slices of spectral data to a Lorentzian function allowed the

assignment of an error for each data point. This inclusion of the complete data is in itself a leap from the partially extracted traditional data and has achieved the first component of developing a unique data processing technique for VQDM time integrated photoluminescence data. Second, we developed and employed an adapted Markov Chain Monte Carlo integration method to derive statistically valid physical parameters from spectroscopic data. For unique solutions, MCMC simulations can only be implemented on uniquely identifiable parameters. The uniquely identifiable parameters / observables that comprehensively describe the model were derived from the analytical expressions that describe the model. The generated predictions for the observables provided by the simulations demonstrated an exceptional fit to the experimental data. Third, we assessed the sensitivity of this MCMC method by changing the size of the error and data density. We found less than 1% variation in simulated values when the data density was varied and a less than .001% when the size of the error bars is changed by 25%. This difference is negligible for higher dimensional data sets like the one analyzed here. This exceptional fit and the analysis of the robustness of the method demonstrate that we have developed a statistically valid technique for data analysis.

Although the MCMC method allows us to extract statistically-valid and accurate values for the observables, these observables are a linear combination of fundamental physical parameters for which we would like to have quantitative values. For example,

$$M1 = E_{X_0}^D + V \begin{pmatrix} 0 & 1 \\ 0 & 1 \end{pmatrix} \quad (8.1)$$

where  $E_{X_0}^D$  is the direct exciton energy for a neutral exciton and  $V \begin{pmatrix} 0 & 1 \\ 0 & 1 \end{pmatrix}$  is the Coulomb interaction term between a single electron and hole. Deconvolving the value

of each fundamental parameter from the value for the observable is an important next step, but this cannot be done directly from the MCMC results because there are no experimentally verifiable values for parameters such as Coulomb interaction terms. To overcome this challenge and extend the MCMC approach to extract values for each physical parameter, we need additional constraints, which will have to come from theory. For example, theoretical bounds on  $V \begin{pmatrix} 0 & 1 \\ 0 & 1 \end{pmatrix}$  would constrain  $M1$  and allow us to extract precise statistically valid values for  $E_{X^0}^D$  directly from spectroscopy data.

Even if the above efforts to extract individual values for the distinct physical parameters proves impossible, the adapted MCMC technique developed and demonstrated here can be deployed for analysis of sparse spectroscopy data. For example, many groups routinely use time integrated spectroscopic data as a function of electric and magnetic field to understand the change of  $g$  factor. The adoption of this new MCMC method for statistically-valid data analysis for complex spectral data is likely to accelerate the design and development of the material foundations for a new generation of QIP devices by allowing the extraction of accurate design and fabrication values.

## REFERENCES

1. Kawasaki, J. K. *et al.* Local Density of States and Interface Effects in Semimetallic ErAs Nanoparticles Embedded in GaAs. *Phys. Rev. Lett.* **107**, 36806 (2011).
2. Kadow, C. *et al.* Self-assembled ErAs islands in GaAs: Growth and subpicosecond carrier dynamics. *Appl. Phys. Lett.* **75**, 3548 (1999).
3. Kadow, C., Jackson, A. W., Gossard, A. C., Matsuura, S. & Blake, G. A. Self-assembled ErAs islands in GaAs for optical-heterodyne THz generation.
4. Brown, E. R. *et al.* Evidence for a Strong Surface-Plasmon Resonance on ErAs Nanoparticles in GaAs. *Phys. Rev. Lett.* **90**, 77403 (2003).
5. Müller, K. *et al.* High-fidelity optical preparation and coherent Larmor precession of a single hole in an (In,Ga)As quantum dot molecule. *Phys. Rev. B* **85**, 241306 (2012).
6. Doty, M. *et al.* Optical spectra of doubly charged quantum dot molecules in electric and magnetic fields. *Phys. Rev. B* **78**, 115316 (2008).
7. Doty, M. F. *et al.* Hole-spin mixing in InAs quantum dot molecules. *Phys. Rev. B* **81**, 35308 (2010).
8. Liu, W., Bracker, A. S., Gammon, D. & Doty, M. F. Dynamic hole trapping in InAs/AlGaAs/InAs quantum dot molecules. *Phys. Rev. B - Condens. Matter Mater. Phys.* **87**, 1–7 (2013).
9. Kimball, G. E. The Electronic Structure of Diamond Effective masses and electronic structure of diamond including electron correlation effects in first principles calculations using the GW-approximation The Electronic Structure of Diamond. *J. Chem. Phys. J. Chem. Phys. J. Appl. Phys. J. Appl. Phys. J. Appl. Phys. Appl. Phys. Rev.* **311**, 32139–1579 (1935).
10. Heterojunction. *Wikipedia*
11. Aharonovich, I., Englund, D. & Toth, M. Solid-state single-photon emitters. *Nat. Photonics* **10**, 631–641 (2016).

12. Patricia M. A. Farias, \*,† *et al.* Fluorescent II–VI Semiconductor Quantum Dots in Living Cells: Nonlinear Microspectroscopy in an Optical Tweezers System. (2008). doi:10.1021/JP0758465
13. Ottesen, V. Molecular beam epitaxy. [https://en.wikipedia.org/wiki/Molecular\\_beam\\_epitaxy](https://en.wikipedia.org/wiki/Molecular_beam_epitaxy)
14. Davies, J. H. *The Physics of Low-Dimensional Semiconductors*. (Cambridge University Press, 1997). doi:10.1017/CBO9780511819070
15. Grundmann, M. & Bimberg, D. Formation of quantum dots in twofold cleaved edge overgrowth. *Phys. Rev. B* **55**, 4054–4056 (1997).
16. Petroff, P. M. & DenBaars, S. P. MBE and MOCVD growth and properties of self-assembling quantum dot arrays in III–V semiconductor structures. *Superlattices and Microstructures* **15**, 15 (1994).
17. Fitzgerald, A. No Title. [https://en.wikipedia.org/wiki/Finite\\_potential\\_well](https://en.wikipedia.org/wiki/Finite_potential_well)
18. Haffouz, S. *et al.* Growth and fabrication of quantum dots superluminescent diodes using the indium-flush technique: A new approach in controlling the bandwidth. *J. Cryst. Growth* **311**, 1803–1806 (2009).
19. Doty, M. F. *et al.* Antibonding ground states in InAs quantum-dot molecules. *Phys. Rev. Lett.* **102**, 1–4 (2009).
20. Fermann, M. E., Hanna, D. C., Shepherd, D. P., Suni, P. J. & Townsend, J. E. Efficient operation of an Yb-sensitised Er fibre laser at 1.56  $\mu\text{m}$ . *Electron. Lett.* **24**, 1135 (1988).
21. Said, M., Bertoni, C. M., Fasolino, A. & Ossicini, S. Electronic structure of rare earth arsenide/gallium arsenide superlattices. *Solid State Commun.* **100**, 477–480 (1996).
22. Nathan, V., Mitra, S. S. & Guenther, A. H. Review of multiphoton absorption in crystalline solids. *J. Opt. Soc. Am. B* **2**, 294 (1985).
23. Poole, I., Singer, K. E., Peaker, A. R. & Wright, A. C. Growth and structural characterization of molecular beam epitaxial erbium-doped GaAs. *J. Cryst. Growth* **121**, 121–131 (1992).
24. Burke, P. G. *et al.* Electrically active Er doping in InAs,  $\text{In}_{0.53}\text{Ga}_{0.47}\text{As}$ , and GaAs. *Appl. Phys. Lett.* **101**, 232103 (2012).
25. Kadow, C. *et al.* Self-assembled ErAs islands in GaAs: Growth and

- subpicosecond carrier dynamics Carrier dynamics in self-assembled ErAs nanoislands embedded in GaAs measured by optical-pump terahertz- probe spectroscopy Self-assembled ErAs islands in GaAs: Growth and subp. *Cit. Appl. Phys. Lett. Appl. Phys. Lett. Appl. Phys. Lett. Appl. Phys. Lett.  $\mu$ m Appl. Phys. Lett. Appl. Phys. Lett.* **75**, 251119–3116 (1999).
26. Zhang, Y. *et al.* Stacking InAs quantum dots over ErAs semimetal nanoparticles on GaAs (0 0 1) using molecular beam epitaxy. (2017). doi:10.1016/j.jcrysgro.2017.02.042
  27. Schroder, D. K. *Semiconductor material and device characterization*. (IEEE Press, 2006).
  28. Pankove, J. I. *Optical processes in semiconductors*. (Dover, 1975).
  29. Gammon, D., Snow, E. S., Shanabrook, B. V., Katzer, D. S. & Park, D. Homogeneous Linewidths in the Optical Spectrum of a Single Gallium Arsenide Quantum Dot. *Science* **273**, 87–90 (1996).
  30. Koukaras, E. N. *Fermi's Golden Rule*.
  31. Ashcroft, N. W. & Mermin, N. D. *Solid state physics*. (Holt, Rinehart and Winston, 1976).
  32. Perinetti, U. *Optical Properties of Semiconductor Quantum Dots*. (2011).
  33. Poenariu, V. Influence of lateral electric field in InAs-Quantum Dots. (Ruhr-Universität Bochum, 2005).
  34. Warburton, R. J. *et al.* Optical emission from a charge-tunable quantum ring. *Nature* **405**, 926–929 (2000).
  35. Zhou, X. SPECTROSCOPIC PROPERTIES OF SELF-ASSEMBLED LATERAL QUANTUM DOT MOLECULES. (2015).
  36. Haughn, C. R. *et al.* Carrier transfer from InAs quantum dots to ErAs metal nanoparticles. *Appl. Phys. Lett.* **105**, 1–5 (2014).
  37. Crook, A. M., Nair, H. P. & Bank, S. R. Surface segregation effects of erbium in GaAs growth and their implications for optical devices containing ErAs nanostructures. *Appl. Phys. Lett.* **98**, 121108 (2011).
  38. Cario, G. Von & Franck, J. Ober Zerlegung von Wasserstoffmolekiilen durch angeregte Quecksilberatome.

39. Förster, T. Zwischenmolekulare Energiewanderung und Fluoreszenz. *Ann. Phys.* **437**, 55–75 (1948).
40. Davidson, M. W. (The F. S. U., Piston, D. W. (Vanderbilt U. & Kremer, G.-J. (Vanderbilt U. Basics of FRET Microscopy | MicroscopyU. Available at: <https://www.microscopyu.com/applications/fret/basics-of-fret-microscopy>. (Accessed: 13th March 2018)
41. Sekar, R. B. & Periasamy, A. Fluorescence resonance energy transfer (FRET) microscopy imaging of live cell protein localizations. *J. Cell Biol.* **160**, 629–33 (2003).
42. Stryer, L. & Hauglandt, R. P. ENERGY TRANSFER: A SPECTROSCOPIC RULER\*.
43. *IUPAC Compendium of Chemical Terminology*. (IUPAC, 2009). doi:10.1351/goldbook
44. Hochstrasser, R. M. *Excited states of biological molecules: edited by J. B. Birks, published by John Wiley and Sons, London, New York, Toronto, Sydney, 1976. Trends in Biochemical Sciences* **1**, (Elsevier Current Trends, 1976).
45. Steinberg, I. Z. Nonradiative Energy Transfer in Systems in which Rotatory Brownian Motion is Frozen. *J. Chem. Phys.* **48**, 2411–2413 (1968).
46. Waterman, P. C. Matrix formulation of electromagnetic scattering. *Proc. IEEE* **53**, 805–812 (1965).
47. Stroud, D. & Kazaryan, A. Optical sum rules and effective-medium theories for a polycrystalline material: Application to a model for polypyrrole. *Phys. Rev. B* **53**, 7076–7084 (1996).
48. Haughn, C. Energy transfer in nanostructured materials. (University of Delaware, 2014).
49. Greilich, A., Carter, S. G., Kim, D., Bracker, A. S. & Gammon, D. Optical control of one and two hole spins in interacting quantum dots. *Nat. Photonics* **5**, 702–708 (2011).
50. Krenner, H. J. *et al.* Direct Observation of Controlled Coupling in an Individual Quantum Dot Molecule. *Phys. Rev. Lett.* **94**, 57402 (2005).
51. He, Y. *et al.* Dynamically Controlled Resonance Fluorescence Spectra from a Doubly Dressed Single InGaAs Quantum Dot. *Phys. Rev. Lett.* **114**, 97402

- (2015).
52. Warburton, R. J. Single spins in self-assembled quantum dots. *Nat. Publ. Gr.* **12**, (2013).
  53. Economou, S. E. *et al.* Scalable qubit architecture based on holes in quantum dot molecules. *Phys. Rev. B* **86**, 85319 (2012).
  54. Liu, W. *Characterizing and engineering tunable spin functionality inside InAs/GaAs quantum dot molecules.* (2013).
  55. Wellalage, N. K. W., Zhang, T. & Dwight, R. Calibrating Markov Chain–Based Deterioration Models for Predicting Future Conditions of Railway Bridge Elements. *J. Bridg. Eng.* **20**, 4014060 (2015).
  56. Apenteng, O. O. & Ismail, N. A. A Markov Chain Monte Carlo Approach to Estimate AIDS after HIV Infection. *PLoS One* **10**, e0131950 (2015).
  57. Tu, Z., Chen, X., Yuille, A. L. & Zhu, S.-C. Image Parsing: Unifying Segmentation, Detection, and Recognition. *Int'l J. Comput. Vis.* (2005).
  58. Gilks, W. R. (Wally R. ., Richardson, S. (Sylvia) & Spiegelhalter, D. J. *Markov chain Monte Carlo in practice.* (Chapman & Hall, 1996).
  59. Syversveen, A. R. *NONINFORMATIVE BAYESIAN PRIORS. INTERPRETATION AND PROBLEMS WITH CONSTRUCTION AND APPLICATIONS.*
  60. Metropolis, N. & Ulam, S. The Monte Carlo Method. *J. Am. Stat. Assoc.* **44**, 335–341 (1949).
  61. Jarosz, W. *EFFICIENT MONTE CARLO METHODS FOR LIGHT TRANSPORT IN SCATTERING MEDIA. (UNIVERSITY OF CALIFORNIA, SAN DIEGO).*
  62. Schubert, E. F., Göbel, E. O., Horikoshi, Y., Ploog, K. & Queisser, H. J. Alloy broadening in photoluminescence spectra of Al<sub>x</sub>Ga<sub>1-x</sub>As. *Phys. Rev. B* **30**, 813–820 (1984).
  63. Bracker, A. S. *et al.* Engineering electron and hole tunneling with asymmetric InAs quantum dot molecules. *Appl. Phys. Lett.* **89**, 233110 (2006).
  64. Ponomarev, I. V *et al.* Theory of spin states in coupled quantum dots. *stat. sol. phys. stat. sol. PACS* **73217021**, 3869–3873 (2006).

65. Dodds, M. G. & Vicini, P. Assessing Convergence of Markov Chain Monte Carlo Simulations in Hierarchical Bayesian Models for Population Pharmacokinetics. *Ann. Biomed. Eng.* **32**, 1300–1313 (2004).
66. Bonassi, F. V., Chan, C. & West, M. Bayesian analysis of immune response dynamics with sparse time series data. (2016).
67. Vanderhoef, L. R. *et al.* Charge carrier relaxation processes in TbAs nanoinclusions in GaAs measured by optical-pump THz-probe transient absorption spectroscopy. *Phys. Rev. B* **89**, 45418 (2014).
68. Azad, A. K. *et al.* Carrier dynamics in InGaAs with embedded ErAs nanoislands. doi:10.1063/1.2989127

## Appendix A

### HISTOGRAM OF ALL OBSERVABLES

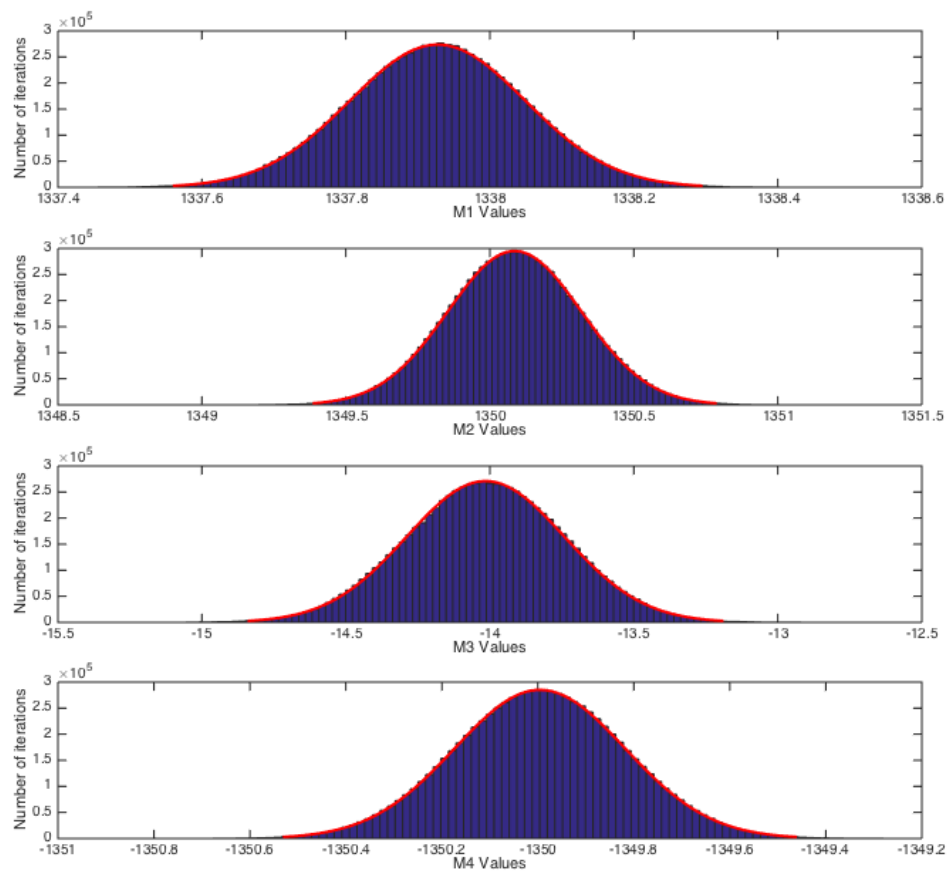


Figure A.1: Histogram of M1, M2, M3 and M4 generated at the end of the MCMC simulation.

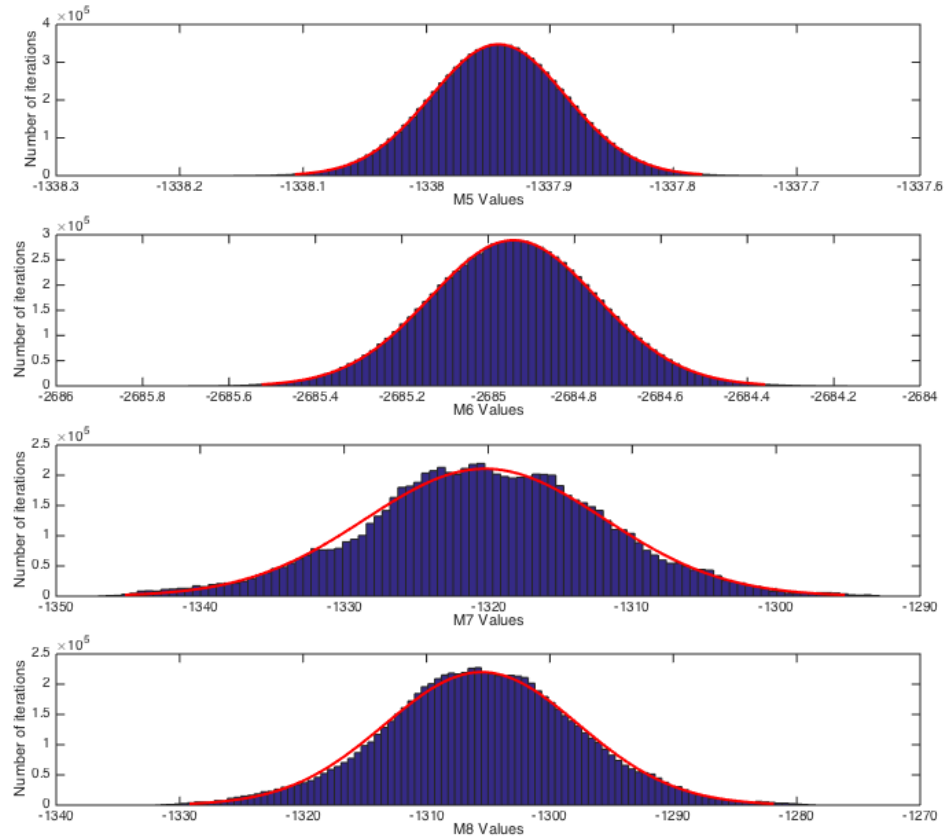


Figure A.2: Histogram of M5, M6, M7 and M8 generated at the end of the MCMC simulation.

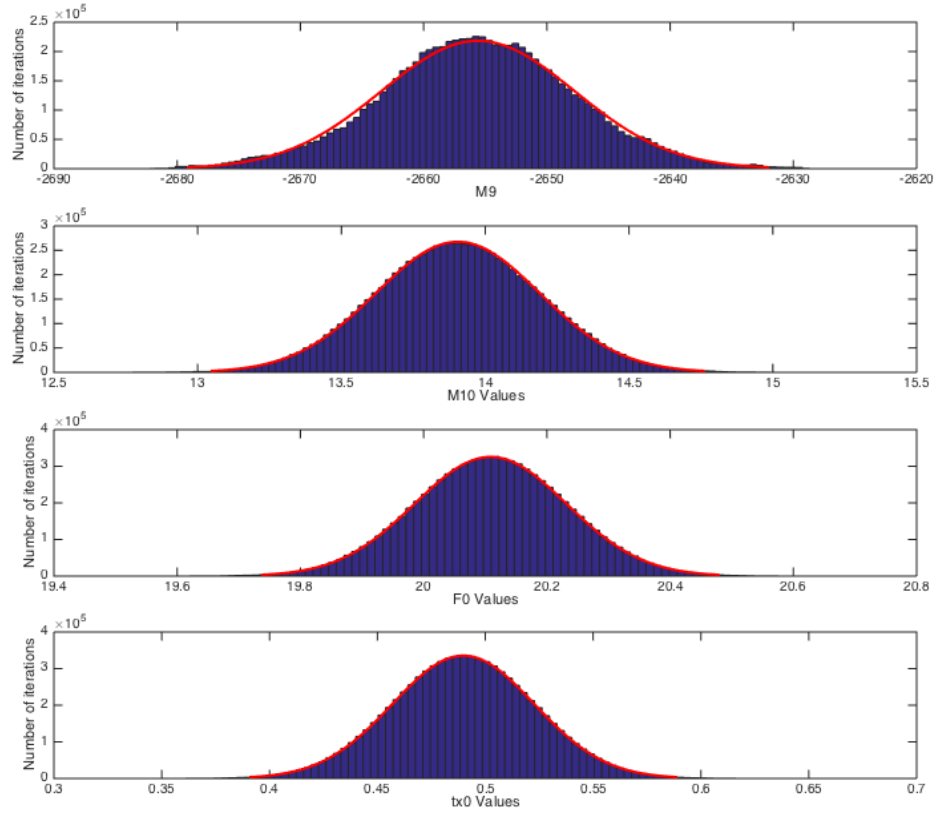


Figure A.3: Histogram of  $M9$ ,  $M10$ ,  $F_0$  and  $t_{x^0}$  generated at the end of the MCMC simulation.

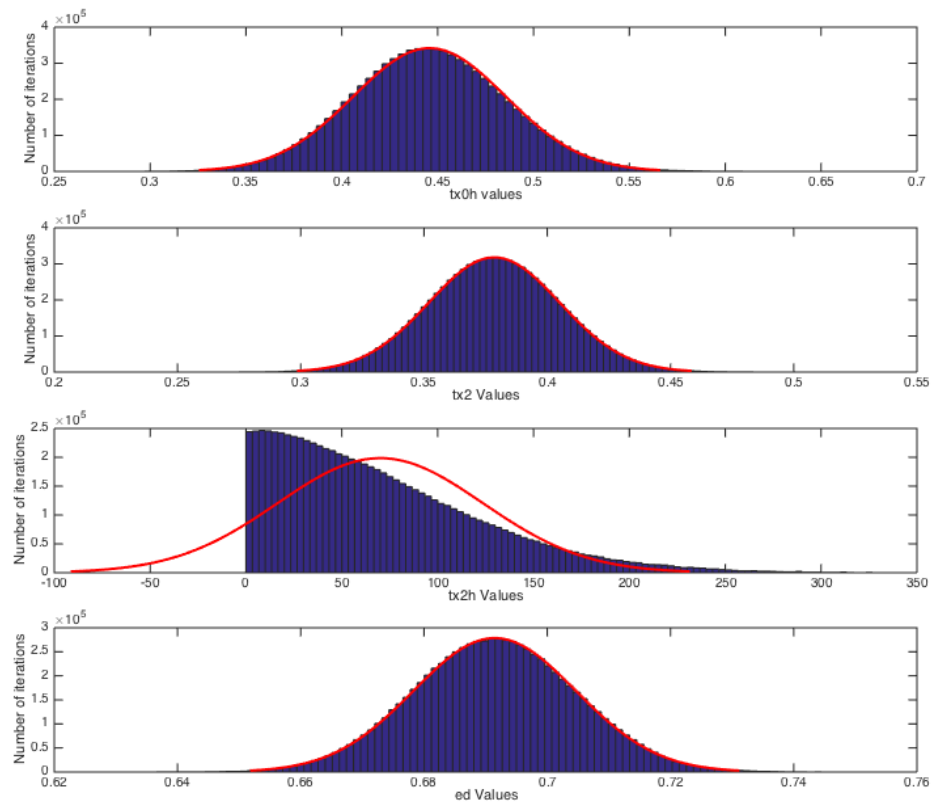


Figure A.4: Histogram of tx0h, tx2, tx2h and ed generated at the end of the MCMC simulation.

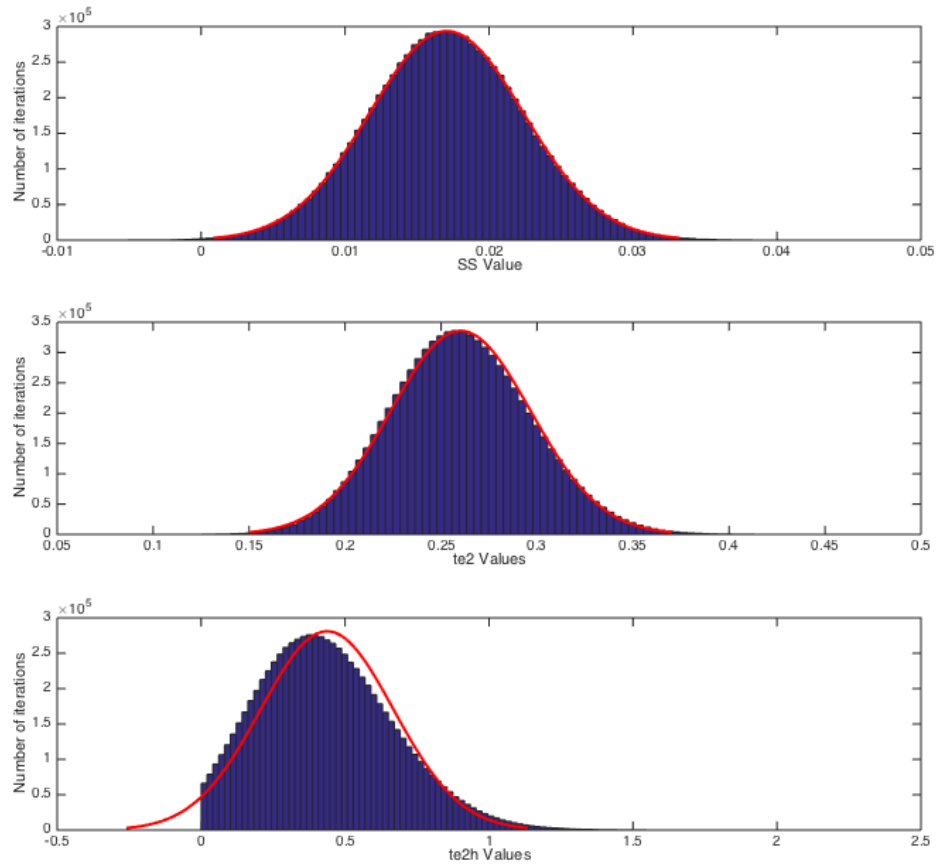


Figure A.5: Histogram of SS, te2 and te2h generated at the end of the MCMC simulation.

## Appendix B

### ADAPTED MCMC MATLAB CODE

```
rng('shuffle'); %randomize timer
warning('off','all');%probably unnecessary, but prevents annoying
output
%load('DataThiefSparse_20171127.mat');
load('DataThief_20180203.mat');%largererror
numbertosave=500000;
gibbs=18;
subsample = gibbs*10;
MCMCNum=numbertosave*subsample;%The number of chain iterations.

LIKELIHOOD=zeros(numbertosave,1);% A matrix that stores the
likelihood
%function value for every step of the MCMC chain

PARASET=zeros(numbertosave,19);% A matrix that store the parameter
sets
%for every step of the MCMC chain

INITS = [1337.805773
1350.056661
-14.07617397
-1349.878327
-1337.859244
-2684.833742
-1291.140874
-1274.21211
-2623.39167
13.9873383
20.08085601
0.49737407
0.431110324
0.388659224
321.8925483
0.696550899
0.023266792
0.249487527
0.26953968];

M1MEAN = INITS(1);
M2MEAN = INITS(2);
M3MEAN = INITS(3);
```

```

M4MEAN = INITS(4);
M5MEAN = INITS(5);
M6MEAN = INITS(6);
M7MEAN = INITS(7);
M8MEAN = INITS(8);
M9MEAN = INITS(9);
M10MEAN = INITS(10);
F0MEAN = INITS(10)/INITS(16);
tx0MEAN = INITS(12);
tx0hMEAN = INITS(13);
tx2mMEAN = INITS(14);
tx2mhMEAN = INITS(15);
edMEAN = INITS(16);
SSMEAN = INITS(17);
te2mMEAN = INITS(18);
te2mhMEAN = INITS(19);

M1STD = 0.4;%0.844172218;%0.017901887;
M2STD = 0.9;%2.591965188;%0.279402744;
M3STD = 0.8;%1.600978894;%0.365982233;
M4STD = 0.6;%0.710223363;%0.018416442;
M5STD = 0.2;%0.058075671;%0.021825919;
M6STD = 0.6;%1.126713934;%0.051546286;
M7STD = 17;%20.423444445;%5.003198626;
M8STD = 15;%5.045327929;%0.736777498;
M9STD = 15;%6.177849581;%0.000000000341; %Note that M9 actually has
a uniform prior
M10STD = 0.8;%0.97432729;%0.018452449;
%F0STD = 1;%5.064049188;
tx0STD = 0.2;%0.324942585;%0.185346429;%Do I need to update these
STDs because of the switch to t squared?
tx0hSTD = 0.3;%0.337152848;%0.22118963;
tx2mSTD = 0.03;%0.107323097;%0.052015686;
tx2mhSTD= 95;%0.194159319;%1.013706921;
edSTD = 0.05;%0.099382212;%0.004414177;
SSSTD = 0.02;%0.021852105;%0.00395455;
te2mSTD= 0.2;%0.112450492;%0.004883379;
te2mhSTD= 0.5;%0.019800042;%0.004003845;

M1INI = M1MEAN;
M2INI = M2MEAN;
M3INI = M3MEAN;
M4INI = M4MEAN;
M5INI = M5MEAN;
M6INI = M6MEAN;
M7INI = M7MEAN;
M8INI = M8MEAN;
M9INI = M9MEAN;
M10INI = M10MEAN;
F0INI = F0MEAN;
tx0INI = tx0MEAN;

```

```

tx0hINI = tx0hMEAN;
tx2mINI = tx2mMEAN;
tx2mhINI = tx2mhMEAN;
te2mINI = te2mMEAN;
te2mhINI = te2mhMEAN;
edINI = edMEAN;
SSINI = SSMEAN;

Para=[M1INI M2INI M3INI M4INI M5INI M6INI M7INI M8INI M9INI M10INI
F0INI tx0INI tx0hINI tx2mINI tx2mhINI edINI SSINI te2mINI te2mhINI];
%Set the initial parameter matrix to the initialization values
PARASET(1,:)=Para;
M1=Para(1);
M2=Para(2);
M3=Para(3);
M4=Para(4);
M5=Para(5);
M6=Para(6);
M7=Para(7);
M8=Para(8);
M9=Para(9);
M10=Para(10);
F0=Para(11);
tx0=Para(12);
tx0h=Para(13);
tx2m=Para(14);
tx2mh=Para(15);
ed=Para(16);
SS=Para(17);
te2m=Para(18);
te2mh=Para(19);

% Now calculate the new likelihood function for this new set of
% parameter values
y1d=0.5*((2*M1)+M10 -ed*(x1))-sqrt((M10-ed*(x1)).^2+4*tx0))+SS*x1;
%yM1 = (1/2)*((2 M1 + M10 - ed (X)) - Sqrt[(M10 - ed (X))^2 + 4
tx0^2]);

% X^0 upper PL branch
y2d=0.5*((2*M1)+M10 -ed*(x2))+sqrt((M10-ed*(x2)).^2+4*tx0))+SS*x2;

% X^0_h lower PL branch
y3d=0.5*((M1+M2+M3+M10-ed*(x3))-sqrt((M1-
M2+M3+M10+ed*(x3)).^2+4*tx0h))+SS*x3;
%yM3 = (1/2)*((M1 + M2 + M3 + M10 - ed (X)) - Sqrt[(M1 - M2 + M3 +
M10 - ed (X))^2 + 4 tx0h^2]);

% X^0_h upper PL branch
y4d=0.5*((M1+M2+M3+M10-ed*(x4))+sqrt((M1-
M2+M3+M10+ed*(x4)).^2+4*tx0h))+SS*x4;

```

```

% X^2
y5d=0.5*(M4-M5-M6-sqrt((M1+M4+M10-ed*(x5)).^2+4*tx2m)...
+sqrt((M1-M5+M6+M10-ed*(x5)).^2+4*te2m))+SS*x5;
%yM5 = (1/2)*((M4 - M5 - M6) - Sqrt[(M1 + M4 + M10 - ed (X))^2 + 4
tx2^2] +
% Sqrt[(M1 - M5 + M6 + M10 - ed (X))^2 + 4 te2^2]);

% X^2
y6d=0.5*(M4-M5-M6-sqrt((M1+M4+M10-ed*(x6)).^2+4*tx2m)...
-sqrt((M1-M5+M6+M10-ed*(x6)).^2+4*te2m))+SS*x6;

%X^2
y7d=0.5*(M4-M5-M6+sqrt((M1+M4+M10-ed*(x7)).^2+4*tx2m)...
+sqrt((M1-M5+M6+M10-ed*(x7)).^2+4*te2m))+SS*x7;

%X^2
y8d=0.5*(M4-M5-M6+sqrt((M1+M4+M10-ed*(x8)).^2+4*tx2m)...
-sqrt((M1-M5+M6+M10-ed*(x8)).^2+4*te2m))+SS*x8;

% X^2h
y9d=0.5*(M7-M8-M9+sqrt((M1+M7+M10-ed*(x9)).^2+4*tx2mh)...
+sqrt((M1-M8+M9+M10-ed*(x9)).^2+4*te2mh))+SS*x9;
%yM9 = (1/2)*((M7 - M8 - M9) + Sqrt[(M1 + M7 + M10 - ed (X))^2 + 4
tx2h^2] +
% Sqrt[(M1 - M8 + M9 + M10 - ed (X))^2 + 4 te2h^2]);

%X^2h
y10d=0.5*(M7-M8-M9+sqrt((M1+M7+M10-ed*(x10)).^2+4*tx2mh)...
-sqrt((M1-M8+M9+M10-ed*(x10)).^2+4*te2mh))+SS*x10;

n=1;%1/2.355;%start with n large for simulated annealing, lower n
each round to narrow in on most likely, run with n=1 for
statistically valid sample
likelihoodNew = sum(log(normpdf(y4d,y4,y4e*n)))...

+sum(log(normpdf(y3d,y3,y3e*n)))+sum(log(normpdf(y5d,y5,y5e*n)))...

+sum(log(normpdf(y6d,y6,y6e*n)))+sum(log(normpdf(y1d,y1,y1e*n)))...

+sum(log(normpdf(y2d,y2,y2e*n)))+sum(log(normpdf(y7d,y7,y7e*n)))...

+sum(log(normpdf(y8d,y8,y8e*n)))+sum(log(normpdf(y9d,y9,y9e*n)))...
+sum(log(normpdf(y10d,y10,y10e*n)));
likeinit = likelihoodNew
LIKELIHOOD(1)=likeinit;
likelihood = likeinit;
tic;
for i=(1):(MCMCNum)
    M1=Para(1);
    M2=Para(2);
    M3=Para(3);

```

```

M4=Para(4);
M5=Para(5);
M6=Para(6);
M7=Para(7);
M8=Para(8);
M9=Para(9);
M10=Para(10);
F0=Para(11);
tx0=Para(12);
tx0h=Para(13);
tx2m=Para(14);
tx2mh=Para(15);
ed=Para(16);
SS=Para(17);
te2m=Para(18);
te2mh=Para(19);
switch (mod(i,gibbs))
case 0
    M1 = M1STD.*randn(1)+(M1MEAN);
case 1
    M2 = M2STD.*randn(1)+(M2MEAN);
case 2
    M3 = M3STD.*randn(1)+(M3MEAN);
case 3
    M4 = M4STD.*randn(1)+(M4MEAN);
case 4
    M5 = M5STD.*randn(1)+(M5MEAN);
case 5
    M6 = M6STD.*randn(1)+(M6MEAN);
case 6
    M7 = M7STD.*randn(1)+(M7MEAN);
case 7
    M8 = M8STD.*randn(1)+(M8MEAN);
case 8
    M9 = M9STD.*randn(1)+(M9MEAN);%800.*rand(1)+(800);
case 9
    M10 = M10STD.*randn(1)+(M10MEAN);
%case 10
%    F0 = F0STD.*randn(1)+(F0MEAN);
case 10
    tx0 = abs(tx0STD.*randn(1)+(tx0MEAN));
case 11
    tx0h = abs(tx0hSTD.*randn(1)+(tx0hMEAN));
case 12
    tx2m = abs(tx2mSTD.*randn(1)+(tx2mMEAN));
case 13
    tx2mh = abs(tx2mhSTD.*randn(1)+(tx2mhMEAN));
case 14
    ed = edSTD.*randn(1)+(edMEAN);
case 15
    SS = SSSTD.*randn(1)+(SSMEAN);
case 16

```

```

te2m = abs(te2mSTD.*randn(1)+(te2mMEAN));
case 17
te2mh = abs(te2mhSTD.*randn(1)+(te2mhMEAN));

end
ParaNew=[M1,M2,M3,M4,M5,M6,M7,M8,M9,M10,M10/ed,tx0,tx0h,tx2m,tx2mh,ed
,SS,te2m,te2mh];%Set new parameter values
% Now calculate the new likelihood function for this new set of
% parameter values
y1d=0.5*((2*M1)+M10 -ed*(x1))-sqrt((M10-ed*(x1)).^2+4*tx0))+SS*x1;
%yM1 = (1/2)*((2 M1 + M10 - ed (X)) - Sqrt[(M10 - ed (X))^2 + 4
tx0^2]);

% X^0 upper PL branch
y2d=0.5*((2*M1)+M10 -ed*(x2))+sqrt((M10-ed*(x2)).^2+4*tx0))+SS*x2;

% X^0_h lower PL branch
y3d=0.5*((M1+M2+M3+M10-ed*(x3))-sqrt((M1-
M2+M3+M10+ed*(x3)).^2+4*tx0h))+SS*x3;
%yM3 = (1/2)*((M1 + M2 + M3 + M10 - ed (X)) - Sqrt[(M1 - M2 + M3 +
M10 - ed (X))^2 + 4 tx0h^2]);

% X^0_h upper PL branch
y4d=0.5*((M1+M2+M3+M10-ed*(x4))+sqrt((M1-
M2+M3+M10+ed*(x4)).^2+4*tx0h))+SS*x4;

% X^2
y5d=0.5*(M4-M5-M6-sqrt((M1+M4+M10-ed*(x5)).^2+4*tx2m)...
+sqrt((M1-M5+M6+M10-ed*(x5)).^2+4*te2m))+SS*x5;
%yM5 = (1/2)*((M4 - M5 - M6) - Sqrt[(M1 + M4 + M10 - ed (X))^2 + 4
tx2^2] +
% Sqrt[(M1 - M5 + M6 + M10 - ed (X))^2 + 4 te2^2]);

% X^2
y6d=0.5*(M4-M5-M6-sqrt((M1+M4+M10-ed*(x6)).^2+4*tx2m)...
-sqrt((M1-M5+M6+M10-ed*(x6)).^2+4*te2m))+SS*x6;

%X^2
y7d=0.5*(M4-M5-M6+sqrt((M1+M4+M10-ed*(x7)).^2+4*tx2m)...
+sqrt((M1-M5+M6+M10-ed*(x7)).^2+4*te2m))+SS*x7;

%X^2
y8d=0.5*(M4-M5-M6+sqrt((M1+M4+M10-ed*(x8)).^2+4*tx2m)...
-sqrt((M1-M5+M6+M10-ed*(x8)).^2+4*te2m))+SS*x8;

% X^2h
y9d=0.5*(M7-M8-M9+sqrt((M1+M7+M10-ed*(x9)).^2+4*tx2mh)...
+sqrt((M1-M8+M9+M10-ed*(x9)).^2+4*te2mh))+SS*x9;
%yM9 = (1/2)*((M7 - M8 - M9) + Sqrt[(M1 + M7 + M10 - ed (X))^2 + 4
tx2h^2] +
% Sqrt[(M1 - M8 + M9 + M10 - ed (X))^2 + 4 te2h^2]);

```

```

%X^2h
y10d=0.5*(M7-M8-M9+sqrt((M1+M7+M10-ed*(x10)).^2+4*tx2mh)...
    -sqrt((M1-M8+M9+M10-ed*(x10)).^2+4*te2mh))+SS*x10;

likelihoodNew = sum(log(normpdf(y4d,y4,y4e*n)))...

+sum(log(normpdf(y3d,y3,y3e*n)))+sum(log(normpdf(y5d,y5,y5e*n)))...

+sum(log(normpdf(y6d,y6,y6e*n)))+sum(log(normpdf(y1d,y1,y1e*n)))...

+sum(log(normpdf(y2d,y2,y2e*n)))+sum(log(normpdf(y7d,y7,y7e*n)))...

+sum(log(normpdf(y8d,y8,y8e*n)))+sum(log(normpdf(y9d,y9,y9e*n)))...
    +sum(log(normpdf(y10d,y10,y10e*n)));
if likelihoodNew > likelihood+log(rand(1))% the inclusion of this
log(rand(1))
% keeps some parameter value sets even when the likelihood (cost)
% function has not improved
    Para=ParaNew;
    likelihood = likelihoodNew;
end

if mod(i, subsample)==0 %save only one sample each subsample steps
    PARASET(i/subsample, :)=Para;
    LIKELIHOOD(i/subsample)=likelihood;
end

if mod(i, subsample*numbertosave/100)==0 %periodically write to file
    a = toc;
    perc = i/subsample/numbertosave*100;
    disp(strcat(num2str(perc), '% done, ', num2str(a/60/60), ' hours
elapsed'))

save('MCMCResults_FWHMLarger_SensitivityCheck.mat', 'PARASET', 'LIKELIHOOD')
end
end

%Now to plot the lines against data and highest likelihood values
AMeanofparaset = mean(PARASET);
AStddeviation = std(PARASET);
AMeanoflikelihood = mean(LIKELIHOOD);
AStddeviationlikelihood = std(LIKELIHOOD);
MeanofParaset = AMeanofparaset';
Stddeviation = AStddeviation';
[LargestLikelihood, indexvalue] = max(LIKELIHOOD);
HighestParaset = (PARASET(indexvalue, 1:19))';
Check = HighestParaset;

```

```

LM1=Check(1);
LM2 = Check(2);
LM3=Check(3);
LM4=Check(4);
LM5=Check(5);
LM6=Check(6);
LM7=Check(7);
LM8=Check(8);
LM9=Check(9);
LM10=Check(10);
LF0=Check(11);
Ltx0=Check(12);
Ltx0h=Check(13);
Ltx2m=Check(14);
Ltx2mh=Check(15);
Lte2m=Check(18);
Lte2mh=Check(19);
Led=Check(16);
LSS=Check(17);

```

```

X1=linspace(18,22);
X2=linspace(18,23);
X3=linspace(11,21);
X4=linspace(14,23);
X5=linspace(0,11);
X6=linspace(1,11);
X7=linspace(2,9);
X8=linspace(1,14);
X9=linspace(2,5);
X10=linspace(0,3);

```

```

yL1=0.5*((2*LM1)+LM10 -Led*(X1))-sqrt((LM10-
Led*(X1)).^2+4*Ltx0))+LSS*X1;
yL2=0.5*((2*LM1)+LM10 -Led*(X2))+sqrt((LM10-
Led*(X2)).^2+4*Ltx0))+LSS*X2;
yL3=0.5*((LM1+LM2+LM3+LM10-Led*(X3))-sqrt((LM1-
LM2+LM3+LM10+Led*(X3)).^2+4*Ltx0h))+LSS*X3;
yL4=0.5*((LM1+LM2+LM3+LM10-Led*(X4))+sqrt((LM1-
LM2+LM3+LM10+Led*(X4)).^2+4*Ltx0h))+LSS*X4;
yL5=0.5*(LM4-LM5-LM6-sqrt((LM1+LM4+LM10-
Led*(X5)).^2+4*Ltx2m)+sqrt((LM1-LM5+LM6+LM10-
Led*(X5)).^2+4*Lte2m))+LSS*X5;
yL6=0.5*(LM4-LM5-LM6-sqrt((LM1+LM4+LM10-Led*(X6)).^2+4*Ltx2m)-
sqrt((LM1-LM5+LM6+LM10-Led*(X6)).^2+4*Lte2m))+LSS*X6;
yL7=0.5*(LM4-LM5-LM6+sqrt((LM1+LM4+LM10-
Led*(X7)).^2+4*Ltx2m)+sqrt((LM1-LM5+LM6+LM10-
Led*(X7)).^2+4*Lte2m))+LSS*X7;
yL8=0.5*(LM4-LM5-LM6+sqrt((LM1+LM4+LM10-Led*(X8)).^2+4*Ltx2m)-
sqrt((LM1-LM5+LM6+LM10-Led*(X8)).^2+4*Lte2m))+LSS*X8;

```

```

yL9=0.5*(LM7-LM8-LM9+sqrt((LM1+LM7+LM10-
Led*(X9)).^2+4*Ltx2mh)+sqrt((LM1-LM8+LM9+LM10-
Led*(X9)).^2+4*Lte2mh))+LSS*X9;
yL10=0.5*(LM7-LM8-LM9+sqrt((LM1+LM7+LM10-Led*(X10)).^2+4*Ltx2mh)-
sqrt((LM1-LM8+LM9+LM10-Led*(X10)).^2+4*Lte2mh))+LSS*X10;

figure(3);
subplot(2,5,1);
plot(X1,yL1,'b-',x1,y1,'rx');
hold on;
errorbar(x1,y1,y1e,'rx');
hold off;

subplot(2,5,2);
plot(X2,yL2,'b-',x2,y2,'rx');
hold on;
errorbar(x2,y2,y2e,'rx');
hold off;

subplot(2,5,3);
plot(X3,yL3,'b-',x3,y3,'rx');
hold on;
errorbar(x3,y3,y3e,'rx');
hold off;

subplot(2,5,4);
plot(X4,yL4,'b-',x4,y4,'rx');
hold on;
errorbar(x4,y4,y4e,'rx');
hold off;

subplot(2,5,5);
plot(X5,yL5,'b-',x5,y5,'rx');
hold on;
errorbar(x5,y5,y5e,'rx');
hold off;

subplot(2,5,6);
plot(X6,yL6,'b-',x6,y6,'rx');
hold on;
errorbar(x6,y6,y6e,'rx');
hold off;

subplot(2,5,7);
plot(X7,yL7,'b-',x7,y7,'rx');
hold on;
errorbar(x7,y7,y7e,'rx');
hold off;

subplot(2,5,8);

```

```

plot(X8,yL8,'b-',x8,y8,'rx');
hold on;
errorbar(x8,y8,y8e,'rx');
hold off;

subplot(2,5,9);
plot(X9,yL9,'b-',x9,y9,'rx');
hold on;
errorbar(x9,y9,y9e,'rx');
hold off;

subplot(2,5,10);
plot(X10,yL10,'b-',x10,y10,'rx');
hold on;
errorbar(x10,y10,y10e,'rx');
hold off;

saveas(figure(3),'DataThief_LargerFWHM_Sensitivity check.jpg');

figure(4);
plot(x1,y1,'x',x2,y2,'x',x3,y3,'x',x4,y4,'x',x5,y5,'x',x6,y6,'x',x7,y
7,'x',x8,y8,'x',x9,y9,'x',x10,y10,'x');
%saveas(figure(4),'SparseData_Datathief.jpg')

save('MCMCResults_FWHMLarger_SensitivityCheck.mat',
'PARASET','LIKELIHOOD','MeanofParaset','Stddeviation','HighestParaset
');
T1 = table ( MeanofParaset , Stddeviation);
T2 = table
(M1,M2,M3,M4,M5,M6,M7,M8,M9,M10,F0,tx0,tx0h,tx2m,tx2mh,te2m,te2mh,ed,
SS);

%Now plot the likelihood trace
figure(1);
d=size(LIKELIHOOD);
x=1:d;
plot(x,LIKELIHOOD);

%print the initial likelihood and the maximum acheived during the run
(the y
%should be similar)
format short;
[likeinit max(LIKELIHOOD)];

```

```

% Now plot the histogram of possible values for each fitting
parameter and
%fit each histogram with a Gaussian distribution.
histnumber = 100;
figure(2);
subplot(2,10,1);
histfit(PARASET(1:1:end,1),histnumber)
subplot(2,10,2)
histfit(PARASET(1:1:end,2),histnumber)
subplot(2,10,3)
histfit(PARASET(1:1:end,3),histnumber)
subplot(2,10,4)
histfit(PARASET(1:1:end,4),histnumber)
subplot(2,10,5)
histfit(PARASET(1:1:end,5),histnumber)
subplot(2,10,6)
histfit(PARASET(1:1:end,6),histnumber)
subplot(2,10,7)
histfit(PARASET(1:1:end,7),histnumber)
subplot(2,10,8)
histfit(PARASET(1:1:end,8),histnumber)
subplot(2,10,9)
histfit(PARASET(1:1:end,9),histnumber) %Not a Gaussian, histfit
inappropriate
subplot(2,10,10)
histfit(PARASET(1:1:end,10),histnumber)
subplot(2,10,11)
histfit(PARASET(1:1:end,11),histnumber)
subplot(2,10,12)
histfit(PARASET(1:1:end,12),histnumber)
subplot(2,10,13)
histfit(PARASET(1:1:end,13),histnumber)
subplot(2,10,14)
histfit(PARASET(1:1:end,14),histnumber)
subplot(2,10,15)
histfit(PARASET(1:1:end,15),histnumber)
subplot(2,10,16)
histfit(PARASET(1:1:end,16),histnumber)
subplot(2,10,17)
histfit(PARASET(1:1:end,17),histnumber)
subplot(2,10,18)
histfit(PARASET(1:1:end,18),histnumber)
subplot(2,10,19)
histfit(PARASET(1:1:end,19),histnumber)

% Print the standard deviation of all parameters
std(PARASET(1:1:end,:))

[size(unique(PARASET(:,1)),1) size(unique(PARASET(:,2)),1) ...
 size(unique(PARASET(:,3)),1) size(unique(PARASET(:,4)),1) ...
 size(unique(PARASET(:,5)),1) size(unique(PARASET(:,6)),1) ...
 size(unique(PARASET(:,7)),1) size(unique(PARASET(:,8)),1) ...

```

```

size(unique(PARASET(:,9)),1) size(unique(PARASET(:,10)),1)...
size(unique(PARASET(:,11)),1) size(unique(PARASET(:,12)),1)...
size(unique(PARASET(:,13)),1) size(unique(PARASET(:,14)),1)...
size(unique(PARASET(:,15)),1) size(unique(PARASET(:,16)),1)...
size(unique(PARASET(:,17)),1) size(unique(PARASET(:,18)),1)...
size(unique(PARASET(:,19)),1)]./numbertosave

% Print Median and 95% confidence interval for each parameter.
format shorteng;
prctile(PARASET(1:1:end,:),[50 2.5 97.5])';
% Since M9 is a one-sided test, this should technically be re-run as
% prctile(PARASET(:,9),[95] to get the upper 95% confidence bound on
M9
format short;

```

## Appendix C

### CODE FOR GENERATING PREDICTION INTERVAL

```
%load ('MCMCResults_DataThief_2_IdiotCheck100hrs.mat');% Results from
dense
%unguided
%load('DataThief_20171110.mat');%data for Dense unguided
load ('MCMC_20171130.mat');% results from Sparse Unguided
load('DataThiefSparse_20171127.mat');% Sparse Data thief data

%prctile(PARASET(1,:),[2.5 100 97.5]);

[mx,ind] = max(LIKELIHOOD);
M1MLE = (PARASET(ind, 1))';
M2MLE = (PARASET(ind, 2))';
M3MLE = (PARASET(ind, 3))';
M4MLE = (PARASET(ind, 4))';
M5MLE = (PARASET(ind, 5))';
M6MLE = (PARASET(ind, 6))';
M7MLE = (PARASET(ind, 7))';
M8MLE = (PARASET(ind, 8))';
M9MLE = (PARASET(ind, 9))';
M10MLE = (PARASET(ind,10))';
F0MLE = (PARASET(ind, 11))';
tx0MLE = (PARASET(ind, 12))';
tx0hMLE = (PARASET(ind, 13))';
tx2MLE = (PARASET(ind, 14))';
tx2hMLE = (PARASET(ind, 15))';
edMLE = (PARASET(ind, 16))';
SSMLE = (PARASET(ind, 17))';
te2MLE = (PARASET(ind, 18))';
te2hMLE = (PARASET(ind, 19))';

figure (2);
[sortlikes,indices] = sort(LIKELIHOOD);
plot(sortlikes);
%NewsortedParaset(i,19)= PARASET(indices(i),19);
NSP=PARASET(indices,:); %NewsortedParaset

Likelihood_size = size (LIKELIHOOD);
lowerlimit = 0.05*Likelihood_size(1,1);
upperlimit = Likelihood_size(1,1);
Hx1 = size(x1);
```

```

Hx2 = size(x2);
Hx3 = size(x3);
Hx4 = size(x4);
Hx5 = size(x5);
Hx6 = size(x6);
Hx7 = size(x7);
Hx8 = size(x8);
Hx9 = size(x9);
Hx10 = size(x10);

```

```

y1test=[];
y2test=[];
y3test=[];
y4test=[];
y5test=[];
y6test=[];
y7test=[];
y8test=[];
y9test=[];
y10test=[];

```

```

for i = 1:1:Hx1(1,1)
    y1test(:,i) =
    0.5*((2*NSP(lowerlimit:upperlimit,1))+NSP(lowerlimit:upperlimit,10)-
    NSP(lowerlimit:upperlimit,16).*(x1(i)))-
    sqrt((NSP(lowerlimit:upperlimit,10)-...

```

```

    NSP(lowerlimit:upperlimit,16)*(x1(i)).^2+4*NSP(lowerlimit:upperlimit
    ,12)))+NSP(lowerlimit:upperlimit,17)*x1(i);
end

```

```

for i = 1:1:Hx2(1,1)
    y2test(:,i) =
    0.5*((2*NSP(lowerlimit:upperlimit,1))+NSP(lowerlimit:upperlimit,10)-
    NSP(lowerlimit:upperlimit,16).*(x2(i)))+sqrt((NSP(lowerlimit:upperlim
    it,10)-...

```

```

    NSP(lowerlimit:upperlimit,16)*(x2(i)).^2+4*NSP(lowerlimit:upperlimit
    ,12)))+NSP(lowerlimit:upperlimit,17)*x2(i);
end

```

```

for i = 1:1:Hx3(1,1)

```

```

    y3test(:,i)=0.5*((NSP(lowerlimit:upperlimit,1)+NSP(lowerlimit:upperli
    mit,2)+NSP(lowerlimit:upperlimit,3)+NSP(lowerlimit:upperlimit,10)-
    NSP(lowerlimit:upperlimit,16)*x3(i))...
        -sqrt((NSP(lowerlimit:upperlimit,1)-
    NSP(lowerlimit:upperlimit,2)+NSP(lowerlimit:upperlimit,3)+NSP(lowerli

```

```

mit:upperlimit,10)+NSP(lowerlimit:upperlimit,16)*x3(i)).^2+4*NSP(love
rlimit:upperlimit,13)))...
        +NSP(lowerlimit:upperlimit,17)*x3(i);
end

for i = 1:1:Hx4(1,1)

y4test(:,i)=0.5*((NSP(lowerlimit:upperlimit,1)+NSP(lowerlimit:upperli
mit,2)+NSP(lowerlimit:upperlimit,3)+NSP(lowerlimit:upperlimit,10)-
NSP(lowerlimit:upperlimit,16)*x4(i))...
        +sqrt((NSP(lowerlimit:upperlimit,1)-
NSP(lowerlimit:upperlimit,2)+NSP(lowerlimit:upperlimit,3)+NSP(lowerli
mit:upperlimit,10)+NSP(lowerlimit:upperlimit,16)*x4(i)).^2+4*NSP(love
rlimit:upperlimit,13)))...
        +NSP(lowerlimit:upperlimit,17)*x4(i);
end

for i = 1:1:Hx5(1,1)
    y5test(:,i)=0.5*(NSP(lowerlimit:upperlimit,4)-
NSP(lowerlimit:upperlimit,5)-NSP(lowerlimit:upperlimit,6)...
-
sqrt((NSP(lowerlimit:upperlimit,1)+NSP(lowerlimit:upperlimit,4)+NSP(1
owerlimit:upperlimit,10)-
NSP(lowerlimit:upperlimit,16)*(x5(i))).^2+4*NSP(lowerlimit:upperlimit
,14))...
        +sqrt((NSP(lowerlimit:upperlimit,1)-
NSP(lowerlimit:upperlimit,5)+NSP(lowerlimit:upperlimit,6)+NSP(lowerli
mit:upperlimit,10)-
NSP(lowerlimit:upperlimit,16)*(x5(i))).^2+4*NSP(lowerlimit:upperlimit
,18)))...
        +NSP(lowerlimit:upperlimit,17)*x5(i);
end

for i = 1:1:Hx6(1,1)
    y6test(:,i)=0.5*(NSP(lowerlimit:upperlimit,4)-
NSP(lowerlimit:upperlimit,5)-NSP(lowerlimit:upperlimit,6)...
-
sqrt((NSP(lowerlimit:upperlimit,1)+NSP(lowerlimit:upperlimit,4)+NSP(1
owerlimit:upperlimit,10)-
NSP(lowerlimit:upperlimit,16)*(x6(i))).^2+4*NSP(lowerlimit:upperlimit
,14))...
        -sqrt((NSP(lowerlimit:upperlimit,1)-
NSP(lowerlimit:upperlimit,5)+NSP(lowerlimit:upperlimit,6)+NSP(lowerli
mit:upperlimit,10)-
NSP(lowerlimit:upperlimit,16)*(x6(i))).^2+4*NSP(lowerlimit:upperlimit
,18)))...
        +NSP(lowerlimit:upperlimit,17)*x6(i);
end

for i = 1:1:Hx7(1,1)
    y7test(:,i)=0.5*(NSP(lowerlimit:upperlimit,4)-
NSP(lowerlimit:upperlimit,5)-NSP(lowerlimit:upperlimit,6)...

```

```

+sqrt((NSP(lowerlimit:upperlimit,1)+NSP(lowerlimit:upperlimit,4)+NSP(
lowerlimit:upperlimit,10)-
NSP(lowerlimit:upperlimit,16)*(x7(i))).^2+4*NSP(lowerlimit:upperlimit
,14))...
+sqrt((NSP(lowerlimit:upperlimit,1)-
NSP(lowerlimit:upperlimit,5)+NSP(lowerlimit:upperlimit,6)+NSP(lowerli
mit:upperlimit,10)-
NSP(lowerlimit:upperlimit,16)*(x7(i))).^2+4*NSP(lowerlimit:upperlimit
,18))...
+NSP(lowerlimit:upperlimit,17)*x7(i);
end

for i = 1:1:Hx8(1,1)
y8test(:,i)=0.5*(NSP(lowerlimit:upperlimit,4)-
NSP(lowerlimit:upperlimit,5)-NSP(lowerlimit:upperlimit,6)...

+sqrt((NSP(lowerlimit:upperlimit,1)+NSP(lowerlimit:upperlimit,4)+NSP(
lowerlimit:upperlimit,10)-
NSP(lowerlimit:upperlimit,16)*(x8(i))).^2+4*NSP(lowerlimit:upperlimit
,14))...
-sqrt((NSP(lowerlimit:upperlimit,1)-
NSP(lowerlimit:upperlimit,5)+NSP(lowerlimit:upperlimit,6)+NSP(lowerli
mit:upperlimit,10)-
NSP(lowerlimit:upperlimit,16)*(x8(i))).^2+4*NSP(lowerlimit:upperlimit
,18))...
+NSP(lowerlimit:upperlimit,17)*x8(i);
end
for i=1:1:Hx9(1,1)
y9test(:,i)= 0.5*(NSP(lowerlimit:upperlimit,7)-
NSP(lowerlimit:upperlimit,8)-NSP(lowerlimit:upperlimit,9)...

+sqrt((NSP(lowerlimit:upperlimit,1)+NSP(lowerlimit:upperlimit,7)+NSP(
lowerlimit:upperlimit,10)-
NSP(lowerlimit:upperlimit,16)*(x9(i))).^2+4*NSP(lowerlimit:upperlimit
,15))...
+sqrt((NSP(lowerlimit:upperlimit,1)-
NSP(lowerlimit:upperlimit,8)+NSP(lowerlimit:upperlimit,9)+NSP(lowerli
mit:upperlimit,10)-
NSP(lowerlimit:upperlimit,16)*(x9(i))).^2+4*NSP(lowerlimit:upperlimit
,19))...
+NSP(lowerlimit:upperlimit,17)*x9(i);
end
for i=1:1:Hx10(1,1)
y10test(:,i)= 0.5*(NSP(lowerlimit:upperlimit,7)-
NSP(lowerlimit:upperlimit,8)-NSP(lowerlimit:upperlimit,9)...

+sqrt((NSP(lowerlimit:upperlimit,1)+NSP(lowerlimit:upperlimit,7)+NSP(
lowerlimit:upperlimit,10)-
NSP(lowerlimit:upperlimit,16)*(x10(i))).^2+4*NSP(lowerlimit:upperlimi
t,15))...

```

```

        -sqrt((NSP(lowerlimit:upperlimit,1)-
NSP(lowerlimit:upperlimit,8)+NSP(lowerlimit:upperlimit,9)+NSP(lowerli
mit:upperlimit,10)-
NSP(lowerlimit:upperlimit,16)*(x10(i))).^2+4*NSP(lowerlimit:upperlimi
t,19)))...
        +NSP(lowerlimit:upperlimit,17)*x10(i);
end

%Now Calculating Max and min at each volatge point for each line
%Just a reminder, here each column for yntest is the y value for all
%paraset at each value
y1ub = max(y1test);
y1lb = min(y1test);
y2ub = max(y2test);
y2lb = min(y2test);
y3ub = max(y3test);
y3lb = min(y3test);
y4ub = max(y4test);
y4lb = min(y4test);
y5ub = max(y5test);
y5lb = min(y5test);
y6ub = max(y6test);
y6lb = min(y6test);
y7ub = max(y7test);
y7lb = min(y7test);
y8ub = max(y8test);
y8lb = min(y8test);
y9ub = max(y9test);
y9lb = min(y9test);
y10ub = max(y10test);
y10lb = min(y10test);

y1limits = vertcat(y1ub,y1lb)';
y2limits = vertcat(y2ub,y2lb)';
y3limits = vertcat(y3ub,y3lb)';
y4limits = vertcat(y4ub,y4lb)';
y5limits = vertcat(y5ub,y5lb)';
y6limits = vertcat(y6ub,y6lb)';
y7limits = vertcat(y7ub,y7lb)';
y8limits = vertcat(y8ub,y8lb)';
y9limits = vertcat(y9ub,y9lb)';
y10limits = vertcat(y10ub,y10lb)';

y1err = (y1ub-y1lb)';
y2err = (y2ub-y2lb)';
y3err = (y3ub-y3lb)';
y4err = (y4ub-y4lb)';
y5err = (y5ub-y5lb)';
y6err = (y6ub-y6lb)';
y7err = (y7ub-y7lb)';
y8err = (y8ub-y8lb)';
y9err = (y9ub-y9lb)';

```

```

y10err = (y10ub-y10lb)';

%Dense unguided prediction results
%{
save('MCMCResults_BruceAskedErrorBars.mat','y1limits','y2limits','y3l
imits','y4limits','y5limits','y6limits',...

'y7limits','y8limits','y9limits','y10limits','y1ub','y1lb','y2ub','y2
lb','y3ub','y3lb','y4ub','y4lb','y5ub','y5lb',...

'y6ub','y6lb','y7ub','y7lb','y8ub','y8lb','y9ub','y9lb','y10ub','y10l
b');
save('MCMCResults_DenseUnguided_PredictionInterval.mat','y1err','y2er
r','y3err','y4err','y5err','y6err',...
      'y7err','y8err','y9err','y10err');
%}

save
('PredictionInterval_SparseUnguided.mat','y1limits','y2limits','y3lim
its','y4limits','y5limits','y6limits',...

'y7limits','y8limits','y9limits','y10limits','y1ub','y1lb','y2ub','y2
lb','y3ub','y3lb','y4ub','y4lb','y5ub','y5lb',...

'y6ub','y6lb','y7ub','y7lb','y8ub','y8lb','y9ub','y9lb','y10ub','y10l
b','y1err','y2err','y3err','y4err','y5err','y6err',...
      'y7err','y8err','y9err','y10err');

```

## Appendix D

### PROCEDURE FOR REFILLING LIQUID HELIUM WITH THE RELIQUIFIER IN OPERATION

- 1) Turn the compressor off at least 12 hours prior to the refill so as to raise the temperature of the cold head to room temperature. The heater on the cold head can also be used to raise the temperature however the heater should only be used under extraneous circumstances.
- 2) Turn the needle valve to close and also the valve which connects the sample space and the liquid Helium reservoir.
- 3) Disconnect the connection between the cold head and the remote controller. Leave the connection between the cold head and temperature controller on through the entire process of the fill.
- 4) Check LHe level
  - a. If low, leave the vent connection on and disconnect the return valve to the cold head from the control valve side. Leaving the He reservoir vent on will prevent excessive loss of LHe.
  - b. If manageable i.e. greater than 5 inches (consider the size of the refill dewar ordered), open the vent and disconnect the return to the cold head.
- 5) Loosen the valve around the drain leg to allow easy translation of the drain leg. Move the drain leg carefully and check for vibrations during transit. If the vibrations are present, slow down. Once on top, move the drain leg out of the way for the refill pipe by loosening the screws on the base of the cold head.
- 6) Refer step 4, if LHe level is low, now is the time to open the LHe reservoir vent.
- 7) If the refill dewar is greater than 60l, use the cooper extension tube on the refill LHe transfer tube, if not continue without the extension.
- 8) Hold the transfer tube (both ends perpendicular to each other) in one hand and use the other hand to guide the dewar end into the dewar. Close the relief valve

on the dewar. Push it gently down, all the way to the bottom, once it hits the bottom raise it just a little to allow LHe to enter the transfer tube.

- 9) Put the cryostat end into the cryostat once you feel either really cold gas or white jet (indicates LHe). Put it through the 6 buffer slots gently, do not force it.
- 10) At the dewar, the connect the He gas to gas input section, increase the flow till the pressure on the dewar is between 3 to 5 psi.
- 11) Change the read-out interval to 3 minutes and monitor. Turn the gas off once the LHe level is at 33 inches.
- 12) Once the fill is complete, we need to purge the cold head with He gas. Make the He gas connections and ensure the cold head temperature at 300K. Ensure moderate He gas flow through the cold head for at least 30 minutes.
- 13) Once the purge is done, start lowering the cold head
  - a. Insert the extension tube into the input port of the cryostat secured with a c clamp to prevent it from falling into the reservoir. When the drain leg sufficiently close to the input port connect it to the extension.
  - b. Position the cold head drain leg and start lowering the cold head. Check for vibrations, and turn off the He gas purging the cold head.
- 14) Once the cold head is lowered completely, wrench tight the valve and close the reservoir vent.
- 15) Make the compressor and cold head connection. Open the valve which connects the sample space and reservoir. Also open the needle valve.
- 16) Change the set point on the cold head's temperature controller to 4K and turn off the heater on the cold head.
- 17) Change the read-out interval on the LHe level to 1 hour.

## Appendix E

### FIRST COOL DOWN PROCEDURE

- 1) Ensure that the whole system is at room temperature. If not, use the capillary heater to bring the temperature to a maximum of 293K. Heating the system beyond 293K could lead to melt an Indium O ring seal, which would require taking the entire cryostat apart for repair.
- 2) Pump the outer vacuum jacket of the cryostat to  $10^{-7}$  Torr which usually takes 2 to 3 days.
  - a. Connect the pumping line to the Turbo pump.
  - b. Make sure the switch (black switch on the backing pump) is flipped for turbo operation
  - c. Connect the pumping line to the outer jacket port, the valve on the port is closed. Turn the pump on, backing and turbo. Pump the line first and then open the valve to start pumping of the outer jacket. Ensure the backing pump has reduced the pressure to atleast  $10^{-2}$  before turning the turbo on.
- 3) Pump the inner vacuum jacket of the cryostat to  $10^{-7}$  Torr, usually takes a day and a half.
- 4) Separately pump the sample space.
- 5) Raise the Liquid Helium reliquefier and take off the extension of the drain leg. Be very careful not to let this extension fall back into the cryostat, use any C Clamp, to prevent its fall into the cryostat. Turn the drain leg away from the filling port.
- 6) The next step is pumping of the sample space for two reasons, viz, to check for any ice blocks in the capillary opening and to pump both the sample space and helium reservoir. To do this, seal/close all the Helium reservoir ports (fill, vent & on the T). Before sealing the fill port, insert the first fill extension tube into the port and then seal it, this is done so as to use the extension tube for N<sub>2</sub> gas purge.

- 7) Pump the sample space, use the roughing pumping mode. a) Connect the pumping line to roughing pump. b) Make sure the needle valve is closed. c) Start the pump and open the sample space port just before the T, once opened the pressure on the gauge will drop to -30, now open the needle valve, if the pressure becomes positive this indicates there is no ice block. d) Continue pumping the whole system ( LHe Reservoir) for atleast 15 to 20 mins. Then close the valve on the pump side and change the position of the needle valve. If you see any change in pressure, then start pumping again. The idea is if the whole space is pumped, thus changing the position of the needle valve slightly should not be changing the pressure.
- 8) Purge the sample space and the LHe reservoir with LN2 gas, till the sample space vent starts venting.
- 9) After the sample space starts to vent, reduce the N2 flow, get the first extension tube. It needs to be sealed with an o ring and the brass caps. The extension tube needs to be screwed in and wrench tightened.
- 10) Be prepared with rubber pipe with the 2 metal extensions.
- 11) Into the extension tube insert the LN2 transfer line and start filling Ln2. The temperature/resistance sensor at the bottom of the reservoir 480-490 ohm. Also check the resistance of the magnet coils at 96 K the 10.4 Ohms (9.5 ohms) for vertical coil (horizontal coil).
- 12) After shutting the LN2 fill, wait for 15-20 mins to see if the temperature stays at LN2 temperature. If the temperature increases start the LN2 fill again. We want LN2 to sit in the system for at least 45 min to 1 hour to allow all the parts to come to equilibrium at 77K.
- 13) Connect the LHe fill port with LN2 fill port with the rubber/metal tube. Connect Grade 5 He gas to start pressurizing and driving LN2 from the LHe reservoir into the LN2 reservoir. The temperature sensor would show an increase in temperature when LN2 is completely pushed out. We want to see it just above 77K, verifying that there is no LN2 left that will freeze to ice. But not much higher than 77K so that there isn't a big thermal load on the He.
- 14) Vacuum pump the Helium reservoir and sample space and purge with grade 5 He gas. Open both the connections between the sample space and He reservoir, both these spaces have to be pumped and purged. Repeat this process a couple of times.

- 15) Start the He Fill process, pump the sample space in the meantime to ensure no ice block in the capillary.
- 16) Once the fill is complete, remove the first cool down extension tube.
- 17) Put the reliquifier back in and start the reliquifier.
- 18) Open the needle valve to cool down sample space.